

X-RAY BUBBLES IN GALAXY CLUSTERS

A dissertation presented to

the faculty of

the College of Arts and Sciences of Ohio University

In partial fulfillment

of the requirements for the degree

Doctor of Philosophy

Filofteia Laura Rafferty

August 2007

This dissertation titled  
X-RAY BUBBLES IN GALAXY CLUSTERS

by  
FILOFTEIA LAURA RAFFERTY

has been approved for  
the Department of Physics and Astronomy  
and the College of Arts and Sciences by

---

Brian R. McNamara

Professor of Physics and Astronomy

---

Benjamin M. Ogles

Dean, College of Arts and Sciences

# Abstract

RAFFERTY, FILOFTEIA LAURA, Ph.D., August 2007, Physics and Astronomy

X-RAY BUBBLES IN GALAXY CLUSTERS (148pp.)

Director of Dissertation: Brian R. McNamara

We present an analysis of radio data for 24 radio galaxies observed with the Very Large Array (VLA) in at least 3 different frequencies. These systems possess prominent X-ray surface brightness depressions associated with cavities or bubbles that were created by interactions between powerful radio sources and the surrounding hot gas. We use the X-ray cavities to measure the mechanical jet power of radio sources over six decades of radio luminosity, independently of the radio properties themselves, which we measure from the VLA data.

Using these measurements, we examine the ratio between radio power and total jet power (the radiative efficiency). We find that the jet power increases with increasing radio power and that the radio sources in our sample are generally poor radiators, with radiative efficiencies ranging from 1 (Cygnus A) to 0.0001 (HCG 62). We argue that radio aging may be partly responsible for this wide range in the radiative efficiencies, in combination with intrinsic differences in the magnetic field strengths and the particle content ( $k$ , the ratio between the heavy-particle energy and electron energy). We place limits on the magnetic field strengths and on the particle content of the radio lobes. We find that the magnetic field strengths derived under different assumptions (equipartition, pressure equilibrium, and by requiring the synchrotron

age to be equal with the buoyancy age) are larger than the cluster wide magnetic field strengths, with the ones derived under pressure equilibrium being much larger than the others. In order for pressure-equilibrium magnetic field strengths to be equal with the equipartition magnetic field, the particle content ( $k$ ) needs to vary from  $\sim 1$  to 35000. Such high values of  $k$  support the idea of heavy jets. By comparing the synchrotron ages with the X-ray-derived ages, we find that the two ages are uncoupled, with the youngest systems, which may be in a driving stage, being better estimated by the synchrotron age. Having radio images in at least 3 frequencies, we are better able to classify a cavity as active, intermediate, or ghost based on the break frequency. However, because of the continuous range in break frequencies that we find, the separation of our sample into different categories is somewhat arbitrary. Lastly, we find that 327 MHz radio maps are typically better suited for tracing the cavity sizes than 1.4 GHz radio maps, and they are a promising proxy for X-ray cavities in systems where it is difficult to image the cavities directly in X-rays.

Approved: \_\_\_\_\_

Brian R. McNamara

Professor of Physics and Astronomy

# Acknowledgments

I would like to acknowledge my advisor, Brian McNamara, for his guidance and help throughout this dissertation. I would also like to thank my committee members, Markus Boettcher, Greg Nadon, and Doug Clowe, for their careful reading of the manuscript and many insightful suggestions for its improvement.

# Table of Contents

	Page
Abstract . . . . .	3
Acknowledgments . . . . .	5
List of Tables . . . . .	8
List of Figures . . . . .	9
1 Introduction . . . . .	12
1.1 The Cooling Flow Problem . . . . .	13
1.2 The Interaction of the AGN with the ICM: X-ray Cavities . . . . .	15
2 The Sample . . . . .	22
2.1 X-Ray Data Reduction and Analysis for the Initial Sample of 18 Systems	25
2.1.1 X-Ray Analysis . . . . .	25
2.1.2 X-Ray Surface Brightness Depressions . . . . .	26
2.2 Radio Reduction and Analysis for the Extended 24-System Sample .	30
2.2.1 Radio Observations and Data Reduction . . . . .	30
2.2.2 Radio Morphologies . . . . .	35
2.2.3 Total Radio Luminosity . . . . .	36
3 Theory . . . . .	39
3.1 X-Ray Cavity Energies and Ages . . . . .	39
3.2 Basic Formulas of Synchrotron Radiation . . . . .	40
3.2.1 Spectrum of Synchrotron Radiation and Total Emitted Power	40

3.2.2	Spectral Modeling and Ages . . . . .	42
3.3	Energy Content and Equipartition Magnetic Fields . . . . .	44
3.4	Particle Content ( $k$ ) . . . . .	46
4	Results . . . . .	48
4.1	Cavity Classification . . . . .	48
4.2	Magnetic Field and Particle Content . . . . .	52
4.3	Does Equipartition Apply in the Lobes of the Radio Sources? . . .	61
4.4	Synchrotron Spectrum and Ages . . . . .	63
4.5	Radiative Efficiencies . . . . .	73
4.5.1	Radiative Efficiencies for the Initial 18-System Sample . . .	73
4.5.2	Radiative Efficiencies for the Extended 24-System Sample .	78
4.6	Radio Observations As a Tracer of Cavity Size . . . . .	84
5	Conclusions . . . . .	91
	Bibliography . . . . .	96
A	Details of Radio Observations and Image Properties . . . . .	112
B	Radio Images . . . . .	122
C	Co-authored Publications . . . . .	148

# List of Tables

2.1	Initial Sample Properties.	24
2.2	Cavity properties.	28
2.3	Radio fluxes, spectral indices, and radio luminosities	32
4.1	Lobe properties derived using the cavity sizes from X-ray observations	54
4.2	Magnetic field, synchrotron age, and particle content using the lobe sizes from 327 MHz radio observations	56
4.3	Break frequency	68
4.4	Radio lobe sizes and pressures	87
A.1	Summary of radio observations	113
A.2	Radio image properties	118

# List of Figures

4.1 <i>Left:</i> Histogram of the ratio of heavy-particle energy to electron energy; <i>Right:</i> Histogram of the corresponding magnetic field strengths . . . . .	58
4.2 The ratio of heavy-particle energy to electron energy versus the adiabatically corrected break frequency . . . . .	60
4.3 <i>Left:</i> Equipartition magnetic field strength vs. the field strength required for pressure equilibrium ( $k = 1$ , $\phi = 1$ ). <i>Right:</i> The same, but for $k = 100$ . . . . .	61
4.4 The spectra of the radio lobes. . . . .	66
4.5 The synchrotron age corrected for adiabatic-expansion losses versus the buoyancy age. . . . .	70
4.6 <i>Left:</i> Mechanical luminosity (cavity power) vs. radio luminosity; <i>Right:</i> The ratio of mechanical luminosity to $\nu P_\nu$ at 1400 MHz vs. radio luminosity. . . . .	74
4.7 Cavity power (mechanical luminosity) versus bolometric radio power for the expanded 24-system sample for the total source ( <i>left</i> ) and lobes only ( <i>right</i> ). . . . .	79
4.8 <i>Left:</i> The ratio of cavity power to lobe bolometric radio power versus the break frequency (corrected for adiabatic expansion). <i>Right:</i> The ratio of cavity energy ( $4pV$ ) to lobe bolometric radio power versus the break frequency (corrected for adiabatic expansion). . . . .	81

4.9 *Left:* Cavity energy inferred from the 1400 MHz radio emission versus that inferred from the X-ray data. *Right:* Cavity energy inferred from the 327 MHz radio emission versus that inferred from the X-ray data. 85

B.1 Radio contours . . . . .	123
B.2 Radio contours – continued . . . . .	124
B.3 Radio contours – continued . . . . .	125
B.4 Radio contours – continued . . . . .	126
B.5 Radio contours – continued . . . . .	127
B.6 Radio contours – continued . . . . .	128
B.7 Radio contours – continued . . . . .	129
B.8 Radio contours – continued . . . . .	130
B.9 Radio contours – continued . . . . .	131
B.10 Radio contours – continued . . . . .	132
B.11 Radio contours – continued . . . . .	133
B.12 Radio contours – continued . . . . .	134
B.13 Radio contours – continued . . . . .	135
B.14 Radio contours – continued . . . . .	136
B.15 Radio contours – continued . . . . .	137
B.16 Radio contours – continued . . . . .	138
B.17 Radio overlays (green) on the smoothed <i>Chandra</i> X-ray images . . .	139
B.18 Radio overlays – continued . . . . .	140

B.19 Radio overlays – continued . . . . .	141
B.20 Radio overlays – continued . . . . .	142
B.21 Radio overlays – continued . . . . .	143
B.22 Radio overlays – continued . . . . .	144
B.23 Radio overlays – continued . . . . .	145
B.24 Radio overlays – continued . . . . .	146
B.25 Radio overlays – continued . . . . .	147

# CHAPTER 1

## Introduction

Clusters of galaxies are the largest gravitationally bound systems in the Universe. They are small enough to achieve an equilibrium during the age of the Universe and big enough to contain a sizable sample of the material that the Universe is made of. These characteristics make them an important cosmological probe.

Galaxy clusters were first studied in the optical by Wolf in 1906 where they appeared as a concentration of hundreds of bright galaxies and thousands of faint ones spread over an approximate size of  $10^{25}$  cm and with a total mass that exceeds  $10^{48}$  g. Morphologically, clusters of galaxies can be classified from regular to irregular following the Abell classification (Abell's 1958 catalog) or from compact to open following the Zwicky classification (Zwicky's 1961-1968 catalog) and they can be either rich or poor depending on the number of the galaxies in the cluster. Rich clusters of galaxies are often dominated by cD or very bright galaxies, while the less dense clusters usually contain spiral galaxies. Today it is well known that the contribution of the galaxies to the total mass of the cluster is only about  $\sim 3\%$ . Up to  $\sim 16\%$  of the cluster mass is in the form of hot diffuse gas, known as the intracluster medium (ICM), first detected through its X-ray emission in 1966 in the galaxy M87 situated at the center of the Virgo cluster. The remaining  $\sim 81\%$  of cluster mass consists of dark matter which is most likely nonbarionic ([Sarazin, 1988](#)).

Today it is known that clusters of galaxies are the second most luminous X-ray sources in the Universe after quasars with  $L_X \sim 10^{43} - 10^{45}$  erg s $^{-1}$ . Due to the very high temperatures ( $T \sim 10^7$  K), the dominant emission process in clusters is thermal bremsstrahlung (free-free radiation) whereas line emission becomes important at lower temperatures. The ICM is rarefied, with the electron density  $n_e$  ranging from  $\sim 10^{-2}$  cm $^{-3}$  in the cluster cores and then decreasing outward. The gas metallicity is a fraction of the solar metallicity and in almost solar proportions, implying that some of the gas comes from the stars in the galaxies (for reviews see Sarazin, 1988, 2003).

The thermal plasma is the dominant constituent of the ICM, but magnetic fields and non-thermal particles are also present (Sarazin, 2003). The magnetic field strengths derived from Faraday rotation measurements are typically about 5  $\mu$ G (Clarke et al., 2001).

## 1.1 The Cooling Flow Problem

In the last two decades a hotly discussed subject in the study of clusters of galaxies was the “cooling flow problem”. Clusters are classified as *cooling flow clusters* when the cooling time, the time for the gas to radiate away all its thermal energy, is much shorter than the age of the cluster; otherwise, they are classified as *non-cooling flow clusters*. The cooling is most effective in the central region of the cluster, known as the *cooling flow region*, where the density is higher and the temperature lower. As the

gas cools down, the weight of the outer layers compresses the inner ones and replaces the gas that has cooled and dropped out of hydrostatic equilibrium. In this classic model, the expected cooling flow rates are  $\sim 100 - 1000 \text{ M}_\odot \text{ yr}^{-1}$  (for a review see [Fabian, 1994](#)).

Recent X-ray observations have forced changes in the classic cooling flow model. With moderate- and high-resolution X-ray telescopes such as ASCA, *Chandra* and XMM-*Newton*, the expected signatures of cooling were not detected (for a review of X-ray spectroscopy, see [Peterson & Fabian, 2006](#)). The cooling flow rates derived from these data are generally a factor of 5 – 10 lower than expected ([Molendi & Pizzolato, 2001](#); [Peterson et al., 2001, 2003](#); [Peterson & Fabian, 2006](#)). To account for the missing signs of cooling seen in the new observations, several scenarios have been proposed. These include differential absorption, efficient mixing, or an inhomogeneous metallicity distribution ([Fabian et al., 2001](#)), all of which attempt to explain the lack of cooling signatures while maintaining the large classical cooling rates. However, these scenarios predict large amounts of cold gas and star formation, which are not observed. The alternative is that the gas is prevented from cooling, either from heating by conduction ([Zakamska & Narayan, 2003](#); [Voigt & Fabian, 2004](#)) or heating by the active galactic nuclei (AGN; [Tabor & Binney, 1993](#); [Binney & Tabor, 1995](#); [Ciotti & Ostriker, 2001](#)). Heating by conduction, however, has been found in simulations to be unstable and does not reproduce the temperature profiles observed in clusters

(Peterson & Fabian, 2006). Therefore, heating by the AGN has emerged as the most promising mechanism to counter the cooling.

There are two alternatives for the degree of feedback between the AGN and the cooling ICM: the first is one in which the cooling flows in clusters are prevented altogether, with the gas not being able to cool below X-ray temperatures (Churazov et al., 2002; Omma et al., 2004); the other is one in which small amounts of gas are allowed to cool below X-ray temperatures, and the black hole accretes cold gas (Soker et al., 2001; Pizzolato & Soker, 2005; Soker & Pizzolato, 2005; Soker, 2006). The presence of moderate amounts of star formation (McNamara & O'Connell, 1992) and cold gas (Edge et al., 2002) in many systems tends to favor the latter scenario.

## 1.2 The Interaction of the AGN with the ICM: X-ray Cavities

Observations show that large galaxies, such as cD galaxies, contain supermassive black holes (SMBH) with  $M \gtrsim 10^8 M_\odot$ . When a SMBH accretes gas from its environment, a radio source is formed. The central region of the active radio galaxy generates a large amount of energy from the SMBH, with the release of the gravitational energy of the accreting material. In the case of cooling flow clusters, the central dominant galaxy, usually a cD galaxy, harbors a radio galaxy  $\sim 71\%$  of the time compared to

just  $\sim 23\%$  in the case of non-cooling flow clusters (Burns, 1990). This suggests a connection between AGN activity and the cooling flow in clusters.

The AGNs convert the gravitational energy of the accreting material into kinetic energy in a pair of oppositely directed jets which are highly collimated and composed of relativistic particles. These jets lose energy by doing work against the ICM until they come into pressure equilibrium with the ICM. At this point, they inflate lobes filled with relativistic particles and magnetic fields which emit synchrotron radiation detected as radio waves. The shape of the radio sources are determined by the details of the interaction of the jets with the ICM. In the case of radio sources in cooling flow clusters, the jets are collimated only on kpc scales, after which the lobes become large bubbles. Such interactions have been extensively modeled in the literature (e.g., Scheuer, 1974; Blandford & Rees, 1974; Begelman & Cioffi, 1989; Kaiser & Alexander, 1997; Heinz et al., 1998).

However, it was not until the advent of high-resolution images from *Chandra* that the strong coupling between the relativistic plasma in radio sources and the thermal gas in clusters was discovered: where the X-ray images show cavities in the surface brightness, the radio maps show an enhancement of emission. There are many examples in the literature of X-ray cavities associated with bright radio lobes, for example Perseus (Fabian et al., 2000), Hydra A (McNamara et al., 2000), Abell 2052 (Blanton et al., 2001), Cygnus A (Smith et al., 2002), and M87 (Young et al., 2002) among many others (Bîrzan et al., 2004). The idea is that the radio-filled lobes should

have a smaller specific weight than the ambient gas and act like bubbles that detach themselves and rise buoyantly. These X-ray cavities are known in the literature as “radio-filled cavities” or “active cavities”. These cavities are on average  $\sim 10$  kpc in radius and are situated at a similar distance from the cluster center. Often, they are surrounded by bright rims, evidence that the bubbles have cold rims of low-entropy gas that has been uplifted during their expansion and rise.

*Chandra* also revealed cavities which are not associated with bright radio lobes, for example Abell 2795 (McNamara et al., 2001) or the outer cavities in Perseus (Fabian et al., 2000). These X-ray cavities are known as “ghost cavities” and are interpreted to be buoyantly rising relics of a radio source that is not active anymore.

This scenario of a buoyantly rising bubble has been modeled by hydrodynamical and magnetohydrodynamical simulations. One type of simulations uses an ad-hoc release of energy and mass at some fixed distance from the center of the AGN (e.g., Brüggen & Kaiser, 2001; Churazov et al., 2001; Quilis et al., 2001; Brüggen et al., 2002; Brüggen, 2003; Robinson et al., 2004; Jones & De Young, 2005; Dalla Vecchia et al., 2004; Ruszkowski et al., 2004; Reynolds et al., 2005). In this scenario, the rising bubbles uplift cold material from the center of the cluster to large distances where they are in pressure equilibrium with the surrounding medium. Some of this uplifted material, when the energy injection is turned off, can fall back toward the black hole, re-energizing the AGN and starting the feedback process. Robinson et al. (2004) and Jones & De Young (2005) show that a magnetic field is necessary in order to be able to

see the ghost cavities. However, recent simulations by Pizzolato & Soker (2006) show that the magnetic field is not necessary to explain the long term stability of cavities, because in an early stage of the bubbles' evolution, when they are inflated by the radio jets, a drag effect is induced which will prevent the Rayleigh-Taylor instabilities that can break the bubbles. The instabilities set in and eventually disrupt the bubbles in a later stage when the radio jets fade. Ruszkowski et al. (2004) and Reynolds et al. (2005) show that the viscosity can be important in maintaining the integrity of the bubbles.

Other simulations are more realistic. They simulate the jets by injecting gas at high velocities, and they consider both the active phase of the radio source and the inactive phase after the jets stop the energy injection into the lobes and when the buoyant phase of the remnants of the radio source starts (e.g., Reynolds et al., 2002; Basson & Alexander, 2003; Omma et al., 2004). However, these supersonic jets create strong shocks, which are not seen in *Chandra* data. A weakness of these simulations is that they use a spherically symmetric analytical profile for the ICM. More recently, Heinz et al. (2006) simulate both the jets and the cluster gas and found that the dynamic of the cluster is important to the evolution of the radio lobes, and may solve the problems discussed by Vernaleo & Reynolds (2006) when they simulated jets in a spherical symmetric cluster model.

Some simulations have included both heating by AGNs and heating by conduction (e.g., Ruszkowski & Begelman, 2002). Brighenti & Mathews (2002b) and Brighenti &

Mathews (2003) have done numerical simulations which reproduced the lower cooling rates that we see in observations, and Dalla Vecchia et al. (2004) show that the energy injected effectively balances the cooling lost and preserves the temperature profile. Furthermore, Brighenti & Mathews (2002a), both through computational and analytical calculations, show that the rims of the bubbles should be cool, in agreement with the observations (e.g., Blanton, 2004).

However, there are many questions still to be answered:

- ◊ How are the luminous energies and mechanical energies of the radio sources related – what are the radiative efficiencies of the radio sources, and can radio observations be used as proxies for X-ray observations in distant systems?
- ◊ What comprises the radio lobes, and are they light (electron-positron) or heavy (electron-proton)?
- ◊ How are the synchrotron and buoyancy ages related?
- ◊ How are the bubbles pressure supported – by the magnetic fields, by hot gas, or by the particles in the lobes?

The discovery of the X-ray cavities has made it possible to quantify the jet power independently of the radio observations. In general, the cavities are good calorimeters of the total jet power; therefore, they can be used, together with the radio data, to estimate the jet content, radiative efficiencies, and magnetic field strengths. The total

energy in the radio lobes is the sum of magnetic and particle energies:  $E_{\text{tot}} = E_B + E_p$ .

For the first time, the cavities allow one to estimate  $E_{\text{tot}}$  to within a factor of a few.

Additionally, the cavities can be used to estimate of the pressures and ages of the lobes. Together, these quantities break the degeneracies in the energy equation and allow meaningful constraints to be placed on the magnetic field strengths and particle content of the lobes.

In this dissertation, we use VLA<sup>1</sup> radio data at 4 different frequencies for a sample of 24 systems with X-ray cavities to investigate the radiative efficiencies. We derive synchrotron break frequencies and ages and, using both X-ray and radio data, we place limits on the magnetic field strengths and on the particle content (more specifically, the ratio of the heavy-particle energy to the electron energy) present in the cavities. We then investigate the effects that differences in the radio source ages or magnetic field strengths and particle content has on the efficiencies.

Furthermore, using both the X-ray and radio data, we investigate the radio source age, by comparing the synchrotron ages with the buoyancy ages. In general the synchrotron ages are lower limits on the radio source age (Eilek, 1996; Eilek et al., 1997; Eilek, 1999) due to the homogeneities in the magnetic field, which is difficult to estimate (Siah & Wiita, 1990; Wiita & Gopal-Krishna, 1990). The X-ray derived ages (e.g., buoyancy ages) assume that the bubbles detach early from the driving jet and rise buoyantly in the ICM. By finding discrepancies between the two ages, we

---

<sup>1</sup>The VLA (Very Large Array) is a facility of the National Radio Astronomy Observatory (NRAO). The NRAO is a facility of the National Science Foundation operated under cooperative agreement by Associated Universities, Inc.

can test the assumptions that go into their determination. Lastly, on a related topic, we are now able to determine more precisely whether a cavity is radio filled or ghost (as discussed above).

We adopt  $H_0 = 70 \text{ km s}^{-1} \text{ Mpc}^{-1}$ ,  $\Omega_M = 0.3$ , and  $\Omega_\Lambda = 0.7$  in all calculations throughout this paper.

# CHAPTER 2

## The Sample

Since our study was done over some time, we have two samples: an initial sample and an extended, updated sample that shares many of the same objects. The primary difference between the samples is that for the initial sample we relied on inhomogeneous radio data taken from the literature, whereas for the extended sample we obtained a high-quality, homogeneous set of radio data.

The initial sample of 18 systems ([Bîrzan et al., 2004](#)) was selected by visually inspecting  $\sim 80$  systems in the *Chandra* Data Archive for surface brightness depressions associated with their radio sources (see Table 2.1). The sample consists of 16 galaxy clusters, one galaxy group (HCG 62), and one giant elliptical galaxy (M84), ranging in redshift from  $z = 0.0035$  (M84) to  $z = 0.35$  (RBS 797), and in X-ray luminosity from  $\sim 10^{41}$  erg s $^{-1}$  (M84) to  $4 \times 10^{45}$  erg s $^{-1}$  (RBS 797). We avoided depressions with questionable association with a radio source, and we excluded clusters in which there is clear evidence for merging, since merging clusters often show complex structure that can be mistaken for a radio-induced cavity. All clusters in our sample were previously reported in the literature as containing cavities likely to be associated with radio bubbles.

The expanded sample includes these 18 systems plus 6 new cavity systems recently discovered by *Chandra* (A1835, Sersic 159/03, Zw 2701, Zw 3146, MACS

J1423.8+2404 and MS 0735.6+7421). This sample consist of 22 galaxy clusters, one galaxy group (HCG 62) and one elliptical galaxy, M84. There is a broad range in redshift from 0.0035 (M84) to 0.545 (MACS J1423.8+2404) and a broad range in radio luminosity from  $2.2 \times 10^{39}$  erg s<sup>-1</sup> (HCG 62) to  $7.75 \times 10^{45}$  erg s<sup>-1</sup> (Cygnus A). See Table 2.3 for the general properties of the extended sample.

Table 2.1. Initial Sample Properties.

System	z	$\sigma$ (ref) <sup>a</sup> (km s <sup>-1</sup> )	$S_{1400}$ (Jy)	$\alpha$ (ref) <sup>b</sup>	$P_{1400}$ (10 <sup>24</sup> W Hz <sup>-1</sup> )	$L_{\text{radio}}$ (10 <sup>42</sup> ergs s <sup>-1</sup> )
Cygnus A	0.056	...	1598±41	0.7 (4)	11800±300	700±20
Hydra A	0.052	322±20 (8)	40.8±1.3	0.92 (4,13)	261±8	19.9±0.6
A2597	0.085	224±19 (16)	1.875±0.056	1.35 (11)	35±1	6.8±0.2
MKW 3S	0.045	...	115.0±3.9	2.3 (4,13,17)	0.58±0.02	3.6±0.1
A2052	0.035	253±12 (19)	5.50±0.21	1.2 (1,4,13)	15.7±0.6	2.08±0.08
A133	0.060	...	0.167±0.006	1.9 (14,15)	1.54±0.06	1.94±0.07
A4059	0.048	296±49 (6)	1.284±0.043	1.43 (13,18,21)	6.96±0.2	1.73±0.06
A2199	0.030	295±6 (7)	3.58±0.12	1.37 (1,4,17)	7.43±0.2	1.56±0.05
Perseus	0.018	246±10 (8)	22.83±0.68	1.0 (10)	16.5±0.5	1.42±0.04
RBS 797	0.350	...	0.0217±0.0008	...	9.0±0.3	0.78±0.03
A1795	0.063	297±12 (3)	0.925±0.028	0.98 (1,4,13)	9.0±0.3	0.75±0.02
M87	0.0042	330±5 (2)	138.5±4.9	0.81 (4,9,13)	5.48±0.2	0.36±0.01
Centaurus	0.011	256±11 (5)	3.8	0.7 (4,9,14,20)	1.1	0.060
A478	0.081	...	0.0369±0.0015	...	0.60±0.02	0.052±0.002
M84	0.0035	278±4 (8)	6.00±0.15	0.63 (4,9,17)	0.162±0.004	0.0089±0.0002
2A 0335+096	0.035	...	0.0367±0.0018	0.9 (12)	0.104±0.005	0.0077±0.0004
A262	0.016	...	0.0657±0.0023	0.6 (4)	0.039±0.001	0.00210±0.00007
HCG 62	0.014	...	0.0049±0.0005	...	0.0021±0.0002	0.00018±0.00002

<sup>a</sup>When no velocity dispersion was available,  $\langle \sigma \rangle = 280$  km s<sup>-1</sup> was adopted. References are in parentheses.

<sup>b</sup>The spectral index is defined so that  $S \sim \nu^{-\alpha}$ . When no spectral index was available,  $\alpha = 1$  was adopted. References are in parentheses.

References. — (1) Becker et al. (1991); (2) Bender et al. (1994); (3) Blakeslee & Tonry (1992); (4) Burbidge & Crowne (1979); (5) Carollo et al. (1993); (6) Carter et al. (1985); (7) Fisher et al. (1995); (8) Heckman et al. (1985); (9) Kuehr et al. (1981); (10) Pedlar et al. (1990); (11) Sarazin et al. (1995b); (12) Sarazin et al. (1995a); (13) Slie (1995); (14) Slie & Siegmund (1988); (15) Slie et al. (2001); (16) Smith et al. (1990); (17) Spinrad et al. (1985); (18) Taylor et al. (1994); (19) Tonry (1985); (20) Wright et al. (1994); (21) Wright et al. (1996).

## 2.1 X-Ray Data Reduction and Analysis for the Initial Sample of 18 Systems

### 2.1.1 X-Ray Analysis

For the initial sample of 18 systems (Bîrzan et al., 2004) the X-ray data were obtained through the *Chandra* Data Archive and were reprocessed with CIAO, version 2.3, using CALDB, version 2.21. Of the 18 systems, 16 were imaged with the ACIS-S3 detector and two with the ACIS-I3 detector (RBS 797 and MKW 3S), with exposure times ranging from 12 ksec (RBS 797) to 50 ksec (HCG 62). The charge transfer inefficiency (CTI) correction was applied during reprocessing of the level 1 event file. Blank-sky background files were used for background subtraction for all clusters.<sup>1</sup> The background files were normalized to the count rate of the source image in the 10-12 keV band, after the removal of all bright emission. The required adjustment was less than 12% for all clusters except Centaurus and Perseus, which both required background adjustments of  $\sim 30\%$ . Spectra with at least 2000 counts were extracted in circular annuli centered on the X-ray centroid of the cluster. Response files were made using the CIAO tools *mkrmf* and *mkwarf*. We attempted to correct the resulting ARFs for the quantum efficiency degradation problem using the *corarf* tool.<sup>2</sup> However, upon spectral fitting, we found that  $\sim 75\%$  of our sample was

---

<sup>1</sup>See <http://asc.harvard.edu/contrib/maxim/acisbg/>

<sup>2</sup>See [http://asc.harvard.edu/cal/Acis/Cal\\_prods/qeDeg/](http://asc.harvard.edu/cal/Acis/Cal_prods/qeDeg/)

overcorrected by *corrarf*. Therefore, we present our results without the correction applied (for a discussion of this problem, see Voigt & Fabian (2004)). In general, the largest effect of using *corrarf* was on the cooling rates, which increased on average by a factor of 2 after the correction was applied. To find radial temperatures and densities, we deprojected the spectra extracted above. The deprojection was performed assuming spherical symmetry and using the PROJCT model in XSPEC 11.2.0 with a single-temperature plasma model (MEKAL) and foreground absorption (WABS), fitted between energies of 0.5 and 7.0 keV. The foreground column density,  $N_{\text{H}}$ , was tied between annuli and allowed to vary. The MEKAL abundance was also free to vary. The redshift was fixed to the value given in Table 2.1. The density was then calculated from the normalization of the MEKAL component, assuming  $n_{\text{e}} = 1.2n_{\text{H}}$  (for a fully ionized gas with hydrogen and helium mass fractions of  $X = 0.7$  and  $Y = 0.28$ ). The pressure in each annulus was calculated as  $P = nkT$ , where we have assumed an ideal gas and  $n \approx 2n_{\text{e}}$ .

### 2.1.2 X-Ray Surface Brightness Depressions

For the initial 18 systems sample (Bîrzan et al., 2004), in total, 36 surface brightness depressions or cavities were identified. Table 2.2 lists the cavity properties. For each cavity, a size and position were measured, assuming the cavity extends to the inner edge of any bright surrounding emission. The projected shapes of the cavities were measured by eye as circles or ellipses from the exposure-corrected, unsmoothed

images. This is a qualitative measurement, the accuracy of which depends on the signal-to-noise ratio of the image and on the contrast of the cavity with its surroundings. To distinguish between the poorly defined and well-defined cavities, we have assigned a figure of merit (FOM) to each cavity ranging from 1 for the best-defined cavities – those with surrounding bright rims – to 3 for the worst-defined ones without bright rims.

Table 2.2. Cavity properties.

System	Cavity Type (FOM) <sup>a</sup>	$a^b$ (kpc)	$b^c$ (kpc)	$R^d$ (kpc)	$pV^e$ ( $10^{57}$ ergs)	$t_{c_s}$ (10 <sup>7</sup> yr)	$t_{\text{buoy}}$ (10 <sup>7</sup> yr)	$t_r$ (10 <sup>7</sup> yr)	ref
RBS 797	G (2)	9.7	9.7	19.5	$190^{+340}_{-120}$	1.4	3.6	6.8	18
	G (2)	13.4	8.5	23.8	$190^{+150}_{-40}$	1.7	5.2	7.8	
A478	F (2)	5.5	3.4	9.0	$5.8^{+4.4}_{-1.3}$	1.1	1.9	3.1	20
	F (2)	5.6	3.4	9.0	$6.0^{+4.3}_{-1.3}$	1.1	1.9	3.1	
A1795	G (3)	18.5	7.2	18.5	$39^{+53}_{-4}$	1.8	3.7	6.8	5
	F (1)	4.7	4.7	7.0	$12^{+21}_{-8}$	0.6	1.3	3.2	6,7
Perseus	F (1)	7.3	6.3	11.2	$24^{+34}_{-13}$	1.0	2.1	4.8	
	G (1)	12.9	6.3	29.7	$24^{+12}_{-1}$	3.0	9.4	9.1	
Cygnus A	G (2)	13.6	4.8	36.7	$14^{+25}_{-1}$	3.6	15.1	9.7	
	F (1)	29.0	17.2	43.0	$470^{+300}_{-30}$	3.2	8.9	15.3	19
A2597	F (1)	33.8	23.1	44.7	$930^{+860}_{-230}$	3.3	8.1	17.4	
	G (2)	10.2	7.1	22.6	$21^{+20}_{-5}$	2.6	6.6	8.6	15
G (2)	G (2)	7.1	7.1	23.1	$14^{+26}_{-9}$	2.6	6.8	7.9	
	G (2)	9.3	6.5	23.1	$9.7^{+9.6}_{-2.8}$	3.2	5.7	6.6	13
2A 0335+096	G (3)	4.8	2.6	27.5	$0.79^{+0.40}_{-0.02}$	3.9	11.7	4.8	
	F (2)	17.7	11.8	28.5	$83^{+73}_{-17}$	3.0	5.1	8.7	4,14,16
Hydra A	F (2)	19.9	11.7	33.8	$87^{+57}_{-7}$	3.2	5.6	9.3	
	F (2)	6.5	6.5	18.9	$6.6^{+11.9}_{-4.3}$	2.1	4.0	5.2	11
A2199	F (2)	6.2	3.5	21.2	$1.8^{+1.1}_{-0.1}$	2.2	6.5	4.7	
	G (3)	53.9	22.6	58.7	$300^{+310}_{-14}$	5.8	12.4	22.3	12
A2052	F (1)	6.5	6.0	6.7	$3.2^{+5.0}_{-1.8}$	1.1	1.0	3.5	1,2
	F (1)	10.7	7.8	11.2	$8.4^{+8.8}_{-2.8}$	1.8	2.0	5.5	
A4059	G (2)	9.2	9.2	19.3	$8.9^{+16.3}_{-6.0}$	2.8	3.5	6.2	10
	G (2)	20.4	10.1	22.7	$24^{+11}_{-3}$	2.6	4.2	8.4	
A133	F (2)	9.8	5.2	28.1	$3.4^{+1.7}_{-1.7}$	3.5	8.6	7.0	9
	F (2)	9.8	5.7	32.7	$4.0^{+2.7}_{-0.1}$	3.9	10.2	7.7	
Centaurus	F (3)	3.3	1.6	3.5	$0.196^{+0.10}_{-0.003}$	0.7	0.7	1.5	17
	F (2)	3.3	2.4	6.0	$0.40^{+0.42}_{-0.13}$	1.0	1.3	2.2	

Table 2.2 (continued)

System	Cavity Type (FOM) <sup>a</sup>	$a^b$ (kpc)	$b^c$ (kpc)	$R^d$ (kpc)	$pV^e$ ( $10^{57}$ ergs)	$t_{c_s}$ ( $10^7$ yr)	$t_{\text{buoy}}$ ( $10^7$ yr)	$t_r$ ( $10^7$ yr)	ref
A262	G (2)	2.6	2.6	6.2	$0.17^{+0.32}_{-0.11}$	1.1	1.3	2.0	3
	G (3)	3.3	2.6	6.7	$0.21^{+0.27}_{-0.10}$	1.2	1.4	2.2	
M87	F (2)	1.6	0.8	2.2	$0.078^{+0.043}_{-0.003}$	0.4	0.4	0.6	22
	F (2)	2.3	1.4	2.8	$0.25^{+0.18}_{-0.02}$	0.4	0.4	0.9	
HCG 62	G (2)	5.0	4.3	8.4	$0.29^{+0.41}_{-0.15}$	1.8	1.5	3.1	21
	G (2)	4.0	4.0	8.6	$0.21^{+0.37}_{-0.13}$	1.9	1.6	2.9	
M84	F (2)	1.6	1.6	2.3	$0.019^{+0.035}_{-0.013}$	0.5	0.4	1.0	8
	F (2)	2.1	1.2	2.5	$0.013^{+0.007}_{-0.001}$	0.6	0.5	1.0	

<sup>a</sup>Radio-filled cavities are denoted by “F,” radio-faint ghosts are denoted by “G.” The FOM gives a relative measure of the cavity’s contrast to its surroundings: (1) high contrast: bright rim surrounds cavity; (2) medium contrast: bright rim partially surrounds cavity; and (3) low contrast: no rim or faint rim surrounds cavity.

<sup>b</sup>Projected semimajor axis of the cavity.

<sup>c</sup>Projected semiminor axis of the cavity.

<sup>d</sup>Projected distance from the cavity center to the radio core.

<sup>e</sup>The errors in  $pV$  include an estimate of the projection effects; see the text for details.

References. — (1) Blanton et al. (2001); (2) Blanton et al. (2003); (3) Blanton (2004); (4) David et al. (2001); (5) Ettori et al. (2002); (6) Fabian et al. (2000); (7) Fabian et al. (2002); (8) Finoguenov & Jones (2001); (9) Fujita et al. (2002); (10) Heinz et al. (2002); (11) Johnstone et al. (2002); (12) Mazzotta et al. (2002); (13) Mazzotta et al. (2003); (14) McNamara et al. (2000); (15) McNamara et al. (2001); (16) Nulsen et al. (2002); (17) Sanders & Fabian (2002); (18) Schindler et al. (2001); (19) Smith et al. (2002); (20) Sun et al. (2003); (21) Vrtilek et al. (2002); (22) Young et al. (2002).

In the analysis that follows, we assumed that the cavities are bubbles devoid of gas at the local ambient temperature (McNamara et al., 2000; Blanton et al., 2003). Their volumes were calculated assuming spherical or prolate ellipsoidal shapes, with semimajor axis  $a$  and semiminor axis  $b$ . The errors in the volumes due to projection were estimated by allowing each bubble to have an intrinsic  $a/b$  as large as that of the most eccentric cavity observed in the sample,  $(a/b)_{\max}$ . The upper and lower limits are calculated assuming either oblate or prolate symmetry. In this sense, spherical bubbles have the greatest range of possible volumes, while projected ellipses with an  $a/b = (a/b)_{\max}^{2/3}$  have the smallest range. The pressure and temperature of the gas surrounding the cavity were taken to be the azimuthally averaged values at the projected radius of its center.

For the extended, 24-system sample we did not analyze the X-ray data. The X-ray information that we used (see Section 3.1) are taken from Rafferty et al. (2006).

## 2.2 Radio Reduction and Analysis for the Extended 24-System Sample

### 2.2.1 Radio Observations and Data Reduction

In order to accurately measure the synchrotron spectrum and the bolometric flux for the 24 systems in our sample, we used VLA radio data at 327 MHz, 1.4 GHz, 4.5 GHz and 8.5 GHz. We obtained new VLA observations for 13 objects that did

not have VLA archival data at one or more of these frequencies. The observations that we used for each frequency are given in Table A.1. Data were analyzed with the Astronomical Image Processing System (AIPS). The primary flux density calibrators and the phase calibrators are listed in Table A.1. The data were Fourier-transformed, cleaned, restored, and self-calibrated with AIPS. In order to subtract confusing sources we imaged the entire primary beam. Table A.2 gives the resolution, position angle and the RMS noise of the final radio images for at least three different frequencies (327 MHz, 1.4 GHz, 4.5 GHz and/or 8.5 GHz). Where available, data at different arrays were added for better u-v coverage. In some cases we show images at different resolutions for the same frequency: A133 at 330 MHz and 1.4 GHz, RBS 797 at 1.4 GHz and 8.5 GHz, and A1835 at 1.4 GHz.

Table 2.3. Radio fluxes, spectral indices, and radio luminosities

Name	z	Component	$S_{327}$ (Jy)	$S_{1400}$ (Jy)	$S_{4500}$ (Jy)	$S_{8500}$ (Jy)	$\alpha^a$	$L_{\text{radio}}^{\text{b}}$ ( $10^{42} \text{ erg s}^{-1}$ )
A133	0.060	lobes	$3.5 \pm 0.2$	$0.125 \pm 0.006$	...	...	$2.28 \pm 0.04$	$7.6 \pm 1.2$
		core	$0.11 \pm 0.01$	$0.0072 \pm 0.0003$	$0.00058 \pm 0.0004$	$0.0029 \pm 0.0001$	$1.87 \pm 0.04$	$0.08 \pm 0.01$
A262	0.016	lobes	$0.244 \pm 0.015$	$0.047 \pm 0.004$	...	...	$1.14 \pm 0.07$	$0.0033 \pm 0.0003$
		core	$0.055 \pm 0.002$	$0.026 \pm 0.001$	...	$0.0042 \pm 0.0002$	$0.52 \pm 0.04$	$0.0011 \pm 0.0001$
Perseus	0.018	lobes	$15.7 \pm 1.3$	$1.9 \pm 1.3$	...	...	$1.7 \pm 0.5$	$1.1^{+1.2}_{-0.6}$
		core	$8.9 \pm 0.4$	$21.4 \pm 0.9$	...	$23.9 \pm 1.0$	$-0.56 \pm 0.04$	$2.7 \pm 0.4$
2A 0335+096	0.035	lobes	$0.13 \pm 0.02$	$0.015 \pm 0.002$	$0.0039 \pm 0.0007$	...	$1.16 \pm 0.12$	$0.009 \pm 0.002$
		core	$0.083 \pm 0.005$	$0.015 \pm 0.001$	$0.0063 \pm 0.0003$	$0.0040 \pm 0.0002$	$1.13 \pm 0.05$	$0.0055 \pm 0.0005$
A478	0.081	lobes	$0.048 \pm 0.016$	$0.008 \pm 0.002$	...	...	$1.2 \pm 0.3$	$0.02 \pm 0.01$
		core	$0.067 \pm 0.006$	$0.0193 \pm 0.0008$	...	$0.0054 \pm 0.0002$	$0.83 \pm 0.07$	$0.025 \pm 0.003$
MS 0735.6+7421	0.216	lobes	$0.72 \pm 0.04$	$0.0117 \pm 0.0012$	...	...	$1.87 \pm 0.04$	$130 \pm 40$
		core	$0.079 \pm 0.003$	$0.0087 \pm 0.0004$	...	$0.00081 \pm 0.0004$	$2.80 \pm 0.08$	$0.43 \pm 0.05$
Hydra A	0.055	outer lobes	$40 \pm 10$	...	...	...	$1.2 \pm 0.2$	$5.9 \pm 1.5$
		inner lobes	$116 \pm 5$	$39.1 \pm 1.6$	$14.8 \pm 0.6$	$7.2 \pm 0.3$	$0.43 \pm 0.04$	$29 \pm 5$
RBS 797	0.350	core	$0.070 \pm 0.006$	$0.14 \pm 0.01$	$0.25 \pm 0.01$	$0.27 \pm 0.01$	$-0.48 \pm 0.08$	$0.14 \pm 0.03$
		lobes	$0.070 \pm 0.007$	$0.0091 \pm 0.0015$	$0.0018 \pm 0.0003$	$0.0011 \pm 0.0002$	$1.35 \pm 0.13$	$0.9 \pm 0.3$
Zw 2701	0.214	core	$0.034 \pm 0.002$	$0.0113 \pm 0.0005$	$0.0023 \pm 0.0001$	$0.00156 \pm 0.0006$	$0.73 \pm 0.04$	$0.33 \pm 0.03$
		lobes	$0.184 \pm 0.014$	...	...	...	...	$0.67 \pm 0.05$
Zw 3146	0.291	core	$0.030 \pm 0.003^c$	...	$0.0043 \pm 0.0002$	$0.0029 \pm 0.0001$	$0.7 \pm 0.1$	$0.10 \pm 0.02$
		lobes	$0.028 \pm 0.003$	...	$0.00139 \pm 0.00007$	$0.00078 \pm 0.00005$	$1.04 \pm 0.14$	$0.17 \pm 0.03$
M84	0.00335	lobes	$1.1 \pm 0.5$	$5.38 \pm 0.23$	$2.07 \pm 0.09$	$1.26 \pm 0.07$	$0.48 \pm 0.04$	$0.0106 \pm 0.0012$
		core	$0.16 \pm 0.01$	$0.232 \pm 0.009$	$0.208 \pm 0.008$	$0.25 \pm 0.01$	$-0.26 \pm 0.05$	$0.00082 \pm 0.00017$
M87	0.00442	lobes	$119 \pm 5$	$133 \pm 6$	$54 \pm 3$	$44 \pm 2$	$0.69 \pm 0.05$	$0.63 \pm 0.05$
		core	$4.96 \pm 0.19$	$5.6 \pm 0.2$	$5.1 \pm 0.2$	$3.62 \pm 0.15$	$0.34 \pm 0.05$	$0.017 \pm 0.002$
Centaurus	0.011	lobes	$7.1 \pm 0.7$	$2.82 \pm 0.16$	$1.24 \pm 0.06$	$0.77 \pm 0.04$	$0.59 \pm 0.07$	$0.063 \pm 0.013$
		core	$5.2 \pm 0.2$	$0.58 \pm 0.02$	$0.132 \pm 0.005$	$0.079 \pm 0.003$	$1.40 \pm 0.04$	$0.047 \pm 0.004$
HCG 62	0.014	lobes	...	$0.0012 \pm 0.0005$	...	...	...	$0.00005 \pm 0.00002$
		core	$0.0081 \pm 0.0018$	$0.0038 \pm 0.0002$	...	$0.00147 \pm 0.00006$	$0.59 \pm 0.16$	$0.00012 \pm 0.00006$
A1795	0.063	lobes	$2.73 \pm 0.14$	$0.72 \pm 0.04$	...	$0.0660 \pm 0.0005$	$0.88 \pm 0.05$	$0.60 \pm 0.04$
		core	$0.63 \pm 0.03^c$	$0.162 \pm 0.007$	...	$0.033 \pm 0.001$	$0.91 \pm 0.03$	$0.138 \pm 0.007$
A1835	0.253	lobes	$0.05 \pm 0.01$	$0.012 \pm 0.002$	...	...	$1.04 \pm 0.18$	$0.23 \pm 0.06$
		core	$0.043 \pm 0.003^c$	$0.020 \pm 0.001^c$	$0.0099 \pm 0.0004$	$0.0073 \pm 0.0003$	$0.54 \pm 0.06$	$0.25 \pm 0.04$
MACS J1423.8	0.545	total	$0.027 \pm 0.002$	$0.0044 \pm 0.0002$	...	...	$1.22 \pm 0.06$	$0.86 \pm 0.13$
		lobes	$27.3 \pm 1.4$	$5.3 \pm 0.3$	$0.39 \pm 0.04$	...	$1.092 \pm 0.046$	$1.80 \pm 0.13$
A2052	0.035	core	$3.63 \pm 0.15$	$0.44 \pm 0.02$	$0.33 \pm 0.13$	$0.264 \pm 0.012$	$1.4 \pm 0.04$	$0.33 \pm 0.03$
		lobes	$4.71 \pm 0.18$	$0.08 \pm 0.04$	...	...	$2.71 \pm 0.04$	$18 \pm 3$
MKW 3S	0.045	core	$0.021 \pm 0.002$	$0.0066 \pm 0.0003$	$0.0025 \pm 0.0001$	$0.0021 \pm 0.0001$	$0.77 \pm 0.05$	$0.0024 \pm 0.0003$

Table 2.3 (continued)

Name	$z$	Component	$S_{327}$ (Jy)	$S_{1400}$ (Jy)	$S_{4500}$ (Jy)	$S_{8500}$ (Jy)	$\alpha^a$	$L_{\text{radio}}^b$ ( $10^{42}$ erg s $^{-1}$ )
A2199	0.030	lobes	24 ± 1	1.64 ± 0.07	0.16 ± 0.02	0.07 ± 0.01	1.31 ± 0.04	1.34 ± 0.12
		core	0.40 ± 0.02	0.184 ± 0.007	0.153 ± 0.006	0.088 ± 0.004	0.39 ± 0.04	0.034 ± 0.004
		lobes	3680 ± 195	1220 ± 68	370 ± 23	123 ± 10	0.72 ± 0.05	710 ± 70
Cygnus A	0.056	core	2.86 ± 0.12 <sup>c</sup>	1.76 ± 0.09 <sup>c</sup>	1.23 ± 0.07	1.45 ± 0.06	0.32 ± 0.04	1.02 ± 0.12
		hot spots	697.22 ± 30.4 <sup>c</sup>	235.02 ± 9.4	104.93 ± 4.2	57.5 ± 2.3	0.7 ± 0.03	1.40 ± 10
		lobes	1.20 ± 0.08	0.18 ± 0.01	0.049 ± 0.003	0.021 ± 0.001	1.28 ± 0.06	0.26 ± 0.03
Sersic 159/03	0.058	core	0.323 ± 0.014	0.038 ± 0.002 <sup>d</sup>	0.0065 ± 0.0003 <sup>d</sup>	0.0029 ± 0.0001	1.44 ± 0.04	0.09 ± 0.01
		lobes	6.3 ± 0.4	1.53 ± 0.09	0.31 ± 0.08	0.082 ± 0.006	0.98 ± 0.06	2.56 ± 0.17
		core	2.05 ± 0.08	0.34 ± 0.01 <sup>c</sup>	0.069 ± 0.004	0.036 ± 0.001	1.25 ± 0.04	0.97 ± 0.08
A2597	0.085	lobes	9.0 ± 0.4	0.83 ± 0.04	0.063 ± 0.003	0.016 ± 0.001	1.61 ± 0.04	2.2 ± 0.3
		core	0.94 ± 0.04	0.0366 ± 0.0015	0.0081 ± 0.0003	0.0035 ± 0.0001	2.19 ± 0.04	0.95 ± 0.14
A4059	0.048	lobes						
		core						

<sup>a</sup>The spectral index was calculated between 327 MHz and 1400 MHz with the exception of Hydra A, calculated between 74 MHz and 327 MHz; Zw 2701 and Zw 3146, calculated between 4500 MHz and 8500 MHz; and Perseus and M87, calculated between 408 MHz (literature data, which are listed in Table 4.3) and 1.4 GHz with  $\nu_0 = 408$  MHz.

<sup>b</sup>The total radio luminosity between 10 MHz and 10000 MHz, for M87, A2199, and A4059 we used literature data at 1.4 GHz in order to estimate the spectral index.

<sup>c</sup>The fluxes were extrapolated using the spectral index between 10 MHz and 10000 MHz.

<sup>d</sup>The fluxes were extrapolated using the spectral index between the 327 MHz and 8500 MHz.

Note. — When we have multiple final images of different resolutions (see Table A.2), the lower resolution image was used to measure the flux, with the exceptions of A133 and Hydra A. In some cases we used literature fluxes in order to calculate spectral indices and total radio luminosities. These cases are Hydra A (408 MHz), M87 (408 MHz and 1400 MHz), A2199 (1400 MHz), and A4059 (1400 MHz); references are given in Table 4.3. Hydra A: 74 MHz and 327 MHz radio maps are from Lane et al. (2004);  $S_{74}^{\text{core}} = 0.033 \pm 0.04$  Jy;  $S_{74}^{\text{innerlobes}} = 220 \pm 10$  Jy. A2597: 327 MHz radio map is from Clarke et al. (2005).

For each source we measured the total flux density using TVSTAT in AIPS. In order to measure the flux density for the core of the radio sources, we used JMFIT in AIPS to fit a gaussian fixed to the beam shape. The flux in the lobes (including any jet emission) was calculated by subtracting the core flux density from the total flux density. In Table 2.3 we list the measured flux densities at 327 MHz, 1.4 GHz, 4.5 GHz, and 8.5 GHz for all the objects in our sample for the core and lobes. The errors in the flux densities include multiplicative errors plus RMS noise in the radio map (additive errors). In Carilli et al. (1991) the multiplicative errors in the flux densities range between 2% at 4.995 GHz and 6% at 327 MHz. For simplicity, we chose an average of 4% for the multiplicative errors at all frequencies. This value is consistent with the multiplicative error that Slee et al. (2001) used for the 1.425 GHz flux density (4.5% to 5.0%). In some cases, because the radio images were barely resolved (see Section 2.2.2 for more details) we couldn't separate the core and lobe fluxes. In these cases the core fluxes were extrapolated using the spectral index between two trusted core fluxes at different frequencies. We used the same procedure in order to infer the hot spot fluxes for Cygnus A at 327 MHz (see the notes for Table 2.3 for details of the extrapolation procedure). In the case of MACS J1423.8+2404, we could not separate the lobe and core contributions because of the lack of higher frequency data (we observed this object at 8.5 GHz, but the data were corrupted by interference). Lastly, for Zw 3146, we see only core emission at all frequencies at which we observed it.

## 2.2.2 Radio Morphologies

Figures B.1–B.16 show the radio contour maps for all the systems listed in Table A.2. Where there are 2 images for the same frequency we list the arrays that were used for each image. In some systems, we do not see extended emission at any of the 3 or 4 frequencies that were observed (e.g., Zw 3146). In general, the lack of extended radio emission is seen at higher frequencies (4.5 GHz and 8.5 GHz) where for some of the systems we imaged only the core (see Table 2.3 where we list the core and lobe contributions for all the systems). The lack of extended radio emission at a given frequency could either be due to the observed frequency being above the break frequency or to missing short spacings in the u-v plane (the latter can be important in particular for the larger sources). However, for some of the systems we imaged only the inner lobes at higher frequencies (e.g., Hydra A). On the other hand, the majority of the lower frequency observations (327 MHz and 1.4 GHz) show extended emission; the exceptions are HCG 62 at 327 MHz and Hydra A - outer lobes at 1.4 GHz, both of which likely have break frequencies below these frequencies. Some systems are barely resolved, especially among the lower frequency observations (e. g., A478 at 327 MHz).

By examining the radio morphology at different frequencies, we find that two of the systems in our sample have jets or lobes oriented differently at higher frequencies (4.5 GHz and 8.5 GHz) than at lower frequencies (327 MHz and 1.4 GHz). Systems with this morphology are Abell 2597 (Pollack et al., 2005; Clarke et al., 2005) and

RBS 797 ([Gitti et al., 2006](#)). However, because our data were obtained to image extended lobe emission, they are usually of insufficient resolution to resolve the jets in the sample as a whole. Additionally, [Dunn et al. \(2006\)](#) demonstrated that different generations of X-ray cavities in the same cluster are not always observed at the same position angle with respect of cluster core. This morphology can be explained by either a deflected jet ([Pollack et al., 2005](#)), by jet precession ([Dunn et al., 2006](#)), or by both ([Gitti et al., 2006](#)). As an example, the 'S' shape jets in Abell 1795 were explained by [Rodríguez-Martínez et al. \(2006\)](#), using hydrodynamical calculations, as a point-symmetric precessing jet interacting with a plane-parallel wind.

A persistent problem with cavity heating in simulations is the distribution of energy, as an unchanging jet orientation will tend to heat the ICM non-isotropically, forming low-density channels that carry the jet's energy out of the cooling region [see [Vernaleo & Reynolds \(2006\)](#), but c.f. [Heinz et al. \(2006\)](#)]. However, if such differently oriented jets are common, the cavity energy might naturally be spread isotropically throughout the atmosphere of a cluster (for a review, see [McNamara & Nulsen, 2007](#)).

### 2.2.3 Total Radio Luminosity

The total radio luminosity can be calculated by integrating the spectrum between  $\nu_1$  and  $\nu_2$ , using the luminosity distance to the source,  $D_L$  ([Pacholczyk, 1970](#)):

$$L_{\text{rad}} = 4\pi D_\nu^2 \int_{\nu_1}^{\nu_2} S(\nu) d\nu, \quad (2.1)$$

where  $S(\nu) \propto \nu^{-\alpha}$  and  $D_\nu = D_L(1+z)^{-\frac{1-\alpha}{2}}$  (Verschuur & Kellermann, 1974). Therefore:

$$L_{\text{rad}} = 4\pi D_L^2 S_{\nu_0} (1+z)^{\alpha-1} \int_{\nu_1}^{\nu_2} (\nu/\nu_0)^{-\alpha} d\nu. \quad (2.2)$$

For the initial 18-system sample, we used  $\nu_1 = 10$  MHz,  $\nu_2 = 5000$  MHz, and used for  $S_{\nu_0}$  the 1400 MHz flux from the NRAO VLA Sky Survey (NVSS) catalog (Condon et al., 1998), except in the case of the Centaurus cluster where no NVSS data were available. In this case, we used the 1410 MHz flux from the Parkes Radio Sources Catalogue (Wright & Otrupcek, 1990). Spectral indices were taken from the catalogs referenced in Table 2.1. As the derived spectral index can vary depending on the frequencies used, we have adopted a weighted average of the available spectral indices. In cases in which the spectral index was not available, a value of  $\alpha = 1$  was adopted.

For the expanded 24-system sample, we used  $\nu_1 = 10$  MHz,  $\nu_2 = 10000$  MHz, and  $\nu_0 = 327$  MHz. For most of the systems, the spectral index is calculated between 327 MHz and 1400 MHz. The exceptions are Hydra A, where the spectral index is calculated between 74 MHz and 327 MHz and  $\nu_0 = 74$  MHz, Zw 2701 and Zw 3146 where the spectral indices are calculated between 4.5 GHz and 8.5 GHz, and Perseus and M87 where the spectral indices are calculated between 408 MHz (taken from the literature, see Table 4.3) and 1.4 GHz, with  $\nu_0 = 408$  MHz. Because of poor u-v coverage, for some of the systems our 1.4 GHz radio fluxes were lower than ones in the literature. In these cases, we used the fluxes from the literature in order to

estimate the spectral index (e.g., M87, A2199 and A4059). Since we imaged only the core of Zw 3146 at all the frequencies that we observed it, we list in Table 2.3 only the core properties (fluxes, spectral index, and radio luminosity). On the other hand, for MACS J1423.2404 we could not separate the lobe contribution from the core contribution (see Section 2.2.1), and in Table 2.3 we list only the total source radio properties.

# CHAPTER 3

## Theory

### 3.1 X-Ray Cavity Energies and Ages

The total energy required to create an X-ray cavity can be estimated as the work done by the jets against the ICM plus the internal energy ([Birzan et al., 2004; Rafferty et al., 2006](#)):

$$E_{\text{cav}} = pV + \frac{1}{\gamma - 1}pV, \quad (3.1)$$

where  $p$  is the gas pressure,  $V$  is the cavity volume, and  $\gamma$ , the ratio of the gas specific heats, is assumed to be 4/3 (i.e., relativistic gas).

The age of each cavity was estimated in three ways. First, as the time required for the cavity to rise the projected distance from the radio core to its present location at the speed of sound,  $v_{\text{cs}} = (\gamma kT / \mu m_{\text{H}})^{1/2}$ , where we have taken  $\gamma = 5/3$  and  $\mu = 0.62$ . The cavity age is then

$$t_{\text{cs}} = R/v_{\text{cs}} = R\sqrt{\mu m_{\text{H}}/\gamma kT}, \quad (3.2)$$

where  $R$  is the projected distance from the center of the bubble to the radio core. This scenario is favored in the computational modeling of [Omma et al. \(2004\)](#), in which the bubble is produced by a high-momentum jet from the AGN instead of rising buoyantly. However, since strong shocks are not generally seen in these systems, this age is likely a lower limit. Second, the age was calculated as the time required for the

cavity to rise buoyantly (bubble-like) at its terminal velocity  $v_t \sim (2gV/SC)^{1/2}$ , where  $V$  is the volume of the bubble,  $S$  is the cross section of the bubble, and  $C = 0.75$  is the drag coefficient (Churazov et al., 2001). The gravitational acceleration was calculated using the stellar velocity dispersion of the central galaxy, under the approximation that the galaxy is an isothermal sphere, as  $g \approx 2\sigma^2/R$  (Binney & Tremaine, 1987). Published values of the velocity dispersion were used when available (see Table 2.1); otherwise, the average value ( $\langle\sigma\rangle = 280$  km s $^{-1}$ ) was adopted. The cavity age is then given by

$$t_{\text{buoy}} = R/v_t \sim R\sqrt{SC/2gV}. \quad (3.3)$$

Finally, the age was calculated as the time required to refill the displaced volume as the bubble rises upward (McNamara et al., 2000; Nulsen et al., 2002):

$$t_r \sim 2R\sqrt{r/GM(R)} = 2\sqrt{r/g}, \quad (3.4)$$

where  $r$  is the radius of the cavity [for ellipsoidal cavities,  $r = (ab)^{1/2}$ ].

## 3.2 Basic Formulas of Synchrotron Radiation

### 3.2.1 Spectrum of Synchrotron Radiation and Total Emitted Power

Synchrotron radiation is produced by relativistic electrons spiraling around magnetic field lines. The motion of an electron of mass  $m_e$  and energy  $E = \gamma m_e c^2$ , where

$\gamma$  is the Lorentz factor, in a magnetic field  $B$  is a helical one (a combination of a circular motion and a uniform motion along the field lines) with a frequency of rotation (gyration)  $\omega_B = eB(\gamma m_e c)^{-1}$ . An important feature of synchrotron radiation is that the observer will see the radiation confined in a time interval much smaller than the gyration period and confined to a cone of emission of half-angle  $\sim 1/\gamma$ , resulting in a beaming effect. As a result, from the observer's point of view, the radiation is a continuum with a very peaked spectrum at the critical frequency (for a detailed description of synchrotron radiation, see [Rybicki & Lightman, 1979](#)):

$$\nu_C = \frac{3}{4\pi} \gamma^3 \omega_B \sin \theta = \frac{3}{4\pi} \frac{e}{m_e^3 c^5} B \sin \theta E^2 = c_1 B \sin \theta E^2, \quad (3.5)$$

where  $\theta$  is the pitch angle between the magnetic field lines and the electron velocity. In order to express the above relation in c.g.s. units, the constant  $c_1 = 6.27 \times 10^{18}$  ([Pacholczyk, 1970](#)).

The rate of energy loss for the particles due to synchrotron radiation is:

$$\left. \frac{-dE}{dt} \right|_S = \frac{2e^4}{3m_e^4 c^7} (B \sin \theta)^2 E^2 = c_2 (B \sin \theta)^2 E^2, \quad (3.6)$$

where  $c_2 = 2.37 \times 10^{-3}$ , again in order to express the above relation in c.g.s. units.

Another important feature of synchrotron radiation is the fact that the synchrotron spectrum can be approximated by a power law over a limited range of frequencies:  $S(\nu) \propto \nu^{-\alpha}$ , where  $\alpha$  is the spectral index. For a power-law distribution of electrons with  $N(E) \propto N^{-p}$ , where  $p$  is the particle distribution index, the total power radiated per unit volume per unit frequency by such a distribution is

$S(\nu) \propto \nu^{-\frac{p-1}{2}}$ . Consequently, the spectral index and the particle distribution index are related by  $\alpha = (p - 1)/2$ .

### 3.2.2 Spectral Modeling and Ages

Kardashev (1962) studied the synchrotron spectrum of an ensemble of electrons evolving with time in the presence of a magnetic field (see Pacholczyk, 1970) and showed that the electron spectrum steepens at high frequencies. This steepening is dependent on the pitch angle and energy of the relativistic electrons. There are three main models based on this theory for characterizing the synchrotron spectrum: the KP (Kardashev-Pacholczyk) model, which includes a single injection of electrons and assumes a constant pitch angle with time; the JP (Jaffe-Perola) model, which includes a single energy injection of electrons and a continuous isotropization of the pitch angle with time; and the CI (continuous injection) model, which assumes a mixed population of electrons of different ages (see Myers & Spangler, 1985; Carilli et al., 1991; Feretti et al., 1998; Mack et al., 1998).

In order to study the spectrum of an ensemble of electrons, all of these models take into account not only the synchrotron losses described in the previous section, but also the inverse Compton losses due to scattering off of the Cosmic Microwave Background (CMB) photons. The rate of energy loss of a single electron due to inverse Compton losses is (Pacholczyk, 1970):

$$-\frac{dE}{dt} \Big|_{\text{C}} = \frac{32}{9} \frac{\pi c e^4}{(m_e c^2)^4} u_{\text{rad}} E^2 = \frac{2}{3} c_2 B_{\text{CMB}}^2 E^2, \quad (3.7)$$

where  $u_{\text{rad}} = B_{\text{CMB}}^2/(8\pi)$  is the energy density of the photon field and  $B_{\text{CMB}} = 3.25[1+z]^2\mu\text{G}$  is the magnetic field strength with an energy density equal to that of the CMB. Then, by taking into account both synchrotron losses and inverse Compton losses, the electron's rate of energy loss is given by:

$$-\frac{dE}{dt} = c_2 B^2 \left( \sin^2 \theta + \frac{2}{3} \frac{B_{\text{CMB}}}{B^2} \right) E^2. \quad (3.8)$$

The above relation is valid for the KP model which assumes that the pitch angle distribution is anisotropic. In the case of a isotropic pitch angle distribution (JP model)  $\sin^2 \theta$  will be replaced by  $\langle \sin^2 \theta \rangle = 2/3$ . Then, for the JP model model the above relation becomes:

$$-\frac{dE}{dt} = c_2 B^2 \left( \frac{2}{3} + \frac{2}{3} \frac{B_{\text{CMB}}}{B^2} \right) E^2. \quad (3.9)$$

The inverse Compton term is identical in both the KP and JP models because of the isotropy of the CMB radiation field. By integrating the expression for the electron's rate of energy loss, the evolution of the particle energy with time, for the KP model and JP model respectively, is given by:

$$E_{\text{KP}}(t) = \frac{E_0}{1 + c_2(B^2 \sin^2 \theta + \frac{2}{3} B_{\text{CMB}}^2) E_0 t} \quad (3.10)$$

$$E_{\text{JP}}(t) = \frac{E_0}{1 + c_2(\frac{2}{3} B^2 + \frac{2}{3} B_{\text{CMB}}^2) E_0 t}. \quad (3.11)$$

Then, the time required for the electron to lose half of its initial energy,  $E_0$ , is:

$$t_{\text{KP}} = \left( c_2 B^2 \sin^2 \theta + \frac{2}{3} c_2 B_{\text{CMB}}^2 \right)^{-1} E_0^{-1} \quad (3.12)$$

$$t_{\text{JP}} = \left( c_2 \frac{2}{3} B^2 + \frac{2}{3} c_2 B_{\text{CMB}}^2 \right)^{-1} E_0^{-1}. \quad (3.13)$$

This time is interpreted as the electron lifetime. Then, by substitution of Equation 3.5 into Equation 3.12, taking into account the source redshift  $z$ , the above relations become (for a derivation of the electron lifetime, see Feretti & Giovannini, 2007; Slee et al., 2001; van der Laan & Perola, 1969):

$$t_{\text{KP}} = 1060 \frac{B^{1/2}}{B^2 + \frac{2}{3} B_{\text{CMB}}^2} [(1+z)\nu_{\text{C}}]^{-1/2} \quad (3.14)$$

$$t_{\text{JP}} = 1590 \frac{B^{1/2}}{B^2 + B_{\text{CMB}}^2} [(1+z)\nu_{\text{C}}]^{-1/2}, \quad (3.15)$$

where  $\nu_{\text{C}}$  is the critical frequency in the spectrum below which the spectrum remains unchanged ( $\alpha = \alpha_{\text{inj}}$ , where  $\alpha_{\text{inj}}$  is the initial injection index) and above which the spectrum steepens ( $\alpha = \alpha_{\text{inj}} + 0.5$ ). This steepening is produced by radiative cooling, and it is valid for both KP and JP models. In the case of the KP model, the spectrum steepens again, due to inverse Compton losses of small pitch angle electrons, to a new power law:  $\alpha = 4/3\alpha_{\text{inj}} + 1$  (Komissarov & Gubanov, 1994).

### 3.3 Energy Content and Equipartition Magnetic Fields

The total energy within a radio source is the sum of the energy in relativistic electrons ( $E_e$ ), the energy in the heavy particles ( $E_p$ ), and the energy in the magnetic

field ( $E_B$ ):

$$E_{\text{tot}} = E_e + E_p + E_B. \quad (3.16)$$

The total energy of the electrons is defined as:

$$E_e = \int_{E_1}^{E_2} EN(E)dE = N_0 \int_{E_1}^{E_2} E^{-p+1}dE, \quad (3.17)$$

where  $N_0$  can be replaced by the total radio luminosity  $L_{\text{rad}} = \int_{E_1}^{E_2} (dE/dt)N(E)dE$ , with the rate of loss of particles due to synchrotron radiation ( $-dE/dt$ ) defined in Section 3.2.1. Because most of the electrons radiate their energy at frequencies around the critical frequency, we can replace the cutoff energies  $E_1$  and  $E_2$  with the corresponding critical frequencies  $\nu_1$  and  $\nu_2$  defined in Section 3.2.1. Therefore, the total energy of the electrons can be expressed as:

$$E_e = (B \sin \theta)^{-3/2} L_{\text{rad}} c_{12}(\alpha, \nu_1, \nu_2), \quad (3.18)$$

where  $c_{12}(\alpha, \nu_1, \nu_2)$  is a constant as defined by Pacholczyk (1970).

The energy in the heavy particles can be estimated as  $E_p = kE_e$ , where  $k$  can vary between 1, for lepton jets, and 2000, if induction-type acceleration processes are generating the relativistic particles (Pacholczyk, 1970).

The energy in the magnetic field is calculated as:

$$E_B = \frac{B^2}{8\pi} \phi V, \quad (3.19)$$

where  $\phi$  is the filling factor, the fraction of the volume filled by relativistic particles that is filled also with magnetic fields, and  $V$  is the source volume. Then, for  $\sin \theta = 1$ ,

the total energy becomes:

$$E_{tot} = (1 + k)B^{-3/2}L_{rad}c_{12}(\alpha, \nu_1, \nu_2) + \frac{B^2}{8\pi}\phi V. \quad (3.20)$$

One can estimate the magnetic field by assuming the minimum-energy condition (see [Pacholczyk, 1970](#)). The total energy is minimal when the magnetic field energy is approximately equal to the energy in the particles (this minimum magnetic energy is known as the equipartition value):

$$E_{B_{eq}} = \frac{3}{4}(1 + k)E_e. \quad (3.21)$$

Under the minimum-energy assumption the magnetic field strength is :  $B_{eq} = B_{ct}[(1 + k)/\phi]^{2/7}$ , where

$$B_{ct} = (6\pi)^{2/7}c_{12}^{2/7}(\alpha, \nu_1, \nu_2)L_{rad}^{2/7}V^{-2/7} \text{ G}. \quad (3.22)$$

### 3.4 Particle Content ( $k$ )

In order to calculate the ratio between the heavy-particle energy and the electron energy ( $k$ ), we assume pressure equilibrium between the interior particles of the lobe and the magnetic fields ( $P_P + P_B$ ), and the surrounding thermal gas ( $P_{th}$ ). The cavities are assumed to be in near pressure equilibrium because they are observed to be long lived ( $\sim 10^8$  yr) and surrounded by cool rims that are not expanding rapidly ([McNamara & Nulsen, 2007](#)). The pressure in the thermal gas is computed from X-ray observations (see Section [2.1.1](#)). The pressure in the particles and magnetic

fields is given by:

$$P_P + P_B = \frac{(1+k)E_e}{3V\phi} + \frac{E_B}{V\phi}. \quad (3.23)$$

Then, by requiring  $P_{\text{th}} = P_P + P_B$ , we can compute the magnetic field required for pressure equilibrium ( $B_p$ ).

Next, we computed the particle content  $k$  in two ways. The first estimate was computed by requiring that the equipartition magnetic field ( $B_{\text{eq}}$ ) to be equal to the magnetic field required for pressure equilibrium ( $B_p$ ):

$$\left. \frac{1+k}{\phi} \right|_{\text{eq}} = P_{\text{th}}^{7/4} \left[ \frac{B_{\text{ct}}^{-3/2} L_{\text{rad}} c_{12}(\alpha, \nu_1, \nu_2)}{3V} + \frac{B_{\text{ct}}^2}{8\pi} \right]^{-7/4}. \quad (3.24)$$

The second estimate of the particle content was obtained by using the cavity ages calculated from X-ray observations and by equating the synchrotron age to the buoyancy age ( $B_{\text{buoy}}$ ). Then, by requiring  $B_{\text{buoy}} = B_p$ , we obtain:

$$\left. \frac{1+k}{\phi} \right|_{\text{buoy}} = \left[ P_{\text{th}} - \frac{B_{\text{buoy}}^2}{8\pi} \right] \frac{3V}{B_{\text{buoy}}^{-3/2} L_{\text{rad}} c_{12}}. \quad (3.25)$$

# CHAPTER 4

## Results

### 4.1 Cavity Classification

In the literature, X-ray cavities have been divided into two categories depending on the presence of bright 1400 MHz radio emission in the cavities: radio-filled and radio-ghost cavities. Radio-filled cavities, such as the inner cavities in Hydra A ([McNamara et al., 2000](#)), have 1400 MHz or higher frequency emission. Ghost cavities, such as those in A2597 ([McNamara et al., 2001](#)), lack significant emission at 1400 MHz. The ghost cavities were interpreted to be detached relics of earlier outbursts whose radio emission has faded ([McNamara et al., 2001](#)). However, this classification depends critically on the quality of the available radio images and is largely a qualitative one. In this section we give a quantitative classification system based on the break frequency of the synchrotron emission.

For the initial 18-system sample ([Bîrzan et al., 2004](#)), we used the traditional, qualitative classification system. The cavities were classified as either radio-filled or radio-ghost, depending on the presence of 1400 MHz or higher frequency radio emission inside the cavity (see Table 2.2). Lacking data of our own, we used literature radio data in order to classify the cavities. The cavities were classified as radio-filled if there was a direct anticorrelation between the radio emission at 1400 MHz or

higher and the X-ray emission, such that the radio emission fills preferentially the X-ray surface brightness depressions. The cavities classified as ghost cavities, while possibly possessing significant radio emission at frequencies at or below 1400 MHz, did not show the anti-correlation between the high-frequency radio emission and the X-ray emission. As stated above, this classification scheme relies heavily on the availability of high-resolution radio images at several frequencies. However, the available literature radio data are inhomogeneous, and classifying the objects lacking high-resolution radio images was challenging. The poor radio images available for A262, RBS 797, and HCG 62, in particular, led us to classify them as ghosts.

For the expanded, 24-system sample, we have homogeneous radio data at 4 different frequencies for most of the systems in our sample (see Figures B.1 – B.16). Therefore, we can now determine more precisely whether a cavity is radio filled or ghost. Figures B.17 – B.25 show the overlays of radio emission (in green) on the smoothed *Chandra* X-ray images. Since we are interested in the correlation between the X-ray cavities and the radio emission at different frequencies, we display only the cases where we have extended radio emission. These figures show that Hydra A (inner lobes), M84, M87, Centaurus, A2052, A2199, and Cygnus A have X-ray cavities filled with 1.4 GHz and higher frequency radio emission (4.5 GHz and/or 8.5 GHz) and would be classified as radio-filled cavities based on the above classification. On the other hand, A133, A478, and MS 0735.6+7421 were classified as radio-filled cavities

based on the fact that 1.4 GHz fills the cavities; however, our new data do not show any higher frequency emission filling the cavities in these systems.

Since all the cavities have some radio emission when probed deeply, the traditional distinction between radio-ghost and radio-filled cavities is somewhat arbitrary. In order to be more quantitative, we propose that the break frequency be used to separate cavities between radio-filled, radio-ghost, and intermediate cases. The traditional classification is essentially equivalent to saying that a radio-filled cavity is one that has a break frequency higher than 1.4 GHz, since the break frequency defines the point above which the spectrum falls steeply. With this idea in mind, we classify systems with lobe break frequencies below  $\sim 1.4$  GHz as ghost cavity systems, those with frequencies between  $\sim 1.4$  GHz and  $\sim 5.0$  GHz as intermediate cases, and those with break frequencies above 5.0 GHz as radio-filled systems (see Table 4.1). However, note that some systems are classified as ghost because of the lack of a break frequency estimate (e.g., Zw 2701, Zw 3146, HCG 62, and MACS J1423.8+2404).

We note that 1.4 GHz and 5.0 GHz are arbitrary points for separating the systems between radio-filled, intermediate, and ghost, since Table 4.3 shows a continuous range of break frequencies. Furthermore, this continuous range in break frequencies can be interpreted as a continuous range in ages, if the magnetic field strengths are similar (Carilli & Taylor, 2002). Assuming a typical B field between 5 and 10  $\mu$ G, the 1400 MHz break frequency corresponds to an age of roughly between  $3 - 7 \times 10^7$  yr. Since radio sources typically have a lifetime of  $\sim 10^7$  yr, most of the ghost cavities under our

classification have ages significantly older than the lifetime of a typical radio source. The ages of ghost cavities are therefore consistent with the interpretation that they are relics of previous outbursts.

However, the situation has become complicated with the discovery of tunnels of X-ray emission filled with low frequency radio emission ([Clarke et al., 2001](#); [Wise et al., 2007](#)). Additionally, some of the ghost systems show inner jets or lobes at higher frequencies (Hydra A - outer lobes, RBS 797, Sersic 159/03, A2597, and A4059). These radio sources can be either restarting or fading away. For RBS 797, based on the discovery that the inner jets seen at higher frequencies have a different orientation than the outer lobes seen at lower frequencies, the interpretation is that this radio source has probably restarted (see also [Gitti et al., 2006](#)). However, for A4059 the inner jets have the same orientation as the outer ones; therefore, this radio source may be in an intermediate stage where the radio emission from the lobes is fading away (as suggested by [Heinz et al., 2002](#)). Also, A2597 is interpreted by [Clarke et al. \(2005\)](#) as an intermediate case based on the finding of an X-ray tunnel which connects the west ghost bubble to the core of the source. The outer lobes in Hydra A are in a similar situation([Wise et al., 2007](#)). For Sersic 159/03, the 10 ks X-ray observation was not deep enough to image the cavities well. The 327 MHz radio map shows extended emission, but oriented differently than the X-ray cavities identified in [Rafferty et al. \(2006\)](#). Much deeper X-ray observations are required in order to

clarify this discrepancy. However, the radio source seems to be either restarted or fading away; as a result the X-ray cavities are classified as ghost.

## 4.2 Magnetic Field and Particle Content

Because the magnetic field and particles are intimately connected through the observed synchrotron radiation, we discuss them together in this section. Observational evidence for magnetic fields outside of the radio sources, but within the hot thermal gas in galaxy clusters, comes from Faraday rotation measurements of radio galaxies in and beyond clusters in combination with X-ray data (e.g., Dreher et al., 1987; Owen et al., 1990; Burns et al., 1992; Ge & Owen, 1993; Taylor & Perley, 1993; Ge & Owen, 1994; Taylor et al., 1994, 2002). These studies show that the central cooling flow regions have magnetic field strengths of  $5 \mu\text{G}$  to  $10 \mu\text{G}$  with a coherence scale between 5 and 10 kpc (Carilli & Taylor, 2002). Using a uniform sample of background and cluster-member sources, Clarke et al. (2001) found that galaxy clusters are magnetized to a level of  $5 \mu\text{G}$ . The current theory posits that AGN are responsible for the magnetization of the ICM, and they may also have an impact on large-scale structure and galaxy formation (Kronberg et al., 2001; Benson et al., 2003).

Because X-ray and radio data probe different properties of the lobes, they can be used together to increase our understanding of the lobes' content. Equation 3.20 governs the total energy content of the lobes, comprised of magnetic field and particle contributions. However, before the discovery of X-ray cavities, the total energy (the

left hand side of the equation) was essentially unknown. Now, the cavities provide an estimate of the total energy within factor of a few (see Section 4.5.2). The other factors in equation 3.20 are constrained either by X-ray or radio data, with the exceptions of  $k$  and  $B$ . By further assuming pressure balance (see equation 3.23) and equipartition (equation 3.21), we can constrain these two remaining parameters.

In Table 4.1 and Table 4.2 we list the lobes' equipartition magnetic field strengths for  $k = 1$  and  $\phi = 1$  ( $B_{\text{eq}}$ ,  $B_{\text{eq327}}$ ), the magnetic field strengths required for pressure equilibrium for  $k = 1$  and  $\phi = 1$  ( $B_p$ ), and the magnetic field strengths obtained assuming that the synchrotron age is equal to the buoyancy age ( $B_{\text{buoy}}$ ).

Table 4.1. Lobe properties derived using the cavity sizes from X-ray observations

Name	$B_{\text{eq}}^{\text{a}}$ ( $\mu\text{G}$ )	$B_p^{\text{b}}$ ( $\mu\text{G}$ )	$t_{\text{syn}}^{\text{eq,c}}$ ( $10^7$ yr)	$t_{\text{syn},\text{cor}}^{\text{eq,d}}$ ( $10^7$ yr)	$t_{\text{syn}}^p$ ( $10^7$ yr)	$B_{\text{buoy}}^{\text{f}}$ ( $\mu\text{G}$ )	$1 + k_{\text{eq,g}}$	$1 + k_{\text{buoy}}^{\text{g}}$	$B_{\text{eq},p}^{\text{h}}$ ( $\mu\text{G}$ )
A133	$19.4 \pm 0.4$	$53 \pm 1$	$2.0 \pm 0.7$	$1.5 \pm 0.1$	$0.46 \pm 0.03$	$13.5 \pm 0.2$	$37 \pm 2$	$19 \pm 2$	$45 \pm 1$
A262	$6.1 \pm 0.3$	$44 \pm 6$	$7.1 \pm 0.1$	$5.4 \pm 0.4$	$0.4 \pm 0.2$	$23.7 \pm 0.5$	$1100 \pm 500$	$1300 \pm 300$	$37 \pm 5$
Perseus	$16 \pm 2$	$130 \pm 2$	$> 1.9$	$> 1.3$	$> 0.1$	$32 \pm 2$	$1700 \pm 100$	$800 \pm 400$	$110 \pm 10$
2A 0335+096	$6 \pm 0.6$	$70 \pm 1$	$3.8 \pm 0.2$	$2.9 \pm 0.1$	$0.12 \pm 0.03$	$3.1 \pm 0.1$	$5800 \pm 100$	$500 \pm 200$	$58 \pm 6$
A478	$11 \pm 2$	$160 \pm 20$	$3.2 \pm 0.4$	$2.7 \pm 0.3$	$0.06 \pm 0.02$	$21.2 \pm 0.5$	$12000 \pm 5000$	$2600 \pm 2000$	$130 \pm 30$
MS 0735.6+7421	$11.8 \pm 0.3$	$42 \pm 3$	$4.1 \pm 0.3$	$2.1 \pm 0.1$	$0.7 \pm 0.2$	$4.5 \pm 0.2$	$90 \pm 30$	$13 \pm 2$	$35 \pm 3$
Hydra A - outer lobes <sup>i</sup>	$4.1 \pm 0.5$	$29$	$21 \pm 1$	$8.5 \pm 0.4$	$1.7$	$5$	$1000$	$300 \pm 100$	$24 \pm 3$
Hydra A - inner lobes	$70 \pm 10$	$59 \pm 2$	$< 0.06$	$< 0.04$	$< 0.09$	$4.6 \pm 0.4$	$1.70 \pm 0.17$	$\text{NS}^{\text{m}}$	$80 \pm 10$
RBS 797	$17 \pm 1$	$201 \pm 4$	$1.4 \pm 0.1$	$0.9 \pm 0.1$	$0.038 \pm 0.003$	$9.1 \pm 0.2$	$6000 \pm 500$	$250 \pm 70$	$170 \pm 10$
Zw 2701	$4.2 \pm 0.1$	$77 \pm 8$	$\dots$	$\dots$	$\dots$	$\dots$	$27000 \pm 9000$	$\dots$	$76 \pm 5$
Zw 3146 <sup>j</sup>	$\dots$	$\dots$	$\dots$	$\dots$	$\dots$	$\dots$	$\dots$	$\dots$	$\dots$
M84	$40 \pm 20$	$\text{NS}^{\text{m}}$	$< 0.13$	$< 0.07$	$\dots$	$25.6 \pm 0.5$	$\text{NS}^{\text{m}}$	$\text{NS}^{\text{m}}$	$38 \pm 2$
M87	$110 \pm 10$	$\text{NS}^{\text{m}}$	$0.05 \pm 0.02$	$0.04 \pm 0.01$	$< 0.11$	$34 \pm 1$	$\text{NS}^{\text{m}}$	$\text{NS}^{\text{m}}$	$100 \pm 10$
Centaurus	$40 \pm 10$	$65 \pm 3$	$< 0.14$	$< 0.11$	$< 0.08$	$13.5 \pm 0.8$	$5.7 \pm 0.9$	$2.1 \pm 1.9$	$60 \pm 20$
HCG 62	$2 \pm 1$	$24 \pm 2$	$\dots$	$\dots$	$\dots$	$8000 \pm 2000$	$\dots$	$\dots$	$20 \pm 3$
A1795 <sup>k</sup>	$\dots$	$\dots$	$\dots$	$\dots$	$\dots$	$\dots$	$\dots$	$\dots$	$\dots$
A1835	$9 \pm 1$	$171 \pm 7$	$3.6 \pm 0.2$	$3.4 \pm 0.2$	$0.05 \pm 0.01$	$12.3 \pm 0.3$	$35000 \pm 5000$	$2900 \pm 1600$	$140 \pm 20$
MACS J1423.8+2404 <sup>l</sup>	$\dots$	$\dots$	$\dots$	$\dots$	$\dots$	$\dots$	$\dots$	$\dots$	$\dots$
A2052	$19.2 \pm 0.7$	$94 \pm 1$	$0.90 \pm 0.02$	$0.77 \pm 0.01$	$0.15 \pm 0.01$	$18 \pm 1$	$70 \pm 5$	$40 \pm 10$	$53 \pm 2$
MKW 3S	$22.0 \pm 0.4$	$53 \pm 3$	$> 1.7$	$> 1.3$	$> 0.4$	$7.0 \pm 0.1$	$23 \pm 4$	$4.6 \pm 0.3$	$45 \pm 2$
A2199	$16.1 \pm 0.4$	$70 \pm 2$	$1.6 \pm 0.1$	$1.05 \pm 0.02$	$0.18 \pm 0.02$	$12.1 \pm 0.4$	$180 \pm 20$	$53 \pm 8$	$58 \pm 2$
Cygnus A	$69 \pm 6$	$42 \pm 2$	$0.105 \pm 0.004$	$0.055 \pm 0.001$	$0.22 \pm 0.02$	$5.0 \pm 0.2$	$1.8 \pm 0.1$	$\text{NS}^{\text{m}}$	$76 \pm 6$
Seric 159/03	$7.1 \pm 0.3$	$72 \pm 2$	$3.7 \pm 0.2$	$3.2 \pm 0.1$	$0.14 \pm 0.01$	$9.1 \pm 0.3$	$3400 \pm 400$	$700 \pm 100$	$60 \pm 3$
A2597	$15.3 \pm 0.9$	$90 \pm 3$	$1.19 \pm 0.32$	$1.11 \pm 0.02$	$0.08 \pm 0.01$	$6.5 \pm 0.7$	$600 \pm 100$	$40 \pm 20$	$70 \pm 10$
A4049	$21.2 \pm 0.6$	$46 \pm 3$	$1.13 \pm 0.04$	$0.94 \pm 0.03$	$0.36 \pm 0.07$	$12 \pm 3$	$17 \pm 4$	$9 \pm 7$	$40 \pm 3$

aThe equipartition magnetic field strength for  $k = 1$  and  $\phi = 1$ .

bThe magnetic field strength required for pressure equilibrium for  $k = 1$  and  $\phi = 1$ .

cThe synchrotron age computed using the equipartition magnetic field strength ( $B_{\text{eq}}$ ) and the break frequency  $\nu_C$ .

dThe synchrotron age computed using the equipartition magnetic field strength ( $B_p$ ) and the adiabatic-expansion-corrected break frequency,  $\nu_C^{\text{cor}}$ .

eThe synchrotron age computed using the magnetic field strength required for pressure equilibrium ( $B_p$ ) and the break frequency  $\nu_C$ .

fThe magnetic field strength obtained by assuming that the equipartition synchrotron age ( $t_{\text{syn}}^p$ ) is equal to the buoyancy age.

gAssumes  $\phi = 1$ .

hThe magnetic field strength that corresponds to the  $k_{\text{eq}}$  value for which the equipartition magnetic field equals the field required for pressure equilibrium.

iThe X-ray volume, buoyancy age, and sound speed age are from Wise et al. (2007).

jOnly the core was imaged at all frequencies at which we observed it (see Table 2.3).

kThe radio emission and the X-ray cavities are not correlated.

lBecause of the lack of radio data at 4.5 GHz or 8.5 GHz, we couldn't separate the lobe emission from the core emission.

mNo physical solution.

Furthermore, using the equipartition magnetic field strengths or the limiting values of the magnetic field described above and assuming pressure equilibrium, we compute the particle content ( $k$ ), assuming  $\phi = 1$  ( $k_{\text{eq}}$ ,  $k_{\text{eq}327}$ ,  $k_{\text{buoy}}$ ,  $k_{\text{buoy}327}$ ). Based on the X-ray observations of cavities and shocks, the filling factor must be close to 1, otherwise the cavities will not be evident in X-ray images, and the observed shocks require that the lobes displace most of the volume they occupy (see [McNamara & Nulsen, 2007](#)). The magnetic field strengths and  $k$  values listed in Tables [4.1](#) and [4.2](#) are computed using the volume from the X-ray observations and from the radio observations, respectively. Under certain assumptions, M87 and Cygnus A can have negative values of  $k$ . In these cases the outside thermal pressure is lower than the magnetic field pressure supporting the cavities, and the cavities are over-pressurized; therefore, pressure equilibrium under these assumptions is not possible.

Lastly, using the  $k_{\text{eq}}$  ( $k_{\text{eq}327}$ ) values, we calculated the corresponding magnetic field strengths  $B_{\text{eq},p}$  ( $B_{\text{eq},p327}$ ) using the volume inferred from the X-ray observations (see Table [4.1](#)) and from the radio observations (Table [4.2](#)). In general, the magnetic field strengths calculated with the volume from the radio observations are larger than the ones calculated with the volume from the X-ray observations, due to differences in volume (see Section [4.6](#)) . Also, the magnetic field strengths required for pressure equilibrium are much larger than the equipartition magnetic field strengths, and all of them in general are larger than the cluster-wide magnetic field estimates ([Carilli & Taylor, 2002](#)).

Table 4.2. Magnetic field, synchrotron age, and particle content using the lobe sizes from 327 MHz radio observations

Name	$B_{\text{eq}327}^{\text{a}}$ ( $\mu\text{G}$ )	$t_{\text{syn}327}^{\text{eq}}$ ( $10^7$ yr)	$1 + k_{\text{eq}327}^{\text{b}}$	$1 + k_{\text{bouy}327}^{\text{b}}$	$B_{\text{eq},p327}$ ( $\mu\text{G}$ )
A133	$18.4 \pm 0.4$	$2.1 \pm 0.1$	$90 \pm 30$	$33 \pm 2$	$60 \pm 10$
A262	$5.5 \pm 0.3$	$8.1 \pm 0.2$	$1800 \pm 900$	$2000 \pm 1000$	$40 \pm 10$
Perseus	$18 \pm 2$	$> 1.7$	$1700 \pm 1200$	$710 \pm 30$	$110 \pm 30$
2A 0335+096	$3.0 \pm 0.3$	$7.0 \pm 0.3$	$101000 \pm 3000$	$7600 \pm 200$	$130 \pm 10$
A478	$8 \pm 2$	$5.2 \pm 0.6$	$70000 \pm 20000$	$13000 \pm 5000$	$220 \pm 50$
MS 0735.6+7421	$9.8 \pm 0.2$	$5.2 \pm 0.4$	$200 \pm 60$	$27 \pm 7$	$60 \pm 10$
Hydra A - outer lobes	$4.1 \pm 0.5$	$21 \pm 1$	$20000$	$1700$	$60 \pm 10$
RBS 797	$3.0 \pm 0.2$	$5.9 \pm 0.3$	$500000 \pm 10000$	$42000 \pm 8000$	$600 \pm 50$
Zw 2701 <sup>c</sup>	...	...	...	...	...
Zw 3146 <sup>c</sup>	...	...	...	...	...
M84	$31 \pm 9$	$< 0.21$	NS <sup>d</sup>	NS <sup>d</sup>	$40 \pm 20$
M87	$24 \pm 7$	$0.49 \pm 0.02$	$24 \pm 2$	$30 \pm 7$	$220 \pm 20$
Centaurus	$13 \pm 3$	$< 0.8$	$195 \pm 7$	$90 \pm 10$	$160 \pm 40$
HCG 62 <sup>c</sup>	...	...	...	...	...
A1795 <sup>c</sup>	...	...	...	...	...
A1835 <sup>c</sup>	...	...	...	...	...
MACS J1423.8+2404 <sup>c</sup>	...	...	...	...	...
A2052	$11.6 \pm 0.5$	$1.85 \pm 0.04$	$250 \pm 30$	$180 \pm 10$	$76 \pm 4$
MKW 3S	$14.6 \pm 0.3$	$> 2.2$	$110 \pm 20$	$21 \pm 4$	$70 \pm 3$
A2199	$14.6 \pm 0.4$	$1.84 \pm 0.06$	$260 \pm 30$	$80 \pm 10$	$65 \pm 3$
Cygnus A	$66 \pm 5$	$0.111 \pm 0.004$	$4.10 \pm 0.16$	NS <sup>d</sup>	$90 \pm 10$
Sersic 159/03	$6.6 \pm 0.3$	$4.2 \pm 0.2$	$3900 \pm 500$	$800 \pm 100$	$62 \pm 3$
A2597	$8.3 \pm 0.5$	$2.7 \pm 0.1$	$5000 \pm 1000$	$390 \pm 50$	$140 \pm 10$
A4059	$9.9 \pm 0.3$	$3.3 \pm 0.1$	$340 \pm 50$	$150 \pm 30$	$93 \pm 5$

<sup>a</sup>Assumes  $k = 1$  and  $\phi = 1$ .

<sup>b</sup>Assumes  $\phi = 1$ .

<sup>c</sup>The 327 MHz radio emission was unresolved; only the core was imaged.

<sup>d</sup>No physical solution.

Our estimates of the ratio of heavy-particle energy to electron energy range from one to tens of thousands, using the volume from X-ray observations; they are much larger when we use the volume from the radio images (see Table 4.2). A similar range was seen by Dunn & Fabian (2004) and Dunn et al. (2005). However, for some systems our numbers are different by many orders of magnitude. Because  $k$

is inversely proportional to the total radio luminosity, the differences that we see between our  $k$  values and theirs can be due in part to differences in the total radio luminosity. [Dunn & Fabian \(2004\)](#) and [Dunn et al. \(2005\)](#) used the spectral indices from the literature and the 5 GHz radio flux in order to calculate the total radio luminosity. In this work we have better estimates of the total radio luminosity, since we obtained measurements of the lobe fluxes at multiple frequencies to derive the spectral index. Additionally, we used the 327 MHz flux to calculate the luminosity, which is not as sensitive as the 5 GHz flux to aging effects. Also, we note that for some systems the cavity sizes and positions used by [Dunn & Fabian \(2004\)](#) and [Dunn et al. \(2005\)](#) are different than the ones we used ([Birzan et al., 2004](#); [Rafferty et al., 2006](#)). These differences in sizes and positions will further affect the volume and buoyancy-age calculation, both important in the derivation of  $k$ .

From theoretical estimates  $k$  is predicted to range between 1 and 2000, depending on the mechanism that is generating the electrons ([Pacholczyk, 1970](#)). Using both X-ray and radio data we can place observational constraints on  $k$  by assuming pressure equilibrium and equipartition with both electrons and heavy particles (see equation 3.24) or by requiring the synchrotron age to be equal to the buoyancy age (see equation 3.25). The resulting large range in  $k$ , much larger than the theory predicts, may be due to differences in the magnetic field strength or to differences in intrinsic radio source properties such as the synchrotron age.

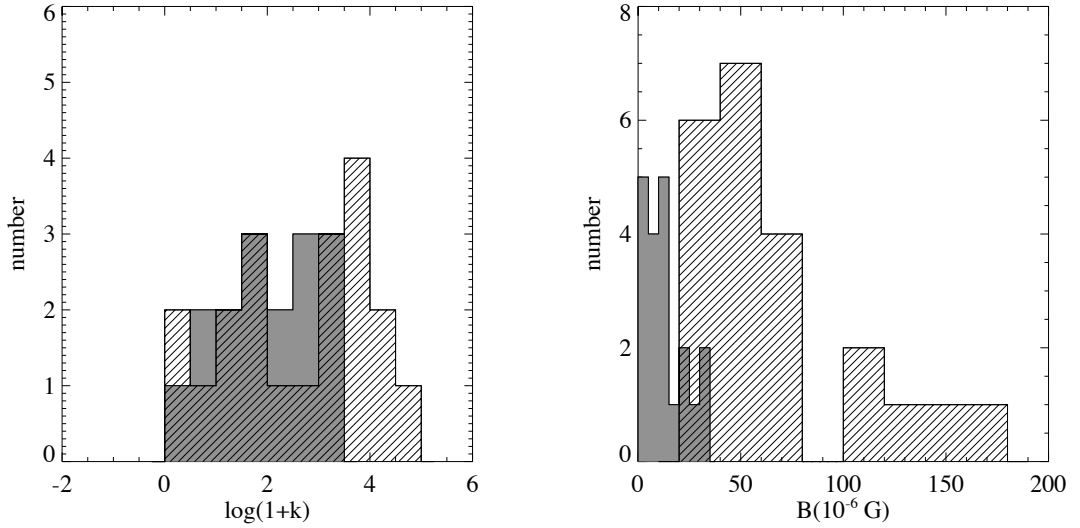


Figure 4.1: *Left:* Histogram of the ratio of heavy-particle energy to electron energy, calculated by assuming pressure equilibrium and equality between the synchrotron age and the buoyancy age ( $k_{\text{buoy}}$ , displayed in grey) and by requiring the equipartition magnetic field to be equal to the field required for pressure equilibrium ( $k_{\text{eq}}$ , shaded); *Right:* Histogram of the corresponding magnetic field strengths,  $B_{\text{buoy}}$  (grey) and  $B_{\text{eq,p}}$  (shaded).

In order to understand how the magnetic field strength affects the  $k$  values, we plot in the left panel of Figure 4.1 histograms of  $k$  ( $k_{\text{eq}}$  and  $k_{\text{buoy}}$ ), and in the right panel we plot the corresponding magnetic field strengths ( $B_{\text{eq,p}}$  and  $B_{\text{buoy}}$ ). We note that the two magnetic field strengths have different ranges, with that of  $B_{\text{buoy}}$  much smaller than that of  $B_{\text{eq,p}}$ .  $B_{\text{buoy}}$  is obtained by forcing the synchrotron age to be equal to the buoyancy age, but  $B_{\text{eq,p}}$  is the magnetic field strength corresponding to the  $k_{\text{eq}}$  for which the equipartition magnetic field equals the field required for pressure equilibrium. In both histograms, we required that the thermal gas be in pressure equilibrium with the particles and magnetic fields. In general, the smaller

$B_{\text{buoy}}$  values produce smaller  $k$  values. This result is due to the interplay between  $k$ ,  $B$ , and the observed radio luminosity, such that if  $B$  decreases, the energy in the electrons increases, thus  $k$  decreases. As a result,  $k$  has approximately the same range. However, both assumptions (equipartition and the age constraint) produce a large range in  $k$ .

The range in  $k$  may also be due to the range in intrinsic radio properties such as the synchrotron age. To investigate this possibility further, in Figure 4.2 we plot  $k_{\text{eq}}$  versus the break frequency. We notice a dichotomy between high and low break frequency systems, such that objects with high  $k$  have a low break frequency, as is expected if the low-break-frequency objects lost their high-energy electrons, increasing the ratio between heavy (total) particle energy and electron energy over time. However, we note that there is a range in break frequencies in our sample of a factor of  $\sim 100$ . This factor of 100 in break frequency translates into only a factor of  $\sim 100$  in  $1 + k$ , since synchrotron luminosity scales proportionally to the break frequency and  $k$  scales inversely with luminosity. Therefore, aging is unlikely to fully explain the range in  $k$  that we find. Lastly, the trend in Figure 4.2 and the large values of  $k$  may support the idea of a heavy jet (for a complementary view on this subject, see De Young, 2006) or entrainment of heavy particles (see e.g., Rossi et al., 2004). Also, we note that the objects with higher value of  $k$  do not have prominent jets in our images, but instead have more extended radio emission.

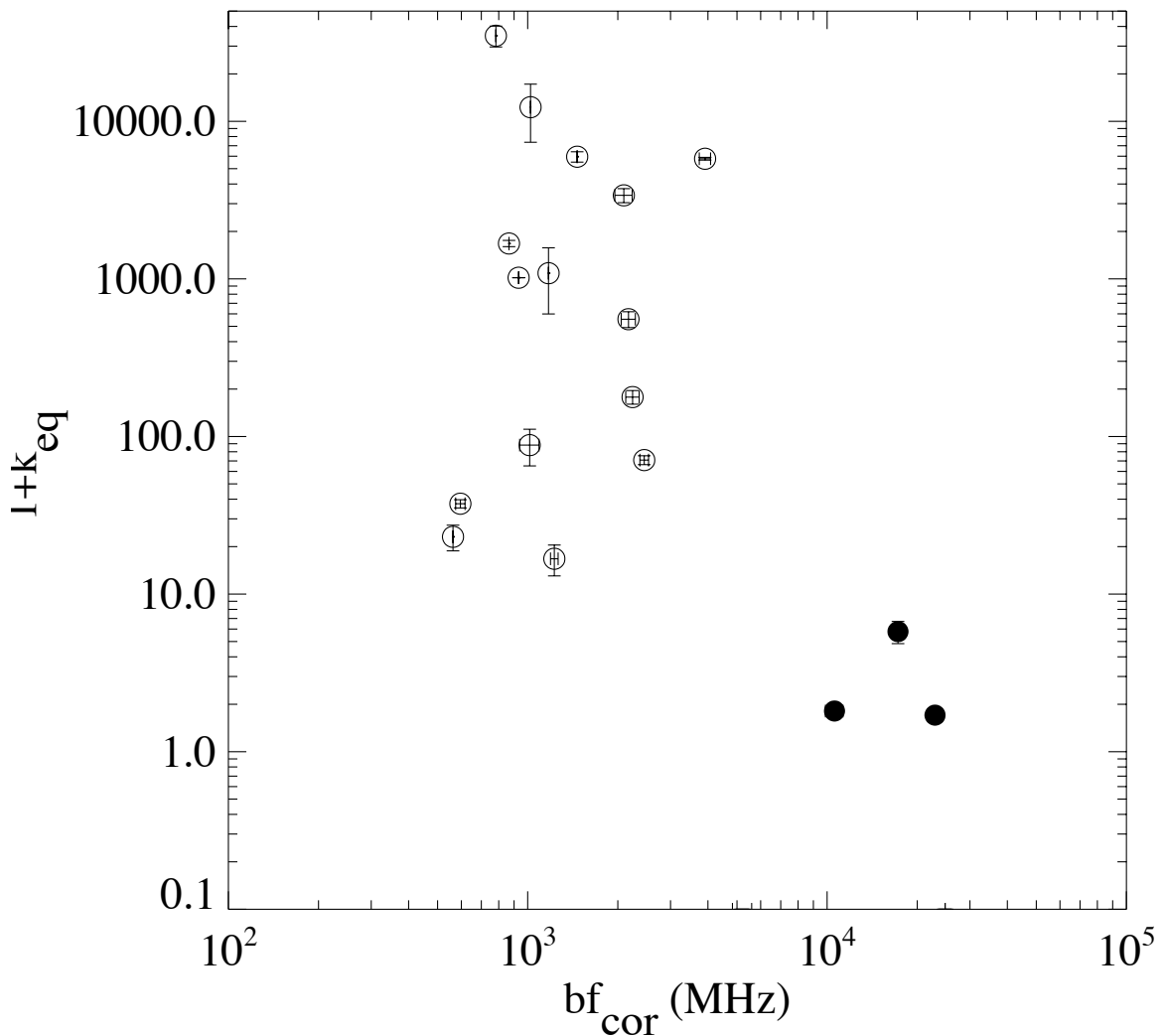


Figure 4.2: The ratio of heavy-particle energy to electron energy for which the equipartition magnetic field strength equals the field required for pressure equilibrium versus the adiabatically corrected break frequency. Filled symbols denote radio-filled cavities, and open symbols denote ghost cavities (which include the intermediate cases).

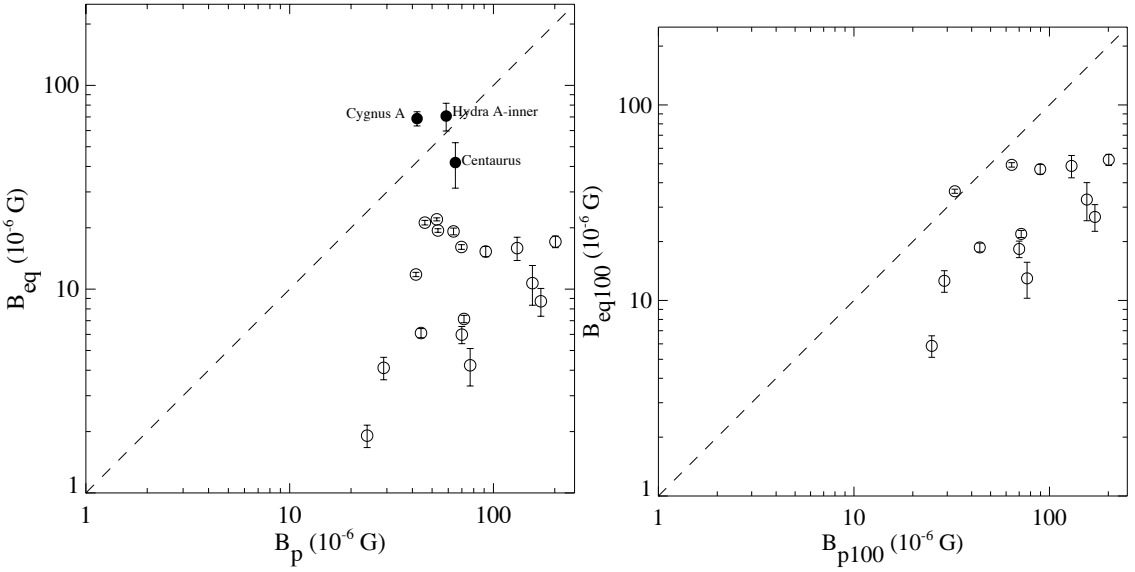


Figure 4.3: *Left:* Equipartition magnetic field strength vs. the field strength required for pressure equilibrium ( $k = 1$ ,  $\phi = 1$ ). *Right:* The same, but for  $k = 100$ . Symbols are the same as in Figure 4.2.

### 4.3 Does Equipartition Apply in the Lobes of the Radio Sources?

Historically, equipartition between the magnetic field energy and the energy in relativistic electrons and heavy particles, which results in the minimum total energy, was used to put limits on the magnetic field strengths in the lobes of radio sources (first proposed by [Burbidge, 1956](#)). We can test whether equipartition applies for our sources with the additional constraints available from the X-ray data (e.g., [Blanton et al., 2001](#)).

In Figure 4.3, left, we compare the equipartition magnetic field strength ( $B_{eq}$ ) with the field strength required for pressure equilibrium ( $B_p$ ) assuming  $k = 1$  and

$\phi = 1$ . We find that for most of the objects  $B_{\text{eq}}$  cannot support the cavities against the ICM pressure, with the exception of Centaurus, Cygnus A, and Hydra A - inner lobes. However, these systems are three out of five systems that were classified as radio-active. For the other two of them (M84 and M87), the pressure equilibrium equation didn't have a solution, so they are not plotted. These objects are likely in a driving stage where the lobes are still being inflated (see Section 4.2). For  $k = 100$  (Figure 4.3, right), many objects shift closer to equality. However, we note that in this plot we are missing many systems for which the pressure equilibrium equation doesn't have a solution for this value of  $k$ . In general, in order for the equipartition magnetic field strengths to be equal to the field strengths required for pressure equilibrium,  $k$  must vary from  $\sim 1$  to 35000 (see  $k_{\text{eq}}$  in Table 4.1). Therefore, if theoretical arguments are correct, with  $k$  ranging from 1 to 2000, such high values of  $k_{\text{eq}}$  imply either that equipartition doesn't apply in the lobes of the radio sources or that there is additional pressure support from other sources (e.g., hot thermal gas). The latter scenario needs to be further investigated with deep *Chandra* images (see e.g., [Gitti et al., 2007](#); [Sanders & Fabian, 2006](#)).

In order to calculate  $B_p$ , we assumed  $k = 1$  or  $k = 100$ . However,  $k$  does not have an important influence on  $B_p$ . In equation 11 with  $k = 1$ , for the majority of the systems (except Cygnus A and Hydra A - inner lobes) the second term dominates (the pressure from magnetic fields). Conversely, for the equipartition magnetic field,

$k$  is the largest source of uncertainty. The estimate of  $B_{\text{eq}}$  will increase by a factor of  $\sim 4$  and  $\sim 14$ , if  $k = 100$  and  $k = 1000$ , respectively.

Lastly, we note that in general, our lobe magnetic field strengths are higher (by a factor of  $\sim 5$ ) than the cluster-wide magnetic fields inferred from Faraday rotation ( $\sim 12 \mu\text{G}$  for cooling flow clusters, [Vogt & Enßlin, 2003](#)), especially for the clusters that we classified as radio-filled. This finding is in agreement with the scenario that the AGNs are responsible for the cluster-wide magnetic fields.

## 4.4 Synchrotron Spectrum and Ages

We can use the synchrotron spectrum to derive the spectral age of the radio-emitting electrons, which gives a lower limit on the age of the radio source. By comparing these ages to the X-ray-derived ages (see Section 3.1), we can investigate the underlying assumptions that go into their determination.

The break frequency is determined by fitting the radio spectrum with the KP, JP, or CI models (for details of the code, see [Carilli et al., 1991](#)). The free parameters in these models are the injection index ( $\alpha_{\text{inj}}$ ), defined as the power law index at frequencies below the critical frequency, and the critical frequency itself ( $\nu_C$ ) above which the spectrum steepens. Under the assumption that the relativistic electrons inside the radio lobes lose their energy only by synchrotron emission and inverse Compton scattering, for the KP model the synchrotron break or critical frequency and the synchrotron age of a distribution of electrons are related through ([Slee et al.,](#)

2001; Feretti & Giovannini, 2007):

$$t_{\text{syn}} = 1060 \frac{B^{1/2}}{B^2 + \frac{2}{3}B_m^2} [\nu_C(1+z)]^{-1/2} \text{ Myr}, \quad (4.1)$$

where the magnetic field  $B$  is in units of  $\mu\text{G}$ , the break frequency  $\nu_C$  is in units of GHz, and the magnetic field equivalent of the 3K radiation, to account for inverse-Compton losses ( $B_m = 3.25[1+z]^2$ ) is in units of  $\mu\text{G}$ .

The largest uncertainty in the synchrotron age calculation is the magnetic field strength. Siah & Wiita (1990) and Wiita & Gopal-Krishna (1990) discussed the difficulty of estimating the strength of the magnetic field and how inhomogeneities in the magnetic field can affect the spectral age estimates. Also, Tribble (1993), by studying the effects of a random magnetic field on the spectral age calculation, showed that the magnetic field rather than the pitch angle distribution is responsible for the difficulty of estimating the spectral age (JP or KP model). Inhomogeneities in the magnetic field can have important consequences for the radio sources such as a deceptively short radiative age (Eilek, 1996; Eilek et al., 1997). Katz-Stone et al. (1999), using spectral tomography, showed that there are other consequences of an inhomogeneous magnetic field such as the overlapping structure of different spectral indices present in many radio sources which make the age calculation meaningless (for a review, see Rudnick, 2002).

In order to calculate the break frequencies for the radio lobes, we used the method described in Carilli et al. (1991). In addition to our data (see Table 2.3), we also used data from the literature to obtain lobe fluxes at least three different frequencies. In

order to get the fluxes for the lobes, we subtracted any contribution due to the core from the total flux. For the literature data, the fluxes from the cores were calculated by extrapolation using the known core fluxes from our own observations and the calculated spectral index between two different frequencies (see Section 2.2.1). We fitted the data with both the KP and JP models at a given injection index ( $\alpha_{\text{inj}}$ ). We selected the break frequency that corresponded to the best fit of the model to the data. In general, the KP and JP models give similar fits of the lobes' spectra, but in some cases the KP model fits better the higher frequency points (as in e.g., A4059 and Perseus). As a result, we use the break frequencies derived with the KP model (see Figure 4.4).

Table 4.3 lists the break frequencies that we derived by fitting the spectrum with a KP model, the derived injection index, and the corresponding chi-squared statistic. For our sample, the injection index varies from 0.5 to 1.2, with MKW 3S, A133, and MS 0735.6+7421 having the highest values (between 0.9 and 1.2). However, the preferred value for the injection index in the literature is 0.5 or sometimes 0.75 (Komissarov & Gubanov, 1994). Our higher values of the injection index for A133 (0.9) and MKW 3S and MS 0735.6+7421 (1.2) suggest that our data are sensitive to a different region of the asymptotic spectrum than those of Slee et al. (2001) and Komissarov & Gubanov (1994). As a result, these sources may have a much lower break frequency than we measure, consistent with previous findings (Komissarov & Gubanov, 1994; Slee et al., 2001). For some systems, we were not able to obtain fluxes

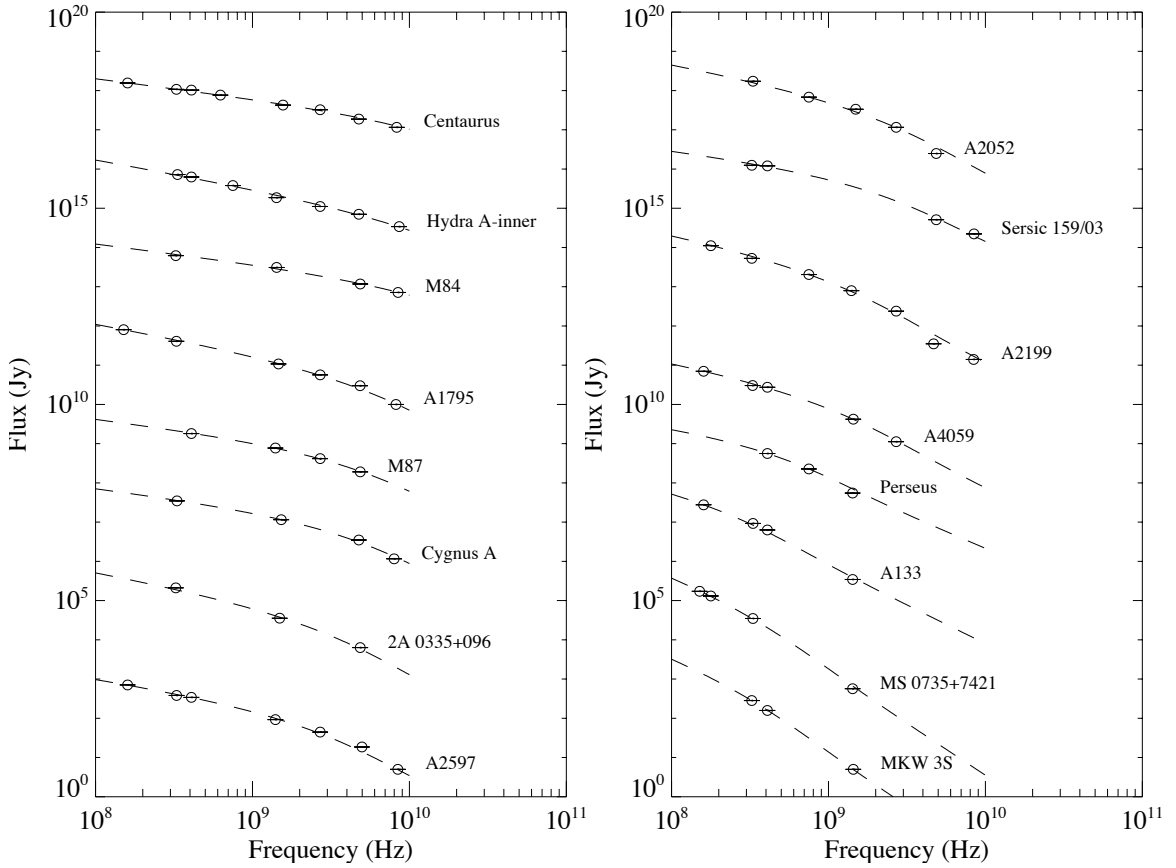


Figure 4.4: The spectra of the radio lobes organized by the spectral index between 327 MHz and 1400 MHz, from the flattest spectrum (top left) to the steepest spectrum (bottom right). Each spectrum is shifted by an arbitrary factor so that all spectra can be shown in one plot. In order to have as many data points as possible we complemented our data with literature values (see Table 4.3). The data were fit with the KP model in order to derive the break frequency. We show the fit with the best  $\chi^2$  value. Both the input parameters for the KP model ( $\alpha_{\text{inj}}$ ) and the results of the model ( $\nu_C$ ,  $\chi^2$ ) are listed in Table 4.3.

at three frequencies (see Table 2.3). In these cases, to derive the break frequency, we use the approximation of Myers & Spangler (1985) for a given spectral index (and assuming  $\alpha_{\text{inj}} = 0.5$ ). Four other systems we have no estimates of the break frequency. In this situation are Zw 3146, because of the lack of any lobe emission estimates at any of the frequencies at which we observed it; MACS J1423.8+2404, where we were

not able to separate the lobe emission from the core emission; and Zw 2701 and HCG 62, which have lobe emission at only 327 MHz and 1.4 GHz respectively (see Table 4.3). We computed the synchrotron ages using equation 3.14 and the minimum energy estimate of the magnetic field strength in the lobes ( $B_{\text{eq}}$ ) or the magnetic field required for pressure equilibrium ( $B_p$ ). In Table 4.1 we list the equipartition magnetic field strengths, the magnetic field strengths required for pressure equilibrium (for  $k = 1$  and  $\phi = 1$ ), and the corresponding synchrotron ages ( $t_{\text{syn}}^{\text{eq}}, t_{\text{syn}}^p$ ).

Table 4.3. Break frequency

Name	$\alpha_{\text{inj}}^{\text{a}}$	$\chi^2_{\text{b}}$	$\nu_C^{\text{c}}$ (MHz)	$\Delta^{\text{d}}$	$f(\Delta)$	$\nu_C^{\text{cor e}}$ (MHz)	References <sup>f</sup>
A133	0.9	1.4	$330 \pm 10$	1.24	1.8	$600 \pm 20$	10(408), 15(160)
A262	0.5	...	660*	1.23	1.8	1200	...
Perseus	0.5	0.5	< 408	1.33	2.1	< 870	3(408), 11(750)
2A 0335+096	0.7	0.5	$2300 \pm 100$	1.21	1.7	$3900 \pm 200$	4(1400)
A478	0.5	...	680*	1.15	1.5	1000	...
MS 0735.6+7421	1.2	2.4	$270 \pm 20$	1.77	3.8	$1000 \pm 100$	8(151), 6,12(178)
Hydra A - outer lobes	0.5	...	160*	2.45	5.9	930	...
Hydra A - inner lobes	0.7	2.8	> 8610	1.47	2.7	> 23000	9(750), 20(408, 2700)
RBS 797	0.5	...	690*	1.32	2.1	1500	...
Zw 2701	...	...	...	1.02	1.1	...	...
Zw 3146	...	...	...	1.33	2.1	...	...
M84	0.5	1.6	> 8460	1.54	2.9	> 25000	...
M87	0.5	0.3	$3400 \pm 300$	1.17	1.5	$5200 \pm 400$	10(408), 13(2700), 19(1400)
Centaurus	0.5	2.0	> 8310	1.32	2.1	> 17000	9(625), 10(408), 14(2700), 15(160)
HCG 62	...	...	...	1.50	2.8	...	...
A1795	0.7	0.6	$4800 \pm 300^{\text{g}}$	1.10	1.3	$6300 \pm 400$	1(2700), 7(4850), 15(80), 18(151)
A1835	0.5	...	680*	1.05	1.2	780	...
MACS J1423.8+2404	...	...	...	1.13	1.4	...	...
A2052	0.7	6.0	$1800 \pm 100$	1.11	1.4	$2500 \pm 100$	11(750), 17(2700)
MKW 3S	1.2	0.1	< 324	1.22	1.7	< 560	10(408)
A2199	0.75	8.4	$970 \pm 50$	1.38	2.3	$2200 \pm 100$	1(2700), 2, 5(159), 4(1400), 11(750)
Cygnus A	0.5	0.1	$3000 \pm 200$	1.71	3.6	$11000 \pm 1000$	...
Sersic 159/03	0.5	3.2	$1500 \pm 100$	1.12	1.4	$2100 \pm 100$	...
A2597	0.6	0.6	$1900 \pm 100$	1.04	1.2	$2200 \pm 100$	10(408), 15(80, 160)
A4059	0.7	1.0	$850 \pm 25$	1.14	1.4	$1230 \pm 40$	4(1400), 10(408), 15(160), 16(2700), 21(4860)

<sup>a</sup>The injection index used in the KP model.<sup>b</sup>The chi-squared statistic given by the KP model.<sup>c</sup>The break frequency corresponding to the best-fit KP model, except those values marked with an asterisk, which were computed using the relation of Myers & Spangler (1985), assuming  $\alpha_{\text{inj}} = 0.5$ . Some systems lack a break-frequency estimate either because no lobe emission was detected (Zw 3146, Zw 2701, and HCG 62) or due to our inability to separate the lobe emission from the core emission (MACS J1423.8+2404).<sup>d</sup>The linear expansion factor for a volume of plasma.<sup>e</sup>The adiabatic-loss-corrected break frequency.<sup>f</sup>The radio fluxes from the literature used to derive the break frequency ( $\nu_C$ ); the number in parentheses are the frequencies in MHz. This break frequency is for the inner radio lobes seen clearly at 1400 MHz and 8500 MHz; the X-ray cavity is much farther out.

References. — (1) Andernach et al. (1981); (2) Bennett (1962); (3) Burbidge &amp; Crowne (1979); (4) Condon et al. (1998); (5) Edge et al. (1959); (6) Gower et al. (1967); (7) Gregory &amp; Condon (1991); (8) Hales et al. (1991); (9) Haynes et al. (1975); (10) Large et al. (1991); (11) Pauliny-Toth et al. (1966); (12) Pilkington &amp; Scott (1965); (13) Reich et al. (2000); (14) Sadler (1984); (15) Skee (1995); (16) Vollmer et al. (2005); (17) Wall &amp; Peacock (1985); (18) Waldram et al. (1996); (19) White &amp; Becker (1992); (20) Wright &amp; Orrupceek (1990); (21) Wright et al. (1994).

The synchrotron ages computed using equation 3.14 ( $t_{\text{syn}}^{\text{eq}}$ ) are estimates of the “spectral ages,” the time elapsed since acceleration of the particles, and they are based on the break frequency estimates and magnetic field strengths. There are many examples in the literature where this approach was used in order to obtain an estimate of the age of a radio source (e.g., Myers & Spangler, 1985; Alexander & Leahy, 1987; Carilli et al., 1991; Liu et al., 1992; Feretti et al., 1998; Murgia et al., 1999; Mack et al., 1998). However, in addition to synchrotron losses, adiabatic-expansion losses can also take place in the lobes of the radio sources. Adiabatic-expansion losses occur as a blob of plasma expands, causing a decrease in the magnetic field strength and particle energies (Scheuer & Williams, 1968). As a result, the observed break frequency will be reached earlier and the corresponding spectral ages ( $t_{\text{syn}}^{\text{eq}}$ ) are overestimated. Blundell & Alexander (1994) computed a formula for break frequency versus age, which takes into account both synchrotron losses and adiabatic-expansion losses:  $\nu_C = \nu_C^{\text{cor}} f(\Delta)$ , where  $\nu_C$  is the measured break frequency in the presence of adiabatic-expansion losses, and  $f(\Delta) = 16\Delta^6/[(\Delta + 1)^2(\Delta^2 + 1)^2]$ , where  $\Delta$  is the linear-expansion factor for a volume of plasma. We calculated  $\Delta$  as the ratio between the final radius of the bubble at the end of the adiabatic expansion ( $r_1$ ) and the initial radius of the bubble at the start of the adiabatic expansion ( $r_0$ ). According to the adiabatic-expansion law:  $r_1 = r_0(p_1/p_0)^{-\frac{1}{3\gamma}}$ , where  $\gamma$ , the ratio of specific heats, is assumed to be 4/3, and  $p_1$  and  $p_0$  are the gas pressures at the location of the X-ray cavity and at the center of the cluster respectively (derived from X-ray observations, see Rafferty et al., 2006).

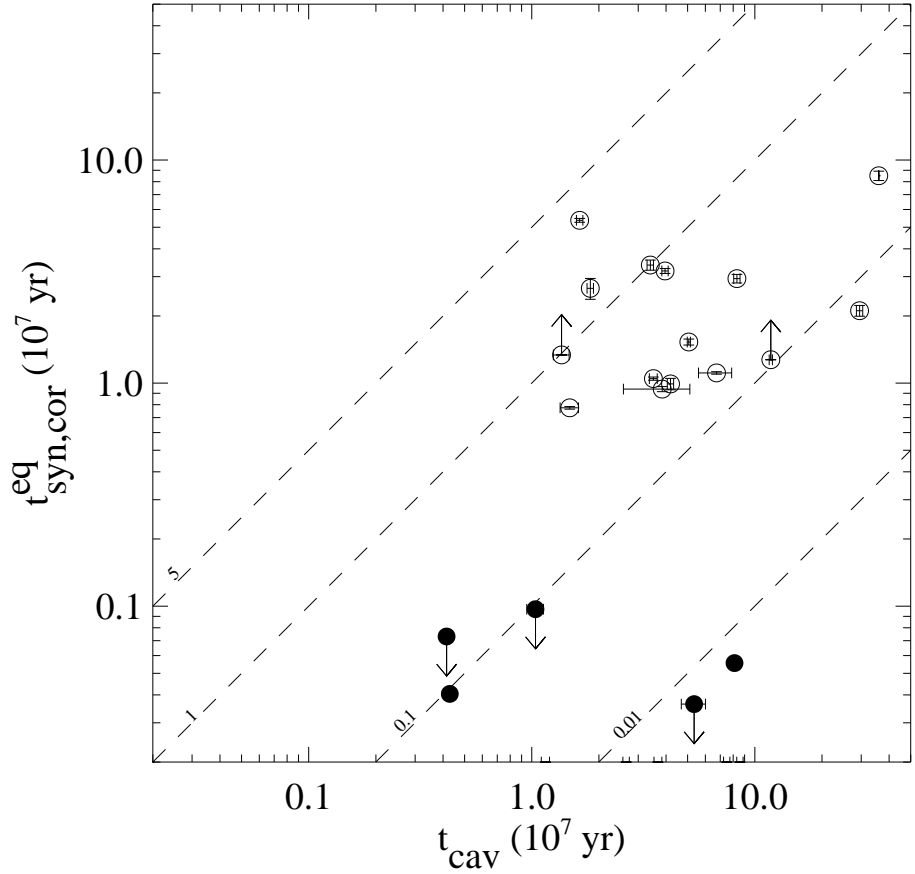


Figure 4.5: The synchrotron age corrected for adiabatic-expansion losses versus the buoyancy age. Symbols are the same as in Figure 4.2. Dashed lines denote different ratios of the adiabatic-loss-corrected synchrotron age to the buoyancy age.

We assume that the bubble starts at the cluster center and calculate  $r_0$  from this equation. Table 4.1 lists the adiabatic-loss-corrected ages ( $t_{\text{syn},\text{cor}}^{\text{eq}}$ ), and the factors involved in its derivation ( $\Delta$ ,  $f(\Delta)$  and  $\nu_C^{\text{cor}}$ ) are listed in Table 4.3.

In Figure 4.5, we compare the adiabatic-loss-corrected synchrotron ages of the radio lobes to the buoyancy ages of the cavities. In this comparison, one can assume either that the buoyancy ages are the true ages or that the synchrotron ages are the true ages. If we assume that the buoyancy ages represent the true ages, we find that

the synchrotron ages systematically underestimate the ages of the radio sources by a mean factor of  $\sim 20$  with a median value  $\sim 4$ . This finding agrees with [Eilek \(1999\)](#), who finds that the synchrotron ages are lower limits on the radio source ages. In several cases the synchrotron age is higher than the X-ray age by a factor as high as  $\sim 5$ . This result might be explained if the buoyancy ages are underestimated by a factor of few due to projection effects and drag effects (due to the magnetic field or to the material in the rims). On the other hand, some of the systems have a buoyancy age much larger than the synchrotron age. In the case of young sources (the active ones), which are likely being driven, the shorter synchrotron age is probably a better estimate of the age than the buoyancy age, since the bubble is not yet buoyant. Additionally, some of the ghost or intermediate systems are still being pumped by the radio source ([Clarke et al., 2005](#); [Wise et al., 2007](#)), and the synchrotron age would be too low due to the continuous injection of new electrons.

If, however, the synchrotron age represents the true dynamical age of the cavity system, Figure 4.5 implies that most of the cavities are being strongly driven, or that they form at radii close to their observed radii. If we assume that they are driven, Figure 4.5 implies that they are moving  $\sim 4$  to  $\sim 20$  times faster than the buoyancy age suggests, so in most cases substantially supersonically. As a result, in these systems we would expect to see shocks. The discovery of mild shocks in some systems (see [McNamara & Nulsen, 2007](#)) fits with the above scenario, and we may

expect to see shocks in all of the other systems for which the synchrotron age is much less than the buoyancy age of the cavity.

We can test in detail whether the synchrotron ages are indicative of the dynamical ages by calculating the implied Mach numbers,  $M = R/(t_{\text{syn,cor}}^{\text{eq}} c_s)$ , where  $R$  is the distance from the cluster center to the cavity center and  $c_s$  is the velocity of sound in the pre-shock gas, both taken from [Rafferty et al. \(2006\)](#). For the objects whose buoyancy age is  $\sim 4$  times higher than the synchrotron age, the Mach numbers lie between 1.4 and 2.2, similar to the observed range in clusters with weak shocks ([McNamara & Nulsen, 2007](#)). However, the rest of the objects have much higher Mach numbers, between 3.5 and 8.0 for M84, M87, Centaurus, MKW 3S, and MS 0735.6+7421, 30 for Cygnus A, and 50 for Hydra A - inner. For objects like Cygnus A, we know that shocks have been seen in the deep *Chandra* images, but with much lower Mach numbers than we calculate, mostly due to the fact that the synchrotron age is a lower limit of the true age. Furthermore, to check if the shocks that we predict could have been seen in existing X-ray observations we compute the X-ray surface brightness jump at the shock using the Rankine-Hugoniot relations ([Spitzer, 1978; Lang, 1999](#)):

$$\frac{\rho_2}{\rho_1} = \frac{(\gamma + 1)M^2}{(\gamma - 1)M^2 + 2} \quad (4.2)$$

and

$$\frac{T_2}{T_1} = \frac{[2\gamma M^2 - (\gamma - 1)][(\gamma - 1)M^2 + 2]}{(\gamma + 1)^2 M^2}, \quad (4.3)$$

where  $\rho_1$  ( $\rho_2$ ) and  $T_1$  ( $T_2$ ) represent the pre-shock (post-shock) density and temperature, and  $\gamma = 5/3$  is the ratio of specific heats.

Approximately 50% of the systems in our sample have  $M > 1$ . The resulting X-ray surface brightness jumps for these systems are between  $\sim 10 - 500$ ; however, the observed surface brightness jumps will be diluted by projection effects and adiabatic expansion. Nevertheless, such surface brightness jumps should be readily apparent in existing images but have not been seen. In general, our predicted surface brightness jumps are much higher than the observed ones. Therefore, the synchrotron ages are not good estimates of the dynamical ages. We conclude that the synchrotron and buoyancy ages are uncoupled. Nevertheless, the existence of weak shocks in many of these systems supports the conclusion that one may expect to see shocks whenever the synchrotron age is much lower than the buoyancy age. However, our calculation is only an estimate and may not apply in all cases (e.g., in Perseus, [Fabian et al., 2006](#), found a mild shock, but from our calculations  $M < 1$ ).

## 4.5 Radiative Efficiencies

### 4.5.1 Radiative Efficiencies for the Initial 18-System Sample

An important problem is the degree of coupling between jet power (traced by the X-ray cavities) and radiative power (the bolometric radio luminosity). Historically, radio sources were thought to have low radiative efficiencies from purely theoret-

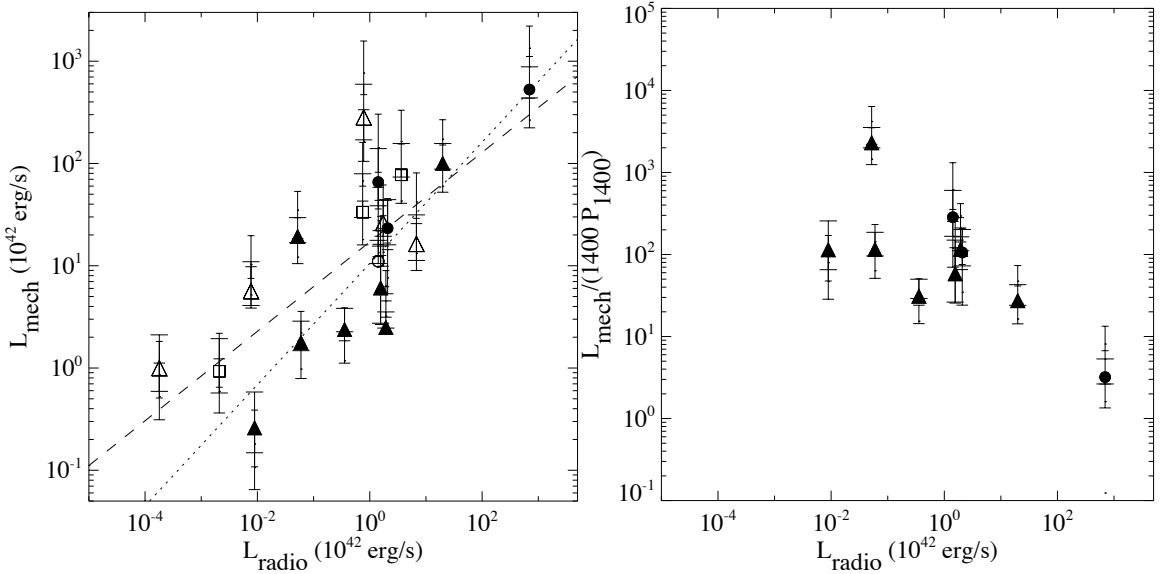


Figure 4.6: *Left:* Mechanical luminosity (cavity power) vs. radio luminosity for the initial 18-system sample. The symbols and wide error bars denote the values of the mechanical luminosity calculated using the buoyancy timescale. The short and medium-width error bars denote upper and lower limits of the mechanical luminosity calculated using the sound speed and refill timescales, respectively. The different symbols indicate FOMs of 1 (*circles*), 2 (*triangles*), and 3 (*squares*). Filled symbols denote radio-filled cavities, and empty symbols denote ghost cavities. Each point represents the sum of mechanical luminosities of each bubble type. The best-fit lines are shown for the entire sample (*dashed line*) and for the radio-filled cavities only (*dotted line*). *Right:* The ratio of mechanical luminosity to  $\nu P_\nu$  at 1400 MHz vs. radio luminosity for the radio-filled cavities only.

cal considerations. Now however, the cavities allow observational constraints to be placed on the radiative efficiencies. Accurate estimates of the radiative efficiencies are important for jet models, accretion models, and models of feedback in galaxy formation.

In Figure 4.6, we present two plots showing the mechanical luminosity versus the total radio luminosity (*left*) and the total radio luminosity versus the ratio of the mechanical luminosity to the monochromatic, 1.4 GHz radio luminosity (*right*). In

each plot we distinguish between radio-filled and ghost cavities, shown with filled symbols and empty symbols respectively. The “error bars” for each point reflect the range of instantaneous mechanical luminosity implied by the range in possible ages. The data are taken or are derived from Tables 2.1 and 2.2.

The left-hand panel of Figure 4.6 shows a trend between the radio luminosity and mechanical luminosity, with the sense that more luminous radio sources tend toward larger mechanical luminosities. This trend seems to be shared by both the radio-filled cavities and the ghost cavities, in spite of the use of the current central radio power for both the filled cavities and the ghosts, to which the current central source may be unrelated. No segregation by FOM is seen. The relation between the two luminosities appears to be roughly a power law. To quantify this relation, we used a linear least-squares fit to the logarithms of the data, with errors in mechanical luminosity given by the extreme values for each system. We show in Figure 4.6 the best-fit line for the entire sample (*dashed line*), given by

$$L_{\text{mech}} = 10^{25 \pm 3} (L_{\text{radio}})^{0.44 \pm 0.06}, \quad (4.4)$$

and for the radio-filled cavities only (*dotted line*), given by

$$L_{\text{mech}} = 10^{18 \pm 4} (L_{\text{radio}})^{0.6 \pm 0.1}. \quad (4.5)$$

In both cases, the mechanical luminosity scales as the radio luminosity to approximately the one-half power over six decades of radio power, albeit with large scatter.

The relative contribution of cosmic scatter and observational uncertainty is hard to judge without precision radio data at a variety of wavelengths and without a better understanding of the bubble production timescale. Nevertheless, the existence of this trend demonstrates quantitatively that the radio sources are indeed creating the cavities. The radio sources are not simply filling preexisting voids in the ICM created by other processes. Furthermore, the synchrotron luminosity and mechanical luminosity do not scale in direct proportion to each other. This relationship implies that the synchrotron luminosity cannot be used to infer the mechanical power of a radio jet in a simple fashion.

An important and poorly understood aspect of radio source physics is the degree of coupling between the mechanical (kinetic) luminosity of radio sources and their synchrotron luminosity. This coupling is theoretically tied to the magnetic field strength and age of the source (see [De Young, 1993](#); [Bicknell et al., 1997](#)), neither of which can be measured reliably from radio data alone. Radio sources are inefficient radiators. The ratio of mechanical power to radio power is typically assumed to range between 10 and 100, almost entirely on theoretical considerations ([De Young, 1993](#); [Bicknell et al., 1997](#)). On the other hand, measurements of the the X-ray cavity sizes and surrounding gas pressures provide unique estimates of their ages and mechanical luminosities, independent of the radio properties. We evaluate the ratio of mechanical energy to radio power by plotting the ratio of mechanical power in the bubbles to monochromatic, 1.4 GHz synchrotron luminosity, assuming  $E_{\text{mech}} = 1pV$  of energy

per radio lobe, against the radio luminosity in the right-hand panel of Figure 4.6. This ratio ranges from a few to a few hundred for the powerful sources, which is broadly consistent with theoretical estimates (see De Young, 1993; Bicknell et al., 1997). On the other hand, Abell 478 has a ratio exceeding a few thousand. To the extent that X-ray cavities provide a good measure of the mechanical energy of radio sources, the large variation in this ratio indicates that radio luminosity is not necessarily a reliable probe of the available mechanical energy.

There are several factors that can introduce scatter into our estimate of the ratio of radio to kinetic power. The most important is probably intrinsic differences between the radio sources themselves, a consequence of dramatic changes in radio luminosity with time. Certainly, if radio outbursts are to compensate for radiative losses in cooling flows, then the absence of radio emission from some systems requires large variations of radio luminosity with time. On the other hand, the  $pV$  energy of the bubbles alone would tend to underestimate the mechanical luminosity of radio sources by factors of several if energy-dissipating shocks are generated, or if the bubbles expand non-adiabatically (they leak), or if the internal energy of the bubbles is boosted with a relativistic plasma.

### 4.5.2 Radiative Efficiencies for the Extended 24-System Sample

In Figure 4.7 we plot the jet power versus the bolometric radio luminosity for the total source (*left*) the lobes (*right*) of the radio sources. Note that the cavity power here has been calculated assuming  $4pV$  of energy per cavity, whereas the mechanical luminosity (shown in Figure 4.6) assumes  $1pV$  per cavity; otherwise they are identical (both assume the buoyancy age). This figure shows the same trend between bolometric radio luminosity and cavity power as seen in Figure 4.6 for the initial 18-system sample. The most radio-luminous objects generally have the largest cavity power. This trend is shared by both radio-filled cavities and radio-ghost cavities, but the ghost cavities tend to have a higher ratio of jet power to radiative power.

As for the 18-system sample, we again fit a linear function to the logarithms of the data. The best fit line for the entire sample is given by

$$L_{\text{mech}} = 10^{25 \pm 2} (L_{\text{radio}})^{0.47 \pm 0.05}, \quad (4.6)$$

for the total source (the *dashed line* in Figure 4.7, *left*) and for the lobes only (the *dashed line* in Figure 4.7, *right*)

$$L_{\text{mech}} = 10^{25 \pm 2} (L_{\text{radio}})^{0.46 \pm 0.05}. \quad (4.7)$$

The relation between the jet power and radio power is similar to our previous finding where we used literature data in order to quantify the radio power (see equation 4.4).

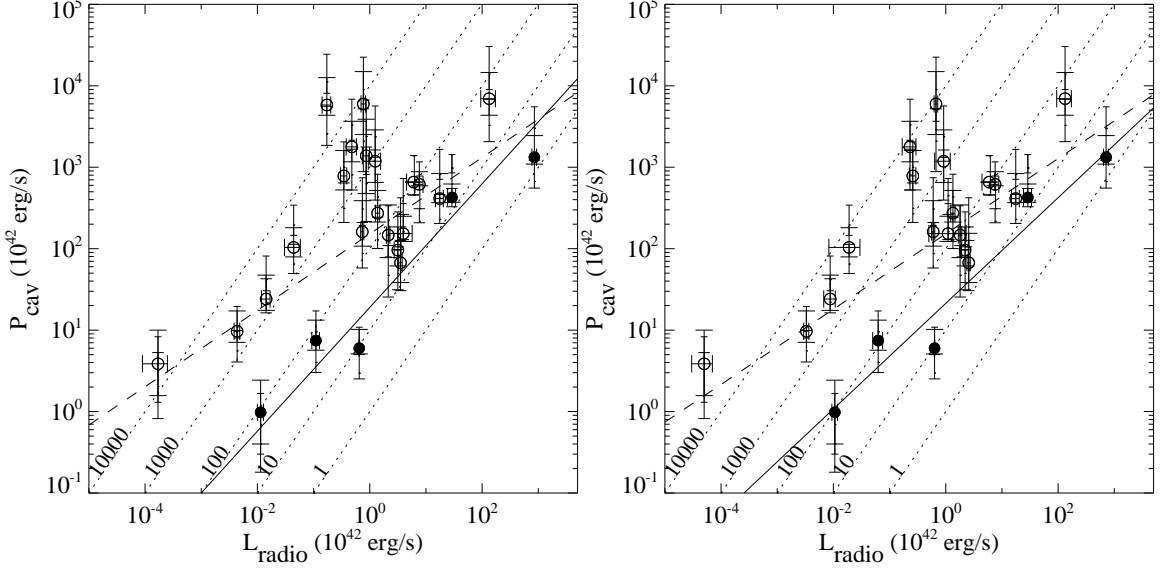


Figure 4.7: Cavity power (mechanical luminosity) versus bolometric radio power for the expanded 24-system sample for the total source (*left*) and lobes only (*right*). Dotted lines denote different ratios of cavity power to bolometric radio luminosity. The dashed line shows the best-fit power law for the entire sample; the solid line shows the fit for the radio-filled systems only. Symbols are the same as in Figure 4.2.

When we use only the active sources, the best fit line is given by

$$L_{\text{mech}} = 10^{12 \pm 5} (L_{\text{radio}})^{0.75 \pm 0.13}, \quad (4.8)$$

for the total source (the solid line in Figure 4.7, *left*) and for the lobes only (the solid line in Figure 4.7, *right*)

$$L_{\text{mech}} = 10^{16 \pm 5} (L_{\text{radio}})^{0.64 \pm 0.11}. \quad (4.9)$$

For the active, radio-filled sources, the jet power scales almost linearly with the radio power, as found by Nipoti & Binney (2005).

However, there is a great deal of scatter about these trends, similar to our previous finding for the initial 18-system sample. In Figure 4.7 we see that the ratio of cavity

power to radio power ranges from a few to a few thousand. About half of our systems fall within a ratio of  $10 - 100$ , with the rest being on average vastly larger (radiative efficiencies of 0.001). The median value for the ratio of cavity power ( $4pV/t$ ) to radio power is 106 when we consider the total radio luminosity, and 117 when we consider only the lobe radio luminosity. However, the mean values for the ratio of cavity power to radio power are 2810 (total radio luminosity) and 4698 (lobe radio luminosity). The scatter that we see in Figure 4.7 is much larger than the range in theoretical estimates, which generally predict a ratio of  $10 - 100$  (De Young, 1993; Bicknell et al., 1997). As a result, radio luminosity is not a good predictor of the total jet power. It is important to note that we did not include the contribution of shocks in the cavity power calculation for any of the objects. Deep Chandra X-ray images show that the lobes create mild shocks during their expansion, with a Mach number lying between 1.2 and 1.7 (Fabian et al., 2006; McNamara et al., 2005; Nulsen et al., 2005a,b; Sanders & Fabian, 2006; Wise et al., 2007; McNamara & Nulsen, 2007). In cases where shocks are present, the cavity powers are lower limits to the jet powers, and as a consequence the radiative efficiencies are overestimated.

Radio-source aging may be responsible for some of the scatter in this plot: in general, the most radiatively efficient systems (e.g., Cygnus A and M87) are also the youngest ones and may still be driven by the radio source. Conversely, the most radiatively inefficient systems are generally the older ones. In this scenario, the sources start with high radiative efficiencies when they are young and, as they

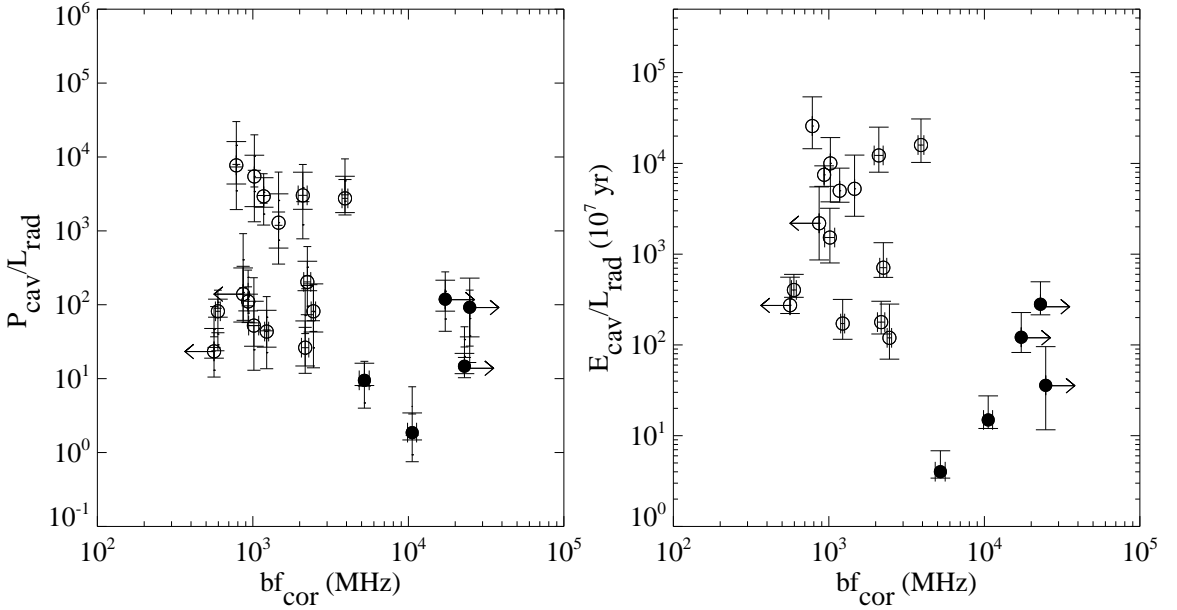


Figure 4.8: *Left:* The ratio of cavity power to lobe bolometric radio power versus the break frequency (corrected for adiabatic expansion). *Right:* The ratio of cavity energy ( $4pV$ ) to lobe bolometric radio power versus the break frequency (corrected for adiabatic expansion). Symbols are the same as in Figure 4.2.

age, their efficiencies decrease. Because  $P_{cav} \sim 1/t$  (neglecting changes in  $pV$ ) and  $L_{radio} \sim (-dE/dt) \sim E^2 \sim 1/t^2$  (neglecting changes in  $B$ ), the radiative efficiency falls as  $\sim 1/t$ . This relation produces evolutionary tracks in Figure 4.7 with a slope 1/2. For the most radiatively inefficient sources, following such a track would imply unrealistically high radio luminosities and cavity powers in the past. Therefore, either the sources don't start with the same efficiency, or aging is not the only factor that induces scatter in Figure 4.7.

To further investigate whether the scatter is due to radio aging, in the left panel of Figure 4.8 we plot the ratio of cavity power to radiative power (the inverse of radiative efficiency) versus the adiabatic-expansion-corrected break frequency. Only

a few objects are radiatively efficient (e.g, M87, Cygnus A, and Hydra A - inner). If the scatter in Figure 4.7 is a radio-aging effect, one would expect to see a correlation between radiative efficiency and the break frequency, such that those objects with high efficiencies have high break frequencies (and are therefore younger). However, while Figure 4.8 shows a segregation between young (radio-filled) objects, which may be still in a driving stage (e.g., M87, Cygnus A, etc.), and the older (ghost) objects (e.g., Hydra A - outer, A1835, etc.) and a tendency for objects with higher break frequencies to be radiatively efficient, no clear trend is present.

A similar segregation is seen in the right panel of Figure 4.8, where we plot the ratio of cavity energy to radiative power versus the adiabatic-expansion-corrected break frequency. The ratio of cavity energy to radiative power represents the timescale for the AGN to radiate away its cavity energy via synchrotron radiation. Since many of the objects have a very long timescale, longer than the Hubble time, the synchrotron radiation is generally a negligible fraction of the total energy budget currently. Only for a few objects is radiation important (e.g, M87, Cygnus A, and M84). As a result, aging does not appear to be the only factor that contributes to the large scatter in the radiative-efficiency plot.

Another factor that may contribute to the scatter in the radiative efficiency plot may be the interplay between the magnetic field and the particle content. From Figure 4.3, we concluded that for  $k = 1$ , only in a few sources (the youngest ones) can the equipartition fields achieve pressure equilibrium. For the majority of the objects, in

order for the equipartition fields to achieve pressure equilibrium, a much larger value of  $k$  is required (see Section 4.3 for details on this topic). However, in Section 4.2 we concluded that the large range in  $k$  is not due only to variations in magnetic field strengths, but may be due to differences in intrinsic radio properties. Because of the interrelations between magnetic field, particle content, and intrinsic radio properties such as radio luminosity, the scatter in Figure 4.7 is not due exclusively to one of these factors, but may be a result of all of them.

Cygnus A, the only FRII radio source in our sample, has the highest radiative efficiency ( $\sim 1$ ). There is a great deal of debate in the literature about the FR dichotomy of radio source morphology (Fanaroff & Riley, 1974). FRII radio sources are more powerful than the FRI radio sources, and they have radio lobes that end in hot spots (edge brightened), rather than dimming outward as do the radio lobes in FRI radio sources (edge darkened). There are several explanations in the literature for the separation between FRI and FRII radio sources which invoke one or more of the following scenarios: the deceleration of the jets by interactions with the ambient medium (De Young, 1993; Bicknell, 1995; Gopal-Krishna & Wiita, 2001), differences in jet composition (Celotti & Fabian, 1993; Reynolds et al., 1996), galactic mergers (Valtonen & Heinämäki, 2000), and differences in black hole spin (Meier, 1999) or black hole mass and accretion rate (Baum et al., 1995; Ghisellini & Celotti, 2001; Wold et al., 2005). Baum et al. (1995) postulated that when the central black hole is fed at low accretion rates, a low ratio of radiative power ( $L_{\text{radio}}$ ) to jet power ( $P_{\text{cav}}$ ) results, forming an

FRI source. Otherwise, if the black hole is fed at higher accretion rates, with a higher ratio of radiative to jet power, an FRII source is formed. This interpretation agrees well with the recent finding by [Heinz et al. \(2007\)](#), that the efficiency of conversion of accreting rest mass into jet power is higher for the low luminosity radio sources. Using our sample, it is impossible to make a separation between the FRI and FRII radio sources. However, our only FRII radio source (Cygnus A) has a similar fraction of total power in radiative luminosity and jet power (a radiative efficiency  $\sim 1$ ). The other sources in our sample have a lower ratio of radiative to jet power (a radiative efficiency  $\sim 0.1$  and below). The higher radiative efficiency for the FRII source is in good agreement with the scenario of [Baum et al. \(1995\)](#).

## 4.6 Radio Observations As a Tracer of Cavity Size

While deep X-ray observations are critical for measuring the AGN output (cavity and shock energy), these observations are difficult to obtain in many clusters, particularly at higher redshift. However, it is important to quantify the history of AGN output in clusters for a better understanding of the feedback process in galaxy formation and cluster preheating. This goal requires sensitive measurements of both the current rate of energy injection and the history of injection with cosmic time. Radio observations, properly calibrated to the total energy, may be a useful proxy for X-ray observations as a tracer of the energy injection. Our goal in this section is to use the observed cavity and radio properties to calibrate the radio-to-total jet power.

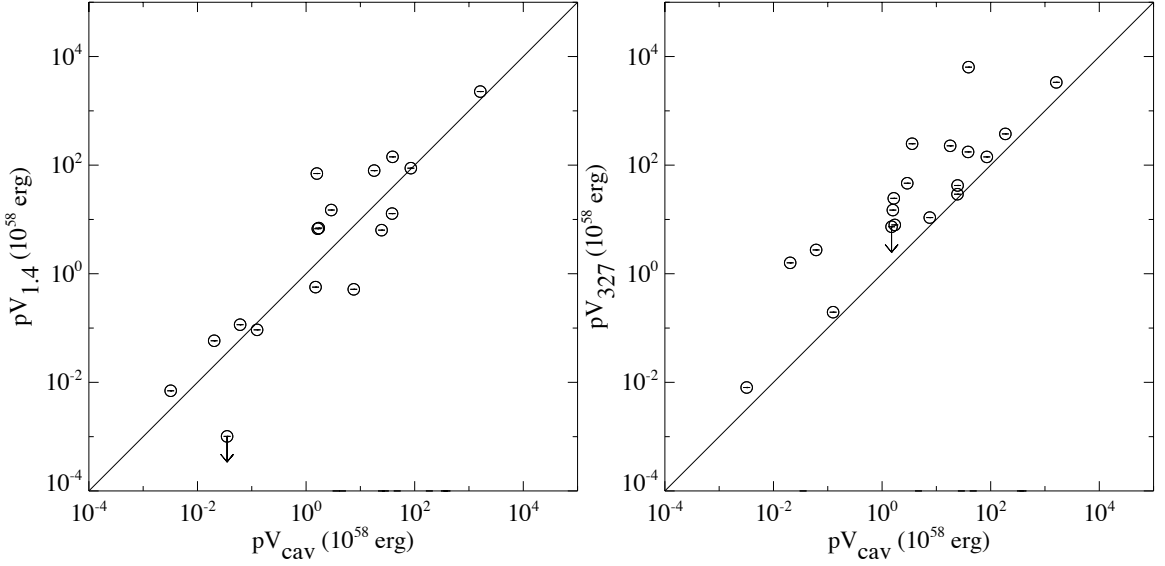


Figure 4.9: *Left:* Cavity energy inferred from the 1400 MHz radio emission versus that inferred from the X-ray data. *Right:* Cavity energy inferred from the 327 MHz radio emission versus that inferred from the X-ray data.

Low-frequency radio observations appear to be a good tracer of cavity activity over  $10^8$  yr timescales (Lane et al., 2004; Wise et al., 2007; Fabian et al., 2001). For example, 327 MHz radio maps have proved to be crucial for detecting the outer, fainter cavities in systems like Hydra A (Wise et al., 2007; Lane et al., 2004), due to a combination of a brighter source at 327 MHz (particularly important for steep spectrum sources, such as MS 0735.6+7421) and the generally higher sensitivity of the VLA at low frequencies to larger-scale structure (though depending on the array this may not always be the case). We note, however, that the system temperature of the VLA is higher at lower frequencies, so there is some trade off between the above effects and VLA's sensitivity to low surface brightness emission. In order to evaluate whether 327 MHz emission is generally a better predictor of cavity size than 1.4 GHz

emission, we compare  $pV_{\text{cav}}$ , where  $V_{\text{cav}}$  is the volume of the cavities from the X-ray maps against  $pV_{1.4}$ , where  $V_{1.4}$  is the volume of the lobes from 1.4 GHz radio maps, in Figure 4.9, left. We also plot  $pV_{\text{cav}}$  against  $pV_{327}$ , where  $V_{327}$  is the volume of the lobes from 327 MHz radio maps (Figure 4.9, right). The pressure on each axis is measured at the position of the radio lobe's center or cavity's center, and can therefore differ from one axis to another. In Table 4.4, we list the the lobe's size and the pressure at the lobe's center for both 327 MHz and 1.4 GHz radio lobes. The X-ray pressures are taken from [Rafferty et al. \(2006\)](#).

Table 4.4. Radio lobe sizes and pressures

Name	Component	$a_{327} \times b_{327}$ <sup>a</sup> (arcsec $\times$ arcsec)	$p_{327}$ <sup>b</sup> ( $10^{-11}$ erg cm $^{-3}$ )	$a_{1.4} \times b_{1.4}$ <sup>c</sup> (arcsec $\times$ arcsec)	$p_{1.4}$ <sup>d</sup> ( $10^{-11}$ erg cm $^{-3}$ )
A133	total	24 $\times$ 23	17 $\pm$ 3	31 $\times$ 10	10.7 $\pm$ 0.4
	east lobe	19 $\times$ 11	9 $\pm$ 2	16 $\times$ 9	10 $\pm$ 2
	west lobe	26 $\times$ 11	8 $\pm$ 2	12 $\times$ 8	12 $\pm$ 2
Perseus	north lobe	30 $\times$ 23	100 $\pm$ 20	20 $\times$ 17	120 $\pm$ 20
	south lobe	35 $\times$ 33	70 $\pm$ 20	15 $\times$ 14	160 $\pm$ 20
2A 0335+096	total	53 $\times$ 16	24.7 $\pm$ 0.4	59 $\times$ 35	23.5 $\pm$ 0.4
A478	total	< 6.1 $\times$ 4.6	130 $\pm$ 20	...	...
	north lobe	...	...	1.6 $\times$ 1.3	170 $\pm$ 20
	south lobe	...	...	1.9 $\times$ 1.6	170 $\pm$ 20
MS 0735.6+7421	north lobe	46 $\times$ 30	7.0 $\pm$ 0.8	35 $\times$ 23	9.3 $\pm$ 1.1
	south lobe	41 $\times$ 30	8.2 $\pm$ 1.2	38 $\times$ 27	8.7 $\pm$ 1.1
Hydra A - outer <sup>e</sup>	north lobe	120 $\times$ 90	2 <sup>f</sup>	...	...
	south lobe	120 $\times$ 45	5 <sup>f</sup>	...	...
Hydra A - inner <sup>g</sup>	north lobe	45 $\times$ 30	23.0 $\pm$ 0.4	34 $\times$ 21	23.0 $\pm$ 0.4
	south lobe	45 $\times$ 30	23.0 $\pm$ 0.4	35 $\times$ 20	22.0 $\pm$ 0.4
RBS 797	total	25 $\times$ 17	63 $\pm$ 7	...	...
	east lobe	...	...	4.2 $\times$ 3.7	92 $\pm$ 7
	west lobe	...	...	3.9 $\times$ 3.2	92 $\pm$ 7
Zw 2701	total	...	...	...	...
Zw 3146	total	...	...	...	...
M84	north lobe	40 $\times$ 31	2.7 $\pm$ 1.5	39 $\times$ 33	2.4 $\pm$ 0.2
	south lobe	42 $\times$ 26	2.6 $\pm$ 0.2	46 $\times$ 26	1.6 $\pm$ 0.2
M87	east lobe	120 $\times$ 86	10.8 $\pm$ 0.3	25 $\times$ 21	38 $\pm$ 4
	west lobe	110 $\times$ 74	15.6 $\pm$ 0.7	22 $\times$ 17	45 $\pm$ 3
Centaurus	total	72 $\times$ 43	13.3 $\pm$ 0.3	...	...
	east lobe	...	...	10 $\times$ 10	27 $\pm$ 3
	west lobe	...	...	13 $\times$ 13	24 $\pm$ 3
HCG 62	south lobe	...	...	< 5.6 $\times$ 2.8	9 $\times$ 1

Table 4.4 (continued)

Name	Component	$a_{327} \times b_{327}$ <sup>a</sup> (arcsec $\times$ arcsec)	$p_{327}$ <sup>b</sup> ( $10^{-11}$ erg cm $^{-3}$ )	$a_{1.4} \times b_{1.4}$ <sup>c</sup> (arcsec $\times$ arcsec)	$p_{1.4}$ <sup>d</sup> ( $10^{-11}$ erg cm $^{-3}$ )
A1795	north lobe	...	...	3.4 $\times$ 6.2	60 $\pm$ 10
	south lobe	...	...	4.7 $\times$ 2.6	60 $\pm$ 10
	total	...	...	...	...
A1835	total	...	...	...	...
MACS J1423.8+2404	total	37 $\times$ 21	12.2 $\pm$ 0.8	32 $\times$ 22	11.1 $\pm$ 0.7
A2052	total	59 $\times$ 54	12.2 $\pm$ 0.9	30 $\times$ 21	11.1 $\pm$ 1.1
MKW 3S	east lobe	31 $\times$ 17	19.5 $\pm$ 1.1	13 $\times$ 4	27 $\pm$ 7
A2199	west lobe	30 $\times$ 20	19.7 $\pm$ 1.1	9.0 $\times$ 7.3	27 $\pm$ 7
Cygnus A	east lobe	40 $\times$ 17	36.9 $\pm$ 0.9	32 $\times$ 15	33 $\pm$ 2
	west lobe	39 $\times$ 17	38.8 $\pm$ 0.9	34 $\times$ 17	31 $\pm$ 2
Sersic 159/03	total	52 $\times$ 14	18.6 $\pm$ 1.3	...	...
A2597	east lobe	19 $\times$ 19	36 $\pm$ 5	...	...
	west lobe	25 $\times$ 17	35 $\pm$ 6	...	...
	total	...	...	10 $\times$ 8	40 $\pm$ 4
A4059	north lobe	27 $\times$ 24	11 $\pm$ 1	23 $\times$ 18	9 $\pm$ 1
	south lobe	35 $\times$ 28	11 $\pm$ 1	25 $\times$ 20	8 $\pm$ 1

<sup>a</sup>Projected semimajor and semiminor axes of the lobes from the 327 MHz radio map.<sup>b</sup>The X-ray pressure at the center of the lobes measured from 327 MHz radio maps; the pressures are from Rafferty et al. (2006).<sup>c</sup>Projected semimajor and semiminor axes of the lobes from the 1400 MHz radio map.<sup>d</sup>The X-ray pressure at the center of the lobes measured from 1400 MHz radio maps; the pressures are from Rafferty et al. (2006).<sup>e</sup>The outer cavities; the cavities called E and F in Wise et al. (2007).<sup>f</sup>The pressure is from Birzan et al. (2004) and Rafferty et al. (2006); called A and B in Wise et al. (2007).<sup>g</sup>The inner cavities measured by Birzan et al. (2004) and Rafferty et al. (2007).

Figure 4.9 suggests that 1.4 GHz emission is a good tracer of cavity size in most cases, but there is a significant scatter, with many points falling below the equality line. Assuming that  $P_{\text{cav}}$  traces the minimum jet power, we note that 1.4 GHz underestimates the cavity power in some systems. On the other hand, at 327 MHz all of the points are above the line. It appears that 327 MHz recovers the energy better and is more sensitive to extended emission than 1.4 GHz. 327 MHz is not only a better tracer of cavity size, but can also be used as a predictor for the existence of X-ray cavities, such as in those objects that are well above the equality line in Figure 4.9, right (e.g., RBS 797). In both plots, some of the objects are close to the equality line (e.g., M84 and MS 0735.6+7421). In these cases, both 327 MHz and 1.4 GHz emission fills the cavities, and both frequencies are good tracers of cavity size. However, some of the objects that at 1.4 GHz lie below the equality line lie on the line at 327 MHz (e.g., A2199). In these cases, 327 MHz emission fills the cavities more fully. Therefore, for these objects 327 MHz emission is a better tracer of cavity size than 1.4 GHz emission.

Other objects are above the equality line in both plots (e.g., Abell 4059, Perseus, Abell 2052, RBS 797, and 2A 0335+096). In these cases, the radio lobes are larger than the cavities. It is possible that X-ray measurements may have underestimated the size of these cavities, or that the radio plasma has diffused beyond the cavities. The last explanation seems to be favorable for Abell 4059 if we think of it as an intermediate case in which the X-ray cavities are fading away (Heinz et al., 2002).

In Hydra A, the inner cavities that we measured from X-ray images are filled with 4.5 GHz radio emission. However, from Wise et al. (2007) we know that Hydra A has outer cavities that are filled with 327 MHz radio emission (from Lane et al., 2004). For Hydra A, we calculated two sets of data: one for the inner cavities using the  $pV_{\text{cav}}$  from Rafferty et al. (2006) and one for the outer cavities using the X-ray information from Wise et al. (2007). We did the same for M87, where Forman et al. (2006) discovered large outer cavities filled with 327 MHz radio emission (from Owen et al., 2000). In this case, in order to calculate  $pV_{327}$ , we used the radio map from Owen et al. (2000). There are other objects similar to Hydra A where the energy inferred from the 327 MHz radio emission is well above the energy we measure from X-ray images (e.g., RBS 797). In these objects we expect to see outer cavities in deeper *Chandra* images which will increase their total  $pV_{\text{cav}}$  estimates.

# CHAPTER 5

## Conclusions

We have presented an analysis of 18 systems taken from the *Chandra* archive having clear evidence for cavities in their X-ray emission. We have measured for the first time the distribution of the ratio of kinetic luminosity to monochromatic radio luminosity for a sample of radio sources. The ratio varies widely, with most objects ranging between few and a few hundred, assuming  $1pV$  of energy per cavity. X-ray cavities provide a unique probe of the mechanical power of radio jets, independently of the radio properties themselves.

We have extended our sample to 24 systems with X-ray cavities for which we have radio data at 4 different frequencies. By combining the X-ray data ([Rafferty et al., 2006](#)) with the VLA radio data we tried to understand the large scatter in the radiative efficiencies noted in [Bîrzan et al. \(2004\)](#), where radio data from the literature were used to infer radiative efficiencies. We found a similar trend as in our previous sample, that the most luminous radio objects have the largest cavity powers, and that the ratio of cavity power to the radio power ranges from few to a few thousands. In order to investigate if the radio aging is the source of scatter in the radiative-efficiencies plot, we plotted the ratio of cavity power to bolometric radio luminosity versus the break frequency. This plot shows a segregation between young objects which are in a driving stage and the older (ghost) objects, but no clear trend was present. A similar

segregation is seen when we plot the ratio of cavity energy to radio power versus the break frequency, such that only for few objects is the radiation important (e.g., Cygnus A, M84, M87). As a result, aging does not appear to be the only factor that contributes to the scatter in the radiative-efficiencies plot. The scatter may be due to both radio aging, magnetic field strengths, and intrinsic radio properties such as bolometric radio luminosity because of the interrelation between these factors.

Furthermore, by using both radio and X-ray data we placed limits on the magnetic field strengths and on the particle content in the lobes (the ratio between the heavy-particle energy and the electron energy). We found that the magnetic field strengths required for pressure equilibrium are in general much larger than the equipartition magnetic field strengths and the magnetic field strengths derived by requiring the synchrotron age to be equal to the buoyancy age. Additionally, all of them are larger than the cluster-wide magnetic field ([Carilli & Taylor, 2002](#)). Furthermore, by comparing the equipartition magnetic field strength ( $k = 1, \phi = 1$ ) with the magnetic field strength required for pressure equilibrium, we found that equipartition does not apply in the lobes of the radio sources or there is additional pressure support from other sources. In order for the equipartition magnetic field strength to be equal to the magnetic field strength required for pressure equilibrium, the ratio of heavy-particle energy to the electron energy ( $k$ ) needs to vary between 1 and 35000, a range similar to that found by [Dunn & Fabian \(2004\)](#); [Dunn et al. \(2005\)](#). We found that the range in  $k$  is not due to the variations in magnetic field strengths, but may be due to the

range in intrinsic radio properties, such as the break frequencies. The objects with high values of  $k$  support the idea of heavy jets ([De Young, 2006](#)).

By comparing the synchrotron ages with the buoyancy ages and looking for discrepancies between the two age estimates, we tested the assumptions that went into their derivations. We found that only for Perseus, A1835, and Sersic 159/03 are the two ages similar. The majority of the systems have a buoyancy age a few times larger than the synchrotron age. This discrepancy can be explained if the synchrotron age is a lower limit on the source age ([Eilek, 1996](#)), due to inhomogeneities in the magnetic field strength ([Siah & Wiita, 1990](#); [Wiita & Gopal-Krishna, 1990](#)). Additionally, the X-ray age may be overestimated due to projection effects, drag effects, or if the bubbles are formed at large radii. Also, we found a number of systems which show very short synchrotron ages compared to the buoyancy ages, and we conclude that these systems are in a driving stage with the lobes still being fed by the radio source. For these systems the synchrotron age is a better estimate of the source age than the buoyancy age. Conversely, A262 and A478 have a larger synchrotron age than the buoyancy age, and the buoyancy age may have been underestimated because of projection effects.

Using radio data at 4 different frequencies for most of the systems in our sample, we were able to better classify the cavities as radio-filled cavities, if at least 1.4 GHz radio emission fills the cavities, or ghost, if only low frequency radio emission fills the cavities. Based on the above classification, A133, A478 and MS 0735+074, which in

Bîrzan et al. (2004) and Rafferty et al. (2006) where classified as active, are ghost cavities because no higher frequency (4.5 GHz or 8.5 GHz) emission fills the cavities. Throughout this paper we used the break frequency to classify the cavities as active, intermediate, and ghost. The cavities with break frequencies below 1.4 GHz are classified as ghost, the ones between 1.4 GHz and 5.0 GHz as intermediate, and the ones above 5.0 GHz are active. Based on this classification only M84, M87, Hydra A-inner, Cygnus A, and Centaurus are active cavities. However, we note that since our systems have a continuous range in break frequencies, our separation of the cavities into discrete categories is somewhat arbitrary.

Lastly, by comparing the cavity energy inferred from the X-ray maps with the cavity energy inferred from 1.4 GHz and 327 MHz radio maps, we found that 327 MHz radio emission is a better tracer of the cavity energy (i.e., closer to the energy inferred from X-ray maps). Additionally, 327 MHz radio maps may be useful in finding faint, outer cavities which are not visible in the X-ray images (e.g., RBS 797).

In summary, using an X-ray and radio study of 24 systems with X-ray cavities, we found that these systems are in general poor radiators with a ratio of cavity power to radio power ranging from a few to a few thousands. We conclude that this scatter is probably due to aging plus a combination of intrinsic differences in magnetic field strength and particle content. Our data allow us to put limits on the particle content and, through comparisons of the buoyancy and synchrotron ages, to test the assumptions that go into their determination. We found that the two age

estimates are uncoupled, with no clear correlation between them. We argue that the synchrotron ages are a better estimate for the younger systems (with high break frequencies) which are actively being inflated by the radio source and which generally have a lower value of  $k$ . On the other hand, for the older systems (with low break frequencies), the buoyancy age is likely the better estimate, and  $k$  is generally much higher. A possible interpretation is that these systems have heavier jets (see also [De Young, 2006](#)).

The discovery of X-ray cavities in the hot atmosphere of clusters has made it possible to estimate the radiative efficiencies of the radio sources, which can be much lower than the theoretical estimates (as low as 0.0001). Therefore, most of the AGN's energy in such radio galaxies is dumped directly into the ICM through the X-ray bubbles and shocks, likely preventing the overcooling of gas below  $\sim 2$  keV ([Birzan et al., 2004](#); [Rafferty et al., 2006](#)) which would lead to an over-abundance of extremely bright galaxies at the centers of clusters ([Sijacki & Springel, 2006](#); [Croton et al., 2006](#)).

The large scatter in the radiative efficiencies can be interpreted following [Churazov et al. \(2005\)](#), where they postulated that the elliptical galaxies and the SMBHs are evolving through two stages: the quasar stage with high accretion rates and high radiative efficiency where the SMBH grows rapidly and has a weak feedback on the ICM, and passively evolving elliptical stage with low accretion and radiative efficiency rates, but with a high feedback which keep the gas hot.

# Bibliography

Alexander, P., & Leahy, J. P. 1987, MNRAS, 225, 1

Andernach, H., Schallwich, D., Haslam, C. G. T., & Wielebinski, R. 1981, A&AS, 43, 155

Basson, J. F., & Alexander, P. 2003, MNRAS, 339, 353

Baum, S. A., Zirbel, E. L., & O'Dea, C. P. 1995, ApJ, 451, 88

Becker, R. H., White, R. L., & Edwards, A. L. 1991, ApJS, 75, 1

Begelman, M. C., & Cioffi, D. F. 1989, ApJ, 345, L21

Bender, R., Saglia, R. P., & Gerhard, O. E. 1994, MNRAS, 269, 785

Bennett, A. S. 1962, MmRAS, 68, 163

Benson, A. J., Bower, R. G., Frenk, C. S., Lacey, C. G., Baugh, C. M., & Cole, S. 2003, ApJ, 599, 38

Bicknell, G. V. 1995, ApJS, 101, 29

Bicknell, G. V., Dopita, M. A., & O'Dea, C. P. O. 1997, ApJ, 485, 112

Binney, J., & Tabor, G. 1995, MNRAS, 276, 663

Binney, J., & Tremaine, S. 1987, Galactic Dynamics (Princeton Univ. Press)

- Bîrzan, L., Rafferty, D. A., McNamara, B. R., Wise, M. W., & Nulsen, P. E. J. 2004, ApJ, 607, 800
- Blakeslee, J. P., & Tonry, J. L. 1992, AJ, 103, 1457
- Blandford, R. D., & Rees, M. J. 1974, MNRAS, 169, 395
- Blanton, E. L. 2004, in The Riddle of Cooling Flows in Galaxies and Clusters of galaxies, ed. T. Reiprich, J. Kempner, & N. Soker, 181–188
- Blanton, E. L., Sarazin, C. L., & McNamara, B. R. 2003, ApJ, 585, 227
- Blanton, E. L., Sarazin, C. L., McNamara, B. R., & Wise, M. W. 2001, ApJ, 558, L15
- Blundell, K. M., & Alexander, P. 1994, MNRAS, 267, 241
- Brightenti, F., & Mathews, W. G. 2002a, ApJ, 574, L11
- . 2002b, ApJ, 573, 542
- . 2003, ApJ, 587, 580
- Brüggen, M. 2003, ApJ, 592, 839
- Brüggen, M., & Kaiser, C. R. 2001, MNRAS, 325, 676
- Brüggen, M., Kaiser, C. R., Churazov, E., & Enßlin, T. A. 2002, MNRAS, 331, 545
- Burbidge, G., & Crowne, A. H. 1979, ApJS, 40, 583

- Burbidge, G. R. 1956, ApJ, 124, 416
- Burns, J. O. 1990, AJ, 99, 14
- Burns, J. O., Sulkanen, M. E., Gisler, G. R., & Perley, R. A. 1992, ApJ, 388, L49
- Carilli, C. L., Perley, R. A., Dreher, J. W., & Leahy, J. P. 1991, ApJ, 383, 554
- Carilli, C. L., & Taylor, G. B. 2002, ARA&A, 40, 319
- Carollo, C. M., Danziger, I. J., & Buson, L. 1993, MNRAS, 265, 553
- Carter, D., Inglis, I., Ellis, R. S., Efstathiou, G., & Godwin, J. G. 1985, MNRAS, 212, 471
- Celotti, A., & Fabian, A. C. 1993, MNRAS, 264, 228
- Churazov, E., Brüggen, M., Kaiser, C. R., Böhringer, H., & Forman, W. 2001, ApJ, 554, 261
- Churazov, E., Sazonov, S., Sunyaev, R., Forman, W., Jones, C., & Böhringer, H. 2005, MNRAS, 363, L91
- Churazov, E., Sunyaev, R., Forman, W., & Böhringer, H. 2002, MNRAS, 332, 729
- Ciotti, L., & Ostriker, J. P. 2001, ApJ, 551, 131
- Clarke, T. E., Kronberg, P. P., & Böhringer, H. 2001, ApJ, 547, L111

- Clarke, T. E., Sarazin, C. L., Blanton, E. L., Neumann, D. M., & Kassim, N. E. 2005, ApJ, 625, 748
- Cohen, A. S., Clarke, T. E., Feretti, L., & Kassim, N. E. 2005, ApJ, 620, L5
- Condon, J. J., Cotton, W. D., Greisen, E. W., Yin, Q. F., Perley, R. A., Taylor, G. B., & Broderick, J. J. 1998, AJ, 115, 1693
- Croton, D. J., Springel, V., White, S. D. M., De Lucia, G., Frenk, C. S., Gao, L., Jenkins, A., Kauffmann, G., Navarro, J. F., & Yoshida, N. 2006, MNRAS, 367, 864
- Dalla Vecchia, C., Bower, R. G., Theuns, T., Balogh, M. L., Mazzotta, P., & Frenk, C. S. 2004, MNRAS, 355, 995
- David, L. P., Nulsen, P. E. J., McNamara, B. R., Forman, W., Jones, C., Ponman, T., Robertson, B., & Wise, M. 2001, ApJ, 557, 546
- De Young, D. S. 1993, ApJ, 405, L13
- . 2006, ApJ, 648, 200
- Dreher, J. W., Carilli, C. L., & Perley, R. A. 1987, ApJ, 316, 611
- Dunn, R. J. H., & Fabian, A. C. 2004, MNRAS, 355, 862
- Dunn, R. J. H., Fabian, A. C., & Sanders, J. S. 2006, MNRAS, 366, 758
- Dunn, R. J. H., Fabian, A. C., & Taylor, G. B. 2005, MNRAS, 364, 1343

- Edge, A. C., Wilman, R. J., Johnstone, R. M., Crawford, C. S., Fabian, A. C., & Allen, S. W. 2002, MNRAS, 337, 49
- Edge, D. O., Shakeshaft, J. R., McAdam, W. B., Baldwin, J. E., & Archer, S. 1959, MmRAS, 68, 37
- Eilek, J. 1999, in Diffuse Thermal and Relativistic Plasma in Galaxy Clusters, ed. H. Boehringer, L. Feretti, & P. Schuecker, 71–76
- Eilek, J. A. 1996, in Astronomical Society of the Pacific Conference Series, Vol. 100, Energy Transport in Radio Galaxies and Quasars, ed. P. E. Hardee, A. H. Bridle, & J. A. Zensus, 281–286
- Eilek, J. A., Melrose, D. B., & Walker, M. A. 1997, ApJ, 483, 282
- Ettori, S., Fabian, A. C., Allen, S. W., & Johnstone, R. M. 2002, MNRAS, 331, 635
- Fabian, A. C. 1994, ARA&A, 32, 277
- Fabian, A. C., Celotti, A., Blundell, K. M., Kassim, N. E., & Perley, R. A. 2002, MNRAS, 331, 369
- Fabian, A. C., Mushotzky, R. F., Nulsen, P. E. J., & Peterson, J. R. 2001, MNRAS, 321, L20
- Fabian, A. C., Sanders, J. S., Ettori, S., Taylor, G. B., Allen, S. W., Crawford, C. S., Iwasawa, K., Johnstone, R. M., & Ogle, P. M. 2000, MNRAS, 318, L65

- Fabian, A. C., Sanders, J. S., Taylor, G. B., Allen, S. W., Crawford, C. S., Johnstone, R. M., & Iwasawa, K. 2006, MNRAS, 366, 417
- Fanaroff, B. L., & Riley, J. M. 1974, MNRAS, 167, 31P
- Feretti, L., & Giovannini, G. 2007, ArXiv Astrophysics e-prints
- Feretti, L., Giovannini, G., Klein, U., Mack, K.-H., Sijbring, L. G., & Zech, G. 1998, A&A, 331, 475
- Finoguenov, A., & Jones, C. 2001, ApJ, 547, L107
- Fisher, D., Illingworth, G., & Franx, M. 1995, ApJ, 438, 539
- Forman, W., Churazov, E., Jones, C., Markevitch, M., Nulsen, P., Vikhlinin, A., Begelman, M., Bohringer, H., Eilek, J., Heinz, S., Kraft, R., Owen, F., & Pahre, M. 2006, ArXiv Astrophysics e-prints
- Fujita, Y., Sarazin, C. L., Kempner, J. C., Rudnick, L., Slee, O. B., Roy, A. L., Andernach, H., & Ehle, M. 2002, ApJ, 575, 764
- Ge, J., & Owen, F. N. 1994, AJ, 108, 1523
- Ge, J. P., & Owen, F. N. 1993, AJ, 105, 778
- Ghisellini, G., & Celotti, A. 2001, A&A, 379, L1
- Giovannini, G., Cotton, W. D., Feretti, L., Lara, L., & Venturi, T. 1998, ApJ, 493,

- Gitti, M., Feretti, L., & Schindler, S. 2006, A&A, 448, 853
- Gitti, M., McNamara, B. R., Nulsen, P. E. J., & Wise, M. W. 2007, ApJ, 660, 1118
- Gopal-Krishna, & Wiita, P. J. 2001, A&A, 373, 100
- Gower, J. F. R., Scott, P. F., & Wills, D. 1967, MmRAS, 71, 49
- Gregory, P. C., & Condon, J. J. 1991, ApJS, 75, 1011
- Hales, S. E. G., Mayer, C. J., Warner, P. J., & Baldwin, J. E. 1991, MNRAS, 251, 46
- Haynes, R. F., Huchtmeier, W., Siegman, B., & Wright, A. E. 1975, Compendium of Radio Measurements of Bright Galaxies (CSIRO Publication)
- Heckman, T. M., Illingworth, G. D., Miley, G. K., & van Breugel, W. J. M. 1985, ApJ, 299, 41
- Heinz, S., Brüggen, M., Young, A., & Levesque, E. 2006, MNRAS, 373, L65
- Heinz, S., Choi, Y.-Y., Reynolds, C. S., & Begelman, M. C. 2002, ApJ, 569, L79
- Heinz, S., Merloni, A., & Schwab, J. 2007, ApJ, 658, L9
- Heinz, S., Reynolds, C. S., & Begelman, M. C. 1998, ApJ, 501, 126
- Hines, D. C., Eilek, J. A., & Owen, F. N. 1989, ApJ, 347, 713
- Johnstone, R. M., Allen, S. W., Fabian, A. C., & Sanders, J. S. 2002, MNRAS, 336,

- Jones, T. W., & De Young, D. S. 2005, ApJ, 624, 586
- Kaiser, C. R., & Alexander, P. 1997, MNRAS, 286, 215
- Kardashev, N. S. 1962, Soviet Astronomy, 6, 317
- Katz-Stone, D. M., Rudnick, L., Butenhoff, C., & O'Donoghue, A. A. 1999, ApJ, 516, 716
- Komissarov, S. S., & Gubanov, A. G. 1994, A&A, 285, 27
- Kronberg, P. P., Dufton, Q. W., Li, H., & Colgate, S. A. 2001, ApJ, 560, 178
- Kuehr, H., Witzel, A., Pauliny-Toth, I. I. K., & Nauber, U. 1981, A&AS, 45, 367
- Laing, R. A., & Bridle, A. H. 1987, MNRAS, 228, 557
- Lane, W. M., Clarke, T. E., Taylor, G. B., Perley, R. A., & Kassim, N. E. 2004, AJ, 127, 48
- Lang, K. R. 1999, Astrophysical Formulae, Vol. Volume I (Springer-Verlag Berlin)
- Large, M. I., Cram, L. E., & Burgess, A. M. 1991, The Observatory, 111, 72
- Liu, R., Pooley, G., & Riley, J. M. 1992, MNRAS, 257, 545
- Mack, K.-H., Klein, U., O'Dea, C. P., Willis, A. G., & Saripalli, L. 1998, A&A, 329, 431
- Mazzotta, P., Edge, A. C., & Markevitch, M. 2003, ApJ, 596, 190

- Mazzotta, P., Kaastra, J. S., Paerels, F. B., Ferrigno, C., Colafrancesco, S., Mewe, R., & Forman, W. R. 2002, ApJ, 567, L37
- McNamara, B. R., & Nulsen, P. E. J. 2007, ARAA, 45, 117
- McNamara, B. R., Nulsen, P. E. J., Wise, M. W., Rafferty, D. A., Carilli, C., Sarazin, C. L., & Blanton, E. L. 2005, Nature, 433, 45
- McNamara, B. R., & O'Connell, R. W. 1992, ApJ, 393, 579
- McNamara, B. R., Rafferty, D. A., Bîrzan, L., Steiner, J., Wise, M. W., Nulsen, P. E. J., Carilli, C. L., Ryan, R., & Sharma, M. 2006, ApJ, 648, 164
- McNamara, B. R., Wise, M., Nulsen, P. E. J., David, L. P., Sarazin, C. L., Bautz, M., Markevitch, M., Vikhlinin, A., Forman, W. R., Jones, C., & Harris, D. E. 2000, ApJ, 534, L135
- McNamara, B. R., Wise, M. W., Nulsen, P. E. J., David, L. P., Carilli, C. L., Sarazin, C. L., O'Dea, C. P., Houck, J., Donahue, M., Baum, S., Voit, M., O'Connell, R. W., & Koekemoer, A. 2001, ApJ, 562, L149
- Meier, D. L. 1999, ApJ, 522, 753
- Molendi, S., & Pizzolato, F. 2001, ApJ, 560, 194
- Murgia, M., Fanti, C., Fanti, R., Gregorini, L., Klein, U., Mack, K.-H., & Vigotti, M. 1999, A&A, 345, 769

Myers, S. T., & Spangler, S. R. 1985, ApJ, 291, 52

Nipoti, C., & Binney, J. 2005, MNRAS, 361, 428

Nulsen, P. E. J., David, L. P., McNamara, B. R., Jones, C., Forman, W. R., & Wise, M. 2002, ApJ, 568, 163

Nulsen, P. E. J., Hambrick, D. C., McNamara, B. R., Rafferty, D., Birzan, L., Wise, M. W., & David, L. P. 2005a, ApJ, 625, L9

Nulsen, P. E. J., McNamara, B. R., Wise, M. W., & David, L. P. 2005b, ApJ, 628, 629

Omma, H., Binney, J., Bryan, G., & Slyz, A. 2004, MNRAS, 348, 1105

Owen, F. N., Eilek, J. A., & Kassim, N. E. 2000, ApJ, 543, 611

Owen, F. N., Eilek, J. A., & Keel, W. C. 1990, ApJ, 362, 449

Pacholczyk, A. G. 1970, Radio Astrophysics, Nonthermal Processes in Galactic and Extragalactic Sources (W. H. Freeman and Company)

Parma, P., de Ruiter, H. R., Fanti, C., & Fanti, R. 1986, A&AS, 64, 135

Pauliny-Toth, I. I. K., Wade, C. M., & Heeschen, D. S. 1966, ApJS, 13, 65

Pedlar, A., Ghataure, H. S., Davies, R. D., Harrison, B. A., Perley, R., Crane, P. C., & Unger, S. W. 1990, MNRAS, 246, 477

- Peterson, J. R., & Fabian, A. C. 2006, Phys. Rep., 427, 1
- Peterson, J. R., Kahn, S. M., Paerels, F. B. S., Kaastra, J. S., Tamura, T., Bleeker, J. A. M., Ferrigno, C., & Jernigan, J. G. 2003, ApJ, 590, 207
- Peterson, J. R., Paerels, F. B. S., Kaastra, J. S., Arnaud, M., Reiprich, T. H., Fabian, A. C., Mushotzky, R. F., Jernigan, J. G., & Sakelliou, I. 2001, A&A, 365, L104
- Pilkington, J. D. H., & Scott, P. F. 1965, MmRAS, 69, 183
- Pizzolato, F., & Soker, N. 2005, ApJ, 632, 821
- . 2006, MNRAS, 371, 1835
- Pollack, L. K., Taylor, G. B., & Allen, S. W. 2005, MNRAS, 359, 1229
- Quilis, V., Bower, R. G., & Balogh, M. L. 2001, MNRAS, 328, 1091
- Rafferty, D. A., McNamara, B. R., Nulsen, P. E. J., & Wise, M. W. 2006, ApJ, 652, 216
- Reich, W., Fürst, E., Reich, P., Kothes, R., Brinkmann, W., & Siebert, J. 2000, A&A, 363, 141
- Reiprich, T., Kempner, J., & Soker, N., eds. 2003, The Riddle of Cooling Flows in Galaxies and Clusters of Galaxies
- Reynolds, C. S., Fabian, A. C., Celotti, A., & Rees, M. J. 1996, MNRAS, 283, 873

- Reynolds, C. S., Heinz, S., & Begelman, M. C. 2002, MNRAS, 332, 271
- Reynolds, C. S., McKernan, B., Fabian, A. C., Stone, J. M., & Vernaleo, J. C. 2005, MNRAS, 357, 242
- Robinson, K., Dursi, L. J., Ricker, P. M., Rosner, R., Calder, A. C., Zingale, M., Truran, J. W., Linde, T., Caceres, A., Fryxell, B., Olson, K., Riley, K., Siegel, A., & Vladimirova, N. 2004, ApJ, 601, 621
- Rodríguez-Martínez, M., Velázquez, P. F., Binette, L., & Raga, A. C. 2006, A&A, 448, 15
- Rossi, P., Bodo, G., Massaglia, S., Ferrari, A., & Mignone, A. 2004, Ap&SS, 293, 149
- Rudnick, L. 2002, New Astronomy Review, 46, 95
- Ruszkowski, M., & Begelman, M. C. 2002, ApJ, 581, 223
- Ruszkowski, M., Brüggen, M., & Begelman, M. C. 2004, ApJ, 615, 675
- Rybicki, G. B., & Lightman, A. P. 1979, Radiative Processes in Astrophysics (John Wiley and Sons, Inc.)
- Sadler, E. M. 1984, AJ, 89, 53
- Sanders, J. S., & Fabian, A. C. 2002, MNRAS, 331, 273
- . 2006, ArXiv Astrophysics e-prints

Sarazin, C. L. 1988, X-ray Emission from clusters of Galaxies (Cambridge University Press)

Sarazin, C. L. 2003, Physics of Plasmas, 10, 1992

Sarazin, C. L., Baum, S. A., & O'Dea, C. P. 1995a, ApJ, 451, 125

Sarazin, C. L., Burns, J. O., Roettiger, K., & McNamara, B. R. 1995b, ApJ, 447, 559

Scheuer, P. A. G. 1974, MNRAS, 166, 513

Scheuer, P. A. G., & Williams, P. J. S. 1968, ARA&A, 6, 321

Schindler, S., Castillo-Morales, A., De Filippis, E., Schwope, A., & Wambsganss, J. 2001, A&A, 376, L27

Siah, M. J., & Wiita, P. J. 1990, ApJ, 363, 411

Sijacki, D., & Springel, V. 2006, MNRAS, 366, 397

Slee, O. B. 1995, Australian Journal of Physics, 48, 143

Slee, O. B., Roy, A. L., Murgia, M., Andernach, H., & Ehle, M. 2001, AJ, 122, 1172

Slee, O. B., & Siegman, B. C. 1988, MNRAS, 235, 1313

Smith, D. A., Wilson, A. S., Arnaud, K. A., Terashima, Y., & Young, A. J. 2002, ApJ, 565, 195

Smith, E. P., Heckman, T. M., & Illingworth, G. D. 1990, ApJ, 356, 399

- Soker, N. 2006, New Astronomy, 12, 38
- Soker, N., & Pizzolato, F. 2005, ApJ, 622, 847
- Soker, N., White, III, R. E., David, L. P., & McNamara, B. R. 2001, ApJ, 549, 832
- Spinrad, H., Marr, J., Aguilar, L., & Djorgovski, S. 1985, PASP, 97, 932
- Spitzer, J. L. 1978, Physical Processes in the Interstellar Medium (New York: Wiley-Interscience)
- Sun, M., Jones, C., Murray, S. S., Allen, S. W., Fabian, A. C., & Edge, A. C. 2003, ApJ, 587, 619
- Tabor, G., & Binney, J. 1993, MNRAS, 263, 323
- Taylor, G. B., Barton, E. J., & Ge, J. 1994, AJ, 107, 1942
- Taylor, G. B., Fabian, A. C., & Allen, S. W. 2002, MNRAS, 334, 769
- Taylor, G. B., & Perley, R. A. 1993, ApJ, 416, 554
- Taylor, G. B., Perley, R. A., Inoue, M., Kato, T., Tabara, H., & Aizu, K. 1990, ApJ, 360, 41
- Taylor, G. B., Sanders, J. S., Fabian, A. C., & Allen, S. W. 2006, MNRAS, 365, 705
- Tonry, J. L. 1985, AJ, 90, 2431
- Tribble, P. C. 1993, MNRAS, 261, 57

Valtonen, M. J., & Heinämäki, P. 2000, ApJ, 530, 107

van Breugel, W., Heckman, T., & Miley, G. 1984, ApJ, 276, 79

van der Laan, H., & Perola, G. C. 1969, A&A, 3, 468

Vernaleo, J. C., & Reynolds, C. S. 2006, ApJ, 645, 83

Verschuur, G. L., & Kellermann, K. I., eds. 1974, Galactic and Extragalactic Radio Astronomy (Springer-Verlag New York Inc.)

Vogt, C., & Enßlin, T. A. 2003, A&A, 412, 373

Voigt, L. M., & Fabian, A. C. 2004, MNRAS, 347, 1130

Vollmer, B., Davoust, E., Dubois, P., Genova, F., Ochsenbein, F., & van Driel, W. 2005, A&A, 431, 1177

Vrtilek, J. M., Grego, L., David, L. P., Ponman, T. J., Forman, W., Jones, C., & Harris, D. E. 2002, APS Meeting Abstracts, 17107

Waldram, E. M., Yates, J. A., Riley, J. M., & Warner, P. J. 1996, MNRAS, 282, 779

Wall, J. V., & Peacock, J. A. 1985, MNRAS, 216, 173

White, R. L., & Becker, R. H. 1992, ApJS, 79, 331

Wiita, P. J., & Gopal-Krishna. 1990, ApJ, 353, 476

- Wise, M. W., McNamara, B. R., Nulsen, P. E. J., Houck, J. C., & David, L. P. 2007,  
ApJ, 659, 1153
- Wold, M., Lacy, M., & Armus, L. 2005, in Growing Black Holes: Accretion in a  
Cosmological Context, ed. A. Merloni, S. Nayakshin, & R. A. Sunyaev, 401–402
- Wright, A., & Otrupcek, R. 1990, in PKS Catalog (1990)
- Wright, A. E., Griffith, M. R., Burke, B. F., & Ekers, R. D. 1994, ApJS, 91, 111
- Wright, A. E., Griffith, M. R., Hunt, A. J., Troup, E., Burke, B. F., & Ekers, R. D.  
1996, ApJS, 103, 145
- Young, A. 2004, PhD thesis, AA(UNIVERSITY OF MINNESOTA)
- Young, A. J., Wilson, A. S., & Mundell, C. G. 2002, ApJ, 579, 560
- Zakamska, N. L., & Narayan, R. 2003, ApJ, 582, 162
- Zhao, J.-H., Sumi, D. M., Burns, J. O., & Duric, N. 1993, ApJ, 416, 51

## APPENDIX A

# Details of Radio Observations and Image Properties

Table A.1 lists the details of our observations for each object in the sample. Table A.2 lists the basic radio image properties such as resolution, noise, position angle for the beam at each frequency, and the arrays from which data were used to make the image. Also listed are the references to published images.

Table A.1. Summary of radio observations

Name	Frequency <sup>a</sup> (MHz)	BW (MHz)	Array	Date	Duration <sup>b</sup> (hh:mm:ss)	Flux calibrator	Phase calibrator
A133	327.5/333	3.125	A	30 November 1992	00:68:00	3C48	0023-263
	328.5/321.56	6.25	AB	9 June 2002	02:19:53	3C48	0116-208
	1464.9/1385.1	50	A	25 June 1998	02:31:10	3C286/3C48	036-216
	1364.9/1435.1	25	C	9 December 2002	03:08:10	3C48	0116-208
	1364.9/1435.1	25	BC	29 September 2002	01:07:40	3C48	0116-208
	1364.9/1435.1	25	BC	6/7 October 2001	00:57:40	3C48	0116-208
	4885.1/4835.1	50	DC	28 October 1989	00:11:10	3C48	0036-216
	8085/8335	50	D	3 August 1988	00:38:20	3C48	2234+282
	8535/8785	50	D	3 August 1988	00:37:00	3C48	2234+282
	327.5/321.56*	3.125	A	13 March 2006	04:23:40	3C48	3C48
Perseus	1515.9/1365.1*	25	B	14 May 2005	02:13:40	3C48	0119+321
	8535.1/8485.1*	50	B	14 May 2005	01:38:50	3C48	0205-322
	327.5	3.125	C	21 November 1998	00:41:50	3C48/3C147/3C286	3C48/3C147/3C286
	327.5	3.125	A	15 August 2003	10:28:30	3C48/3C147	3C48/3C147
	327.5	3.125	B	23 November 2003	08:23:10	3C48/3C147	3C48/3C147
	1514.9/1635.1	50	A	8 October 1983	01:53:30	3C48	3C138
	1380/1706	25/6.25	A	8 October 1983	01:42:20	3C48	3C138
	1635.1/1514.9	50	A	8 October 1983	01:47:00	3C48	3C138
	1706/1380	6.25/25	A	8 October 1983	02:00:20	3C48	3C138
	1514.9/1635.1	50	C	16 April 1984	01:37:00	3C48	3C138
A262	1380/1706	25/6.25	C	16 April 1984	01:37:00	3C48	3C138
	1635.1/1514.9	50	C	16 April 1984	01:30:30	3C48	3C138
	1706/1380	6.25/25	C	16 April 1984	01:33:00	3C48	3C138
	1385.1/1385.1	50	B	25 February 2000	12:44:50	3C48	0303+47/0313+41
	4635/4735	50	A	26 April 1986	00:26:50	3C286	1232+119
	4835/4935	50	A	26 April 1986	00:03:50	3C286	1252+119
	4685/4885	25	D	21 August 1988	03:00:00	3C48	3C138
	4585/4755	25	D	21 August 1988	03:16:50	3C48	3C138
	8414.9/8414.9	50	BC	1 July 1997	00:25:50	3C48/3C286	0954+658
	327.5/321.56*	3.125	B	6 August 2006	01:39:40	3C48	0323+055
A478	1464.9/1514.9	50	C	14/15 March 1992	02:38:00	3C48/0518+165	0319+121
	4885.1/4835.1	50	D	14 July 1992	02:36:30	3C48/0518+165	0319+121
	8414.9/8464.9	50	C	14/15 March 1992	01:19:30	3C48/0518+165	0319+121
	327.1/321.56*	3.125	A+PT	23 November 2004	02:38:50	3C48	0318+164
MS 0735.6+7421	1515.9/1365.1*	25	A	16 November 2004	03:09:20	3C48	0409+122
	8435.1/8485.1*	50	B	14 May 2005	01:46:00	3C48	0449+113
	327.5/321.56*	3.125	A+PT	24 October 2004	02:13:10	3C286	0749+743

Table A.1 (continued)

Name	Frequency <sup>a</sup> (MHz)	BW (MHz)	Array	Date	Duration <sup>b</sup> (hh:mm:ss)	Flux calibrator	Phase calibrator
Hydra A	1464.9/1385.1	12.5	C	15 April 2004	03:13:40	3C147	0841+708
	8435.1/8485.1*	50	D	28 November 2005	04:24:00	3C147	0721+713
	1415/1430	12.5	BC	1 October 1989	01:17:30	3C286	0859-140/0735+178
	1515/1530	12.5	BC	1 October 1989	01:17:20	3C286	0859-140/0735+178
	1415/1430	12.5	BC	29 August 1989	01:20:30	3C286	0859-140/0851+202
	1515/1530	12.5	BC	29 August 1989	01:19:40	3C286	0859-140/0851+202
	1464.9/1514.9	50	D	14 August 1988	00:28:20	3C48/3C286	0859-140
	1415/1430	12.5	BC	3 August 1989	01:21:20	3C286	0859-140/0735+178
	1515/1530	12.5	BC	3 August 1989	01:15:20	3C286	0859-140/0735+178
	4635/4885	25	A	11 January 1989	03:12:59	3C286	0859-140
RBS 797	4635.1/4885.1	50	D	14 August 1988	00:28:10	3C48/3C286	0859-140/0851+202
	4635.1/4885.1	50	B	20 December 1987	02:59:37	3C286	0859-140/0851+202
	4635/4885	12.5	AB	29 October 1987	02:19:40	3C286	0859-140/0851+202
	4635/4885	12.5	A	8 October 1987	02:47:20	3C286	0859-140/0851+202
	7815/8165	12.5	A	12/13 April 1990	01:37:37	3C286	0859-140/0851+202
	8515/8885	12.5	A	12/13 April 1990	01:50:12	3C286	0859-140/0851+202
	7815/8165	12.5	A	14 March 1990	02:05:19	3C286	0859-140/0851+202
	8515/8885	12.5	A	14 March 1990	01:57:05	3C286	0859-140/0851+202
	7814.9/8164.9	50	D	21 December 1989	01:13:02	3C286	0859-140/0851+202
	8514.9/8885.1	50	D	21 December 1989	01:14:46	3C286	0859-140/0851+202
Zw 2701	7815/8165	25	C	15 August 1989	02:16:09	3C286	0859-140/0851+202
	8515/8885	25	C	15 August 1989	02:09:22	3C286	0859-140/0851+202
	7815/8165	25	C	28 August 1989	01:58:39	3C286	0859-140/0851+202
	8515/8885	25	C	28 August 1989	01:53:21	3C286	0859-140/0851+202
	7815/8165	25	B	30 April 1989	03:09:40	3C286	0859-140/0851+202
	8515/8885	25	B	30 April 1989	03:10:30	3C286	0859-140/0851+202
	8785.1/8435.1	50	D	14 August 1988	00:47:50	3C48/3C386	0859-140
	327.5/321.56*	2.246	A	23 November 2004	02:32:30	3C147	1459+716
	1514.9/1435.1	50	A	27 March 2002	04:14:10	3C286	1044+809/0713+438
	1514.9/1435.1	50	B	27 July 2002	06:10:20	3C286	1044+809/0713+438
Zw 3146	4885.1/4835.1*	50	B	3 May 2005	05:05:54	3C147	1044+809/0713+438
	8435.1/8485.1	50	CD	25 September 2001	04:59:20	3C286	1044+809/0713+438
	8435.1/8485.1*	50	B	3 May 2005	00:20:20	3C147	1044+809
	327.5/321.56*	3.125	B	6 August 2006	01:36:30	3C147	0834+555
	4885.1/4835.1*	50	C	18 December 2006	01:39:30	3C147/3C286	1035+564
	8435.1/8485.1*	50	D	28 November 2005	01:37:40	3C147/3C286	0958+474
	327.5/321.56*	3.125	B	6 August 2006	01:43:10		1021+219

Table A.1 (continued)

Name	Frequency <sup>a</sup> (MHz)	BW (MHz)	Array	Date	Duration <sup>b</sup> (hh:mm:ss)	Flux calibrator	Phase calibrator
M84	4885.1/4835.1*	50	C	18 December 2006	04:28:30	3C147/3C286	1024+008
	8435.1/8485.1*	50	C	18 December 2006	01:40:50	3C147	1024+008
	327.5/321.5*	3.125	A	21 November 2004	01:39:30	3C286	1330+251
	1464.9/1385.1	50	B	9 February 2000	00:30:30	3C286	1252+119
	4885.1/4835.1	50	C	4 June 2000	02:20:10	3C286	1236+119
	8435.1/8485.1	50	D	15 April 1999	00:33:30	3C286	1252+119
	327.5/321.5*	3.125	A	21 November 2004	01:39:30	3C286	1330+251
	1364.8/1435	3.125	B	5 February 2000	09:08:20	3C286	1347+122
	4885.1/4835.1	50	CD	18 June 1988	01:47:00	3C286	1221+282
	8085/8335	50	B	29/30 April 1989	01:37:10	3C286	1222+037
M87	8535/8785	50	B	29/30 April 1989	01:42:50	3C286	1222+037
	8085/8335	50	BC	27 June 1989	01:35:20	3C286	1222+037
	8535/8785	50	BC	27 June 1989	01:32:30	3C286	1222+037
	8085.1/8335.1	50	D	12 January 1990	00:59:10	3C286	1345+125
	8535.1/8785.1	50	D	12 January 1990	01:01:10	3C286	
	8085.1/8335.1	50	A	25 April 1990	04:48:30	3C286	0923+392/1226+023/1222+037
	8535.1/8785.1	50	A	25 April 1990	03:48:20	3C286	0923+392/1226+023/1222+037
	8085.1/8335.1	50	B	20 July 1990	02:20:20	3C286	0923+392/1226+023/1222+037
	8535.1/8785.1	50	B	20 July 1990	02:50:20	3C286	0923+392/1226+023/1222+037
	327.5	2.246	A	1 May, 5 May 2002	02:00:13	3C286	0923+392/1226+023/1222+037
Centaurus	1465/1665	25	AB	19 June 1998	01:20:00	3C286	1316-336/1407+284
	1465/1665	25	A	23 April 1993	00:20:05	3C286	1316-336
	4635.1/4885.1	50	AB	19 June 1998	01:15:10	3C286	1316-336/1407+284
	4635.1/4885.1	50	BC	6 November 1998	00:41:00	3C286	1316-336/1407+284
	4635.1/4885.1	50	A	23 April 1993	00:08:05	3C286	1316-336
	8114.9/8485.1	50	AB	19 June 1998	00:54:40	3C286	1316-336/1407+284
	8114.9/8485.1	50	BC	6 November 1998	00:41:35	3C286	1316-336/1407+284
	327.5/321.56*	3.125	B	6 August 2006	05:22:50	3C48/3C147/3C286	1308-098
	1464.9/1385.1	50	BC	16 June 2001	03:20:50	3C286	1246-075
	1515.9/1365.1*	25	C	31 July 2004	04:20:20	3C286	1248-199
HCG 62	8435.1/8485.1*	50	D	12 December 2005	00:47:30	3C286	1246-075
	327.5	2.246	A	23 April, 1 May, 5 May 2002	02:05:54	3C286	3C286
	1464.9	50	A	18 June 1989	02:54:10	3C 286	3C286
	8085/8335	50	CD	15 April 1988	00:44:20	3C286	1142+101
	8535/8785	50	A	8, 10, 11 October 1988	02:20:40	3C286	1055+018
	8535/8785	50	A	14, 15 October 1988	00:50:10	3C286	1055+018
	8535/8785	50	A	22 October 1988	13:14:00	3C286	1055+018/1413+135

Table A.1 (continued)

Name	Frequency <sup>a</sup> (MHz)	BW (MHz)	Array	Date	Duration <sup>b</sup> (hh:mm:ss)	Flux calibrator	Phase calibrator
A1835	327.5	3.125	A	23 April 2002	02:19:52	3C286	3C286
	1464.9/1385.1	50	A	12 April 1998	00:18:30	3C286	1354-021
	1465/1665	25	A	25 April 1998	01:50:30	3C286	1354-021
	1364.9/1435.1	25	B	13/14 July 1998	07:22:15	3C286	1354-021
	4635.1/4885.1	50	A	23 April 1998	00:26:25	3C286	1354-021
	4635.1/4885.1	50	B	31 August 1998	00:20:20	3C286	1354-021
	8435.1/8485.1	50	A	23 February 1998	00:09:00	3C286	1354-021
	8435.1/8485.1	50	A	12 April 1998	00:14:40	3C286	1354-021
	8114.9/8485.1	50	BA	18/19 June 1998	00:24:30	3C286	1354-021
	8114.9/8485.1	50	B	31 August 1998	00:20:10	3C286	1354-021
MACS J1423.8+2404	8114.9/8485.1	50	C	22 January 1999	00:20:20	3C286	1354-021
	8435.1/8485.1	50	C	13 August 2001	02:05:40	3C286	1354-021
	8435.1/8485.1	50	C	17 September 2001	02:05:40	3C286	1354-021
	8435.1/8485.1	50	D	17 November 2001	02:53:10	3C286	1354-021
	327.5/321.56*	3.125	A+PT	17 March 2006	03:24:40	3C286	1330+251
	1464.9/1385.1*	25	A	16/17 March 2006	01:38:50	3C286	1407+284
	327.5/333	3.125	A	1 December 1988	02:58:20	3C286	1416+067
	1464.9/1514.9	50	A	30 November 1988	02:55:00	3C286	1502+106
	1464.9/1514.9	50	B	30 March 1989	02:03:30	3C286	1502+106
	4885.1/4835.1	50	B	30 March 1989	02:20:00	3C286	1502+106
MKW 3S	4885.1/4835.1	50	C	26 June 1989	02:32:50	3C286	1502+106
	8085/8335	50	CD	15 April 1988	00:41:50	3C286	1442+101
	8535/8785	50	D	30 November 1988	00:42:30	3C286	1606+106
	8535/8785	50	B	27 April 1989	03:18:30	3C286	1502+106
	327.5/321.56	3.125	A	29 October 2000	09:26:00	3C286	1419+064
	1464.9/1414.9	25/50	C	2/3 August 2001	00:52:20	3C286	1445+099
	1314.9/1485.9	25	C	6 August 2001	00:24:00	3C286	1445+099
	1464.9/1464.9	25/50	B	17 May 2001	02:01:10	3C286	1504+104
	4885.1/4835.1	50	C	2/3 August 2001	03:19:10	3C286	1504+104
	4885.1/4835.1	50	C	6 August 2001	01:33:00	3C286	1504+104
A2199	4885.1/4835.1	50	C	9/10 August 2001	02:24:50	3C286	1504+104
	8435.1/8485.1*	50	D	28 November 2005	04:24:00	3C286	1504+104
	327.5/321.56*	3.125	A+PT	17 March 2006	01:38:40	3C286	3C286
	1464.9/1385.1	50	A	2 April 1994	00:40:00	3C286	1633+382
	1464.9/1514.9	50	A	2 January 1993	00:57:00	3C286	1656+477
	4685/4885	50	D	4 July 1988	00:36:30	3C286	1656+477
	4585/4785	50	D	12 September 1988	00:73:58	3C286	

Table A.1 (continued)

Name	Frequency <sup>a</sup> (MHz)	BW (MHz)	Array	Date	Duration <sup>b</sup> (hh:mm:ss)	Flux calibrator	Phase calibrator
Cygnus A	4685/4885	50	B	3 April 1989	03:30:24	3C286	1656+477
	4685/4885	50	C	22 July 1989	01:32:12	3C286	1656+477
	8414.9/8464.9	50	A	24 August 1991	00:13:20	3C286	1624+416
	8414.9/8464.9	50	C	17 November 1994	03:35:20	3C286	1611+343/1739+522
	8414.9/8464.9	50	A	11/12 September 1995	03:44:10	3C286	1611+343
	327.5/333	3.125	B	2 December 1998	03:48:10	3C48	1635+38
	327.5/333	3.125	B	3 September 1986	01:18:50	3C286/3C48	3C286/3C48
	327.5/333	3.125	C	5 September 1986	01:03:50	3C286/3C48	3C286/3C48
	327.5/333	3.125	C	1 December 1986	00:44:40	3C286/3C48	3C286/3C48
	327.5/333	3.125	A	18 August 1987	02:27:50	3C286/3C48	3C286/3C48
	327.5/333	3.125	A	31 August 1987	02:51:20	3C286/3C48	3C286/3C48
	1704/1345	3.125/6.25	B	3 September 1986	03:30:10	3C286/3C48/3C138	2050+364
	1704/1345	3.125/6.25	B	5 September 1986	03:11:20	3C286/3C48/3C138	2050+364
	1704/1345	3.125/6.25	C	1 December 1986	02:23:20	3C286/3C48/3C138	2050+364
	1704/1345	3.125/6.25	A	18 August 1987	02:52:10	3C286/3C48/3C138	2050+364
	1704/1345	3.125/6.25	A	31 August 1987	03:44:10	3C286/3C48/3C138	2050+364
	4995.2/4525	12.5	B	14/23 January 1984	07:45:10	3C286/3C48/3C138	2050+403
	4995.2/4525	25	C	15 April 1984	02:18:10	3C286/3C48/3C138	2050+403
	4995.2/4525	25	D	28 August 1984	00:36:30	3C286	2005+403
	8435.1/8485.1	50	D	29 June 1996	00:24:00	0521+166	2340+266/2330+110/2323-032
	7815/8165	25	BC	27 June 1998	03:15:00	3C286/3C48	2005+403
	8515/8885	25	BC	27 June 1998	03:22:10	3C286/3C48	2005+403
Sersic 159/03	327.5/321.56*	3.125	A	6 March 2006	02:32:20	3C48	0025-260
	1464.9/1385.1*	50	B	8 August 2006	01:40:20	3C48	2302-373
	4885.1/4835.1*	50	D	27 November 2005	00:46:50	3C48	2314-449
	8435.1/8485.1*	50	B	8 August 2006	01:42:20	3C48	2314-449
A2597	1364.9/1435.1	50	A	8 October 2004	06:41:55	3C48	2246-121
	4985.1/4985.1	50	A	7 December 1996	01:10:50	3C286	2246-121
	8414.9/8464.9	50	A	30 November 1992	00:13:40	3C286	2329-162
A4059	328.5/321.56	6.25	AB	9 June 2002	02:31:46	3C48	2341-351
	1515.9/1365.1	25	A	24 November 2004	02:16:10	3C48	2314-316
	4885.1/4835.1	50	AB	7 February 1993	00:28:20	3C48	2337-334/0039+230/0518+165
	7814.9/8164.9	50	A	15 November 1992	02:24:00	3C286	2337-334
	8514.9/8885.1	50	A	15 November 1992	02:26:00	3C48	2337-334/0518+165
	7814.9/8164.9	50	AB	7 February 1993	00:56:00	3C48	2337-334/0518+165
	8514.9/8885.1	50	AB	7 February 1993	00:55:50	3C48	2337-334/0518+165

<sup>a</sup>Our observations are marked with \*<sup>b</sup>The integration time on source

Table A.2. Radio image properties

Name	Frequency (MHz)	Array	Resolution (arcsec $\times$ arcsec)	PA (degree)	Rms noise (mJy/beam)	References
A133	330.25	A	10.3 $\times$ 6.6	12.6	1.7	...
	321.56	AB	34.4 $\times$ 18.5	-23.1	2.0	...
	1425	A	3.5 $\times$ 2.3	65.1	0.046	21
	1400	A, BC, C	20.3 $\times$ 12.4	-0.7	0.060	14
	4860.1	DC	12.0 $\times$ 7.9	73.9	0.034	...
	8660	D	18.8 $\times$ 6.9	-27.8	0.033	...
	324.531	A	6.4 $\times$ 5.5	-29.8	0.55	...
	1365.1	B	4.3 $\times$ 3.5	-48.6	0.045	17
	8460.1	B	0.7 $\times$ 0.6	49.2	0.021	...
	327.5	A, B, C	8.6 $\times$ 7.6	-83.8	7.6	6
Perseus	1575	A, B, C	8.1 $\times$ 4.4	86.5	3.0	6, 18
	4785	A, D	4.1 $\times$ 4.1	46.5	10.0	8
	8414.9	BC	2.0 $\times$ 1.2	82.6	15.0	...
	324.531	B	21.7 $\times$ 16.4	-37.4	3.7	...
	1489.9	C	14.3 $\times$ 13.8	-47.7	0.050	20
2A 0335+096	4860.1	D	15.7 $\times$ 13.9	6.7	0.008	20
	8439.9	C	4.7 $\times$ 4.7	-45.0	0.025	20
	324.482	A+PT	5.7 $\times$ 4.2	20.2	5.3	...
	1440.5	A	1.2 $\times$ 1.1	-1.7	0.038	22
	8460.1	B	0.7 $\times$ 0.6	89.1	0.025	...
A478	324.531	A+PT	7.6 $\times$ 5.7	-43.3	1.1	4
	1425	C	18.3 $\times$ 12.0	-56.5	0.036	4, 15
	8460.1	D	7.6 $\times$ 5.8	-10.4	0.015	...
	73.788 <sup>a</sup>	A	31.9 $\times$ 23.7	6.4	39	13
	332.9 <sup>a</sup>	A, B, C	15.7 $\times$ 13.9	-21.9	5.0	13
MS 0735.6+7421	1442.5	BC	16.5 $\times$ 9.0	-22.4	17	13
	1489.9	D	65.1 $\times$ 46.1	-13.3	25	13, 23
	4760.1	A, AB, B, D	0.5 $\times$ 0.4	-2.8	0.25	23

Table A.2 (continued)

Name	Frequency (MHz)	Array	Resolution (arcsec × arcsec)	PA (degree)	Rms noise (mJy/beam)	References
RBS 797	8610.1	A, B, C, D	0.8 × 0.6	-5.4	0.48	...
	324.482	A	7.8 × 5.6	18.4	0.87	...
	1435	A	1.5 × 1.1	-15.6	0.025	10
	1400	B	4.9 × 3.5	5.1	0.025	10
	4860.1	B	1.3 × 1.0	-19.2	0.02	10
Zw 2701	8460.1	CD	5.8 × 3.5	-19.1	0.013	10
	8460.1	B	0.9 × 0.6	46.7	0.032	...
	324.531	B	27.2 × 21.3	-68.9	2.9	...
	4860.1	C	4.5 × 3.0	60.6	0.026	...
	8460.1	D	7.3 × 5.7	-40.8	0.02	...
Zw 3146	324.531	B	31.5 × 17.1	-46.3	3.1	...
	4860.1	C	3.9 × 3.6	87.8	0.018	...
	8460.1	C	2.3 × 2.1	58.1	0.017	...
	324.482	A	6.2 × 5.7	-26.7	8.4	...
	1385.1	B	4.2 × 4.1	-12.7	0.65	12
M84	4860.1	C	4.2 × 3.8	-87.1	0.11	12
	8460.1	D	7.4 × 7.2	-13.2	0.16	...
	324.482	A	6.3 × 5.7	-26.9	21	16
	1398.595	B	4.6 × 4.3	-85.7	5.0	...
	4685	CD	2.1 × 2.0	87.0	1.2	11
Centaurus	8210.1	A, B, BC, D	2.7 × 2.2	-44.5	5.0	...
	327.5	A	38.7 × 8.0	-13.8	5.6	...
	1565	A, AB	4.4 × 2.4	-1.7	0.47	25, 26
	4760.1	A, AB, BC	1.9 × 1.1	15.4	0.13	25, 26
	8300	AB, BC	1.3 × 0.7	18.2	0.11	25, 26
HCG 62	324.531	B	30.9 × 17.4	-36.2	3.0	...
	1440.5	BC, C	13.2 × 9.3	-78.4	0.095	...
	8460.1	D	8.0 × 6.9	-10.5	0.016	...

Table A.2 (continued)

Name	Frequency (MHz)	Array	Resolution (arcsec × arcsec)	PA (degree)	Rms noise (mJy/beam)	References
A1795	327.5	A	9.0 × 8.4	26.6	7.5	...
	1464.9	A	1.2 × 1.1	42.0	0.070	17, 27
A1835	8210	A, CD	0.20 × 0.18	-84.6	0.013	7
	327.5	A	9.9 × 9.0	-12.1	2.5	...
A1425	1425	A	1.3 × 1.3	-16.3	0.032	...
	1400	B	5.1 × 4.4	-67.5	0.021	...
MACS J1423.8+2404	4670.1	A, B	0.50 × 0.50	-37.9	0.034	...
	8460.1	A, BA, B, C, D A+PT	0.86 × 0.63	-31.1	0.024	...
A2052	324.531	A	5.7 × 4.8	-1.9	0.87	...
	1425	A	1.9 × 1.4	-66.8	0.042	...
MKW 3S	330.25	A	6.2 × 5.3	-56.1	7.6	14, 28
	1489.9	A, B	1.5 × 1.3	-55.0	0.30	28
A2199	4860.1	B, C	1.5 × 1.4	-62.8	0.10	1, 28
	8660	B, CD, D	0.9 × 0.7	-30.8	0.52	8
Cyg A	324.464	A	7.5 × 6.6	-76.5	1.2	29
	1439.9	B, C	4.4 × 4.2	-15.1	0.041	...
Cyg A	4860.1	C	4.1 × 3.6	88.0	0.016	...
	8460.1	D	7.1 × 6.4	-81.4	0.013	...
Sersic A	324.531	A+PT	5.9 × 4.8	-18.0	4.5	...
	1489.9	A	1.2 × 1.1	52.9	0.28	9, 17
Cyg A	4675	B, C, D	1.2 × 1.1	82.7	0.038	8, 9
	8414.9	A, C	0.8 × 0.7	-78.5	0.05	9
Sersic 159/03	330.25	A, B, C	13.4 × 10.2	86.9	6.0	2
	1524.5	A, B, C	2.8 × 2.7	-59.4	48	2, 5
Sersic 159/03	4760.1	B, C, D	1.5 × 1.4	89.3	12	2, 5
	7990	BC, D	2.3 × 2.0	-43.6	12	...
Sersic 159/03	324.531	A	25.4 × 5.3	-9.2	4.5	...
	1425	B	18.3 × 3.6	-12.8	0.50	...

Table A.2 (continued)

Name	Frequency (MHz)	Array	Resolution (arcsec × arcsec)	PA (degree)	Rms noise (mJy/beam)	References
A2597	4860.1	D	3.5 × 3.5	-45.0	0.025	...
	8460.1	B	3.1 × 0.6	7.9	0.055	...
	328.305	A	7.5 × 5.4	-20.6	1.0	3
	1400	A	1.7 × 1.3	-1.4	0.16	3
A4059	4985.1		0.5 × 0.4	15.8	0.09	3
	8439.9		0.4 × 0.2	-34.2	0.045	19
	328.5	AB	15.7 × 6.2	18.0	4.1	...
	1440.5	A	3.2 × 1.1	0.19	0.070	...
A4059	4860.1	AB	1.4 × 0.9	43.3	0.067	...
	7989.9	A/AB	0.71 × 0.71	-45.0	0.022	23

<sup>a</sup>The radio map is from Lane et al. (2004).

<sup>b</sup>The radio map is from Clarke et al. (2005).

References. — (1) Burns (1990); (2) Carilli et al. (1991); (3) Clarke et al. (2005); (4) Cohen et al. (2005); (5) Dreher et al. (1987); (6) Fabian et al. (2002); (7) Ge & Owen (1993); (8) Ge & Owen (1994); (9) Giovannini et al. (1998); (10) Gitti et al. (2006); (11) Hines et al. (1989); (12) Laing & Bridle (1987); (13) Lane et al. (2004); (14) Reiprich et al. (2003); (15) McNamara et al. (2005); (16) Owen et al. (2000); (17) Parma et al. (1986); (18) Pedlar et al. (1990); (19) Sarazin et al. (1995b); (20) Sarazin et al. (1995a); (21) Sree et al. (2001); (22) Sun et al. (2003); (23) Taylor et al. (1990); (24) Taylor et al. (1994); (25) Taylor et al. (2002); (26) Taylor et al. (2006); (27) van Breugel et al. (1984); (28) Zhao et al. (1993); (29) Young (2004).

## APPENDIX B

### Radio Images

Figures B.1–B.16 present the radio contours for each image listed in Table A.2. The system’s name and frequency are given at the top left of each plot, with the contour level given below. The beam shape and orientation is shown in the superimposed box at the lower left. Figures B.17–B.25 show the resolved radio emission superimposed on the smoothed *Chandra* X-ray images.

Figure B.1: Radio contours

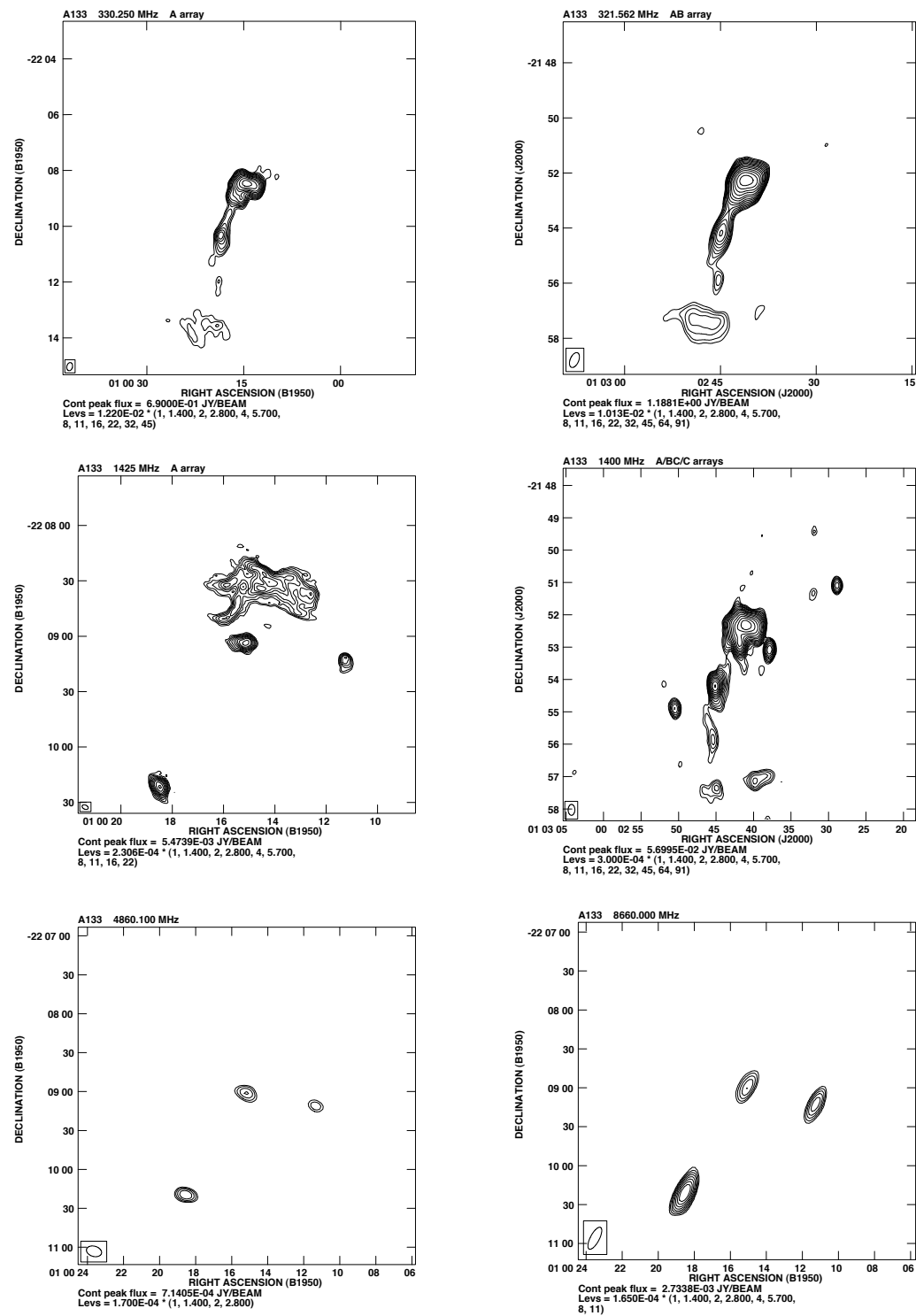


Figure B.2: Radio contours – continued

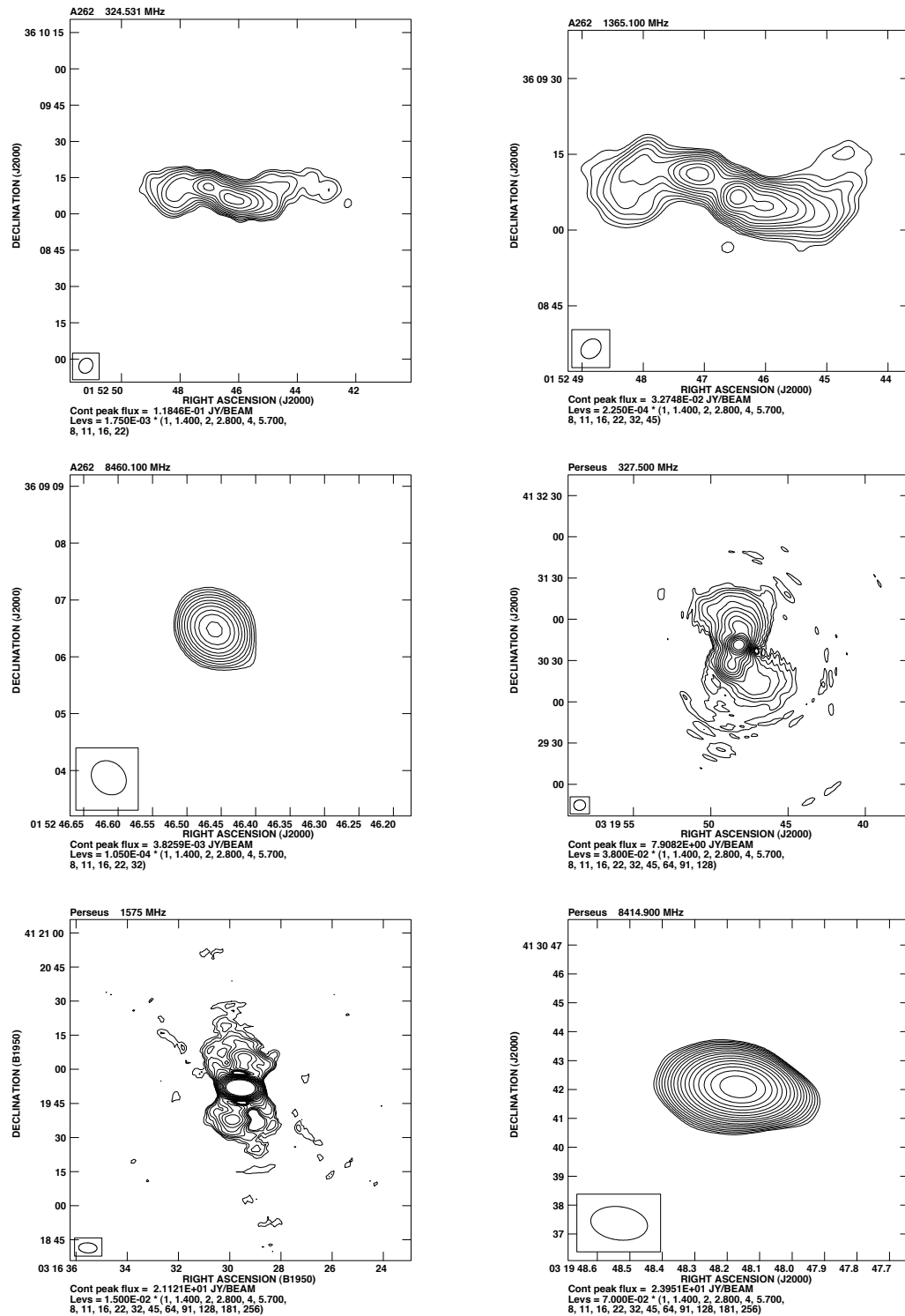


Figure B.3: Radio contours – continued

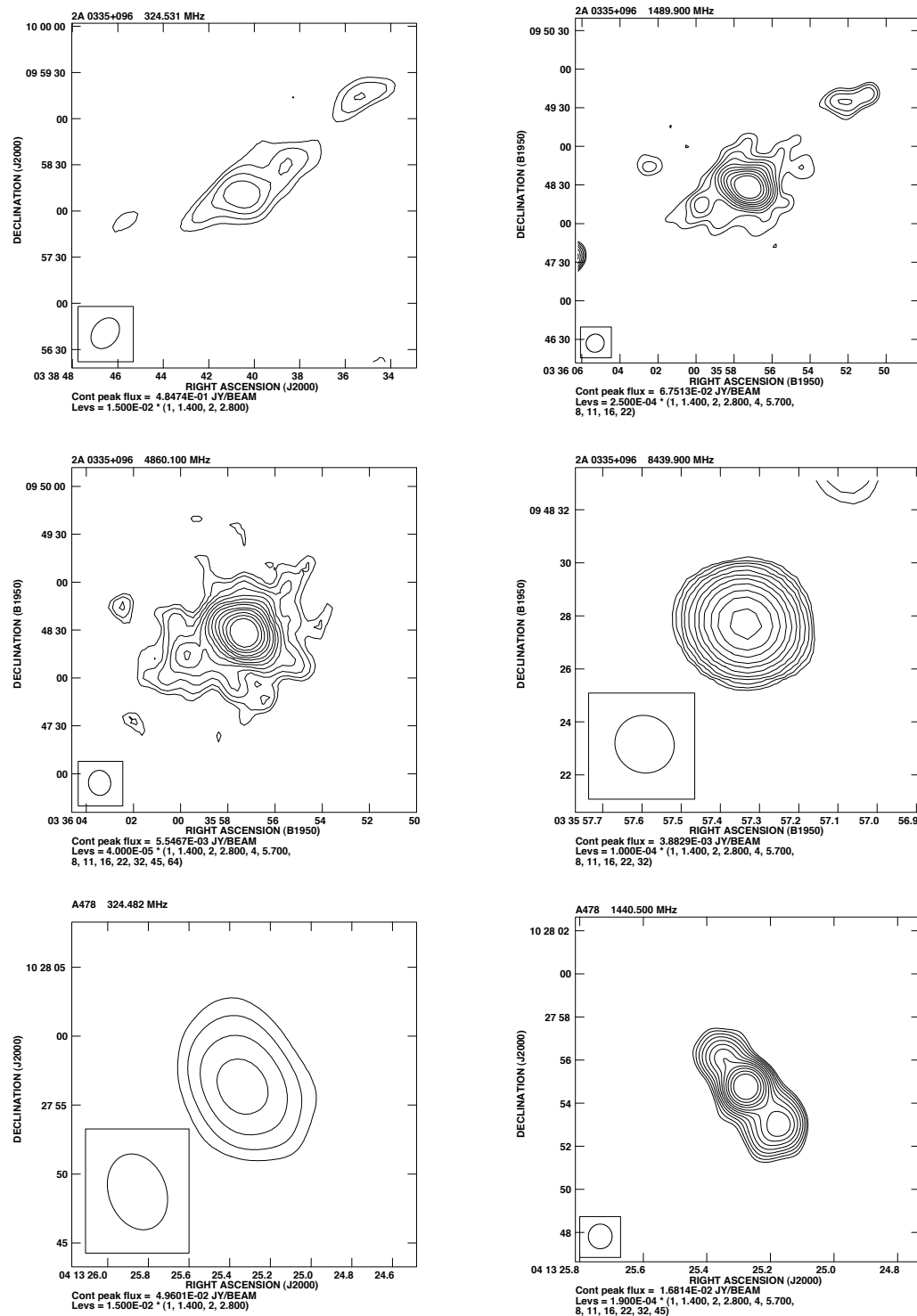


Figure B.4: Radio contours – continued

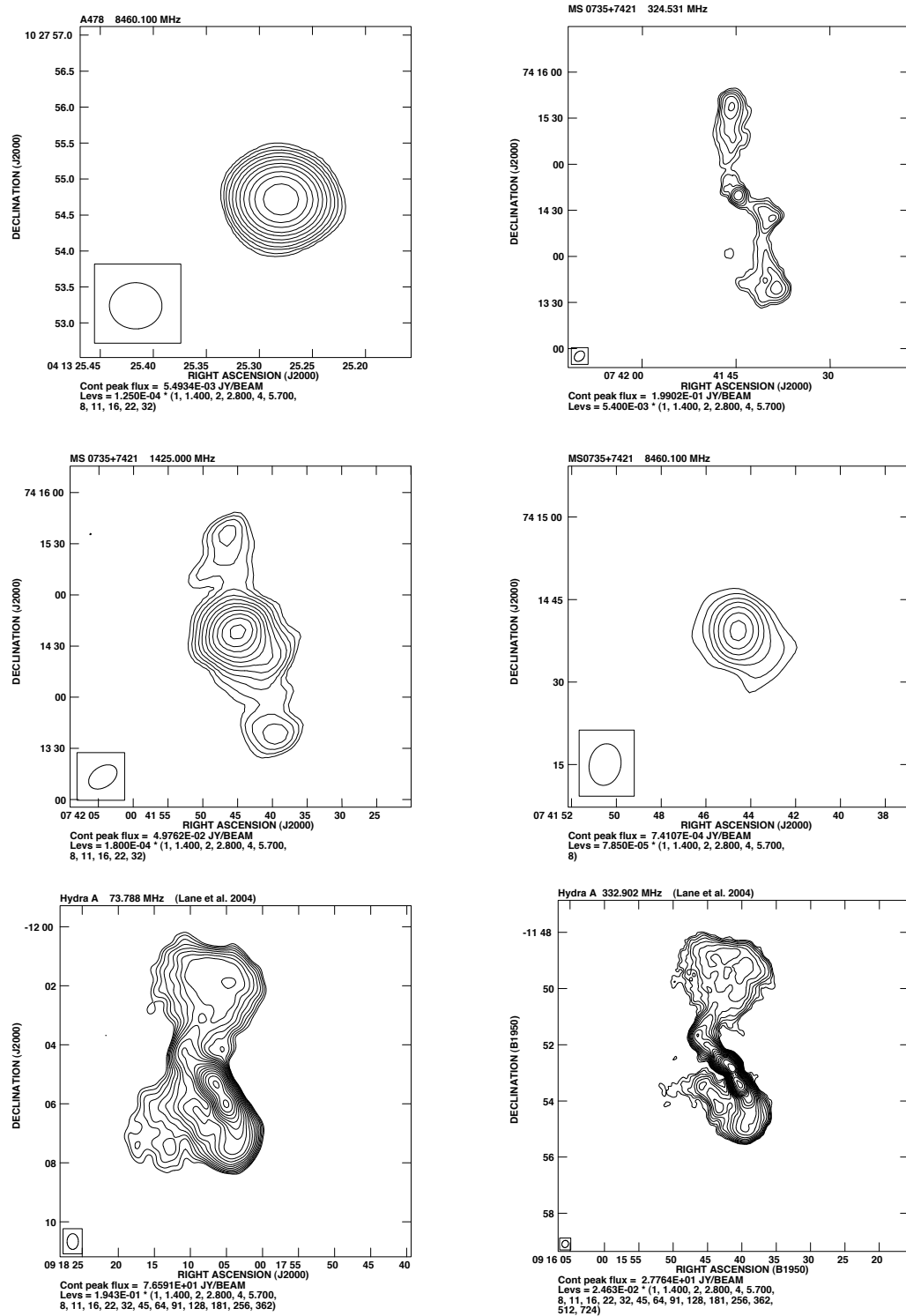


Figure B.5: Radio contours – continued

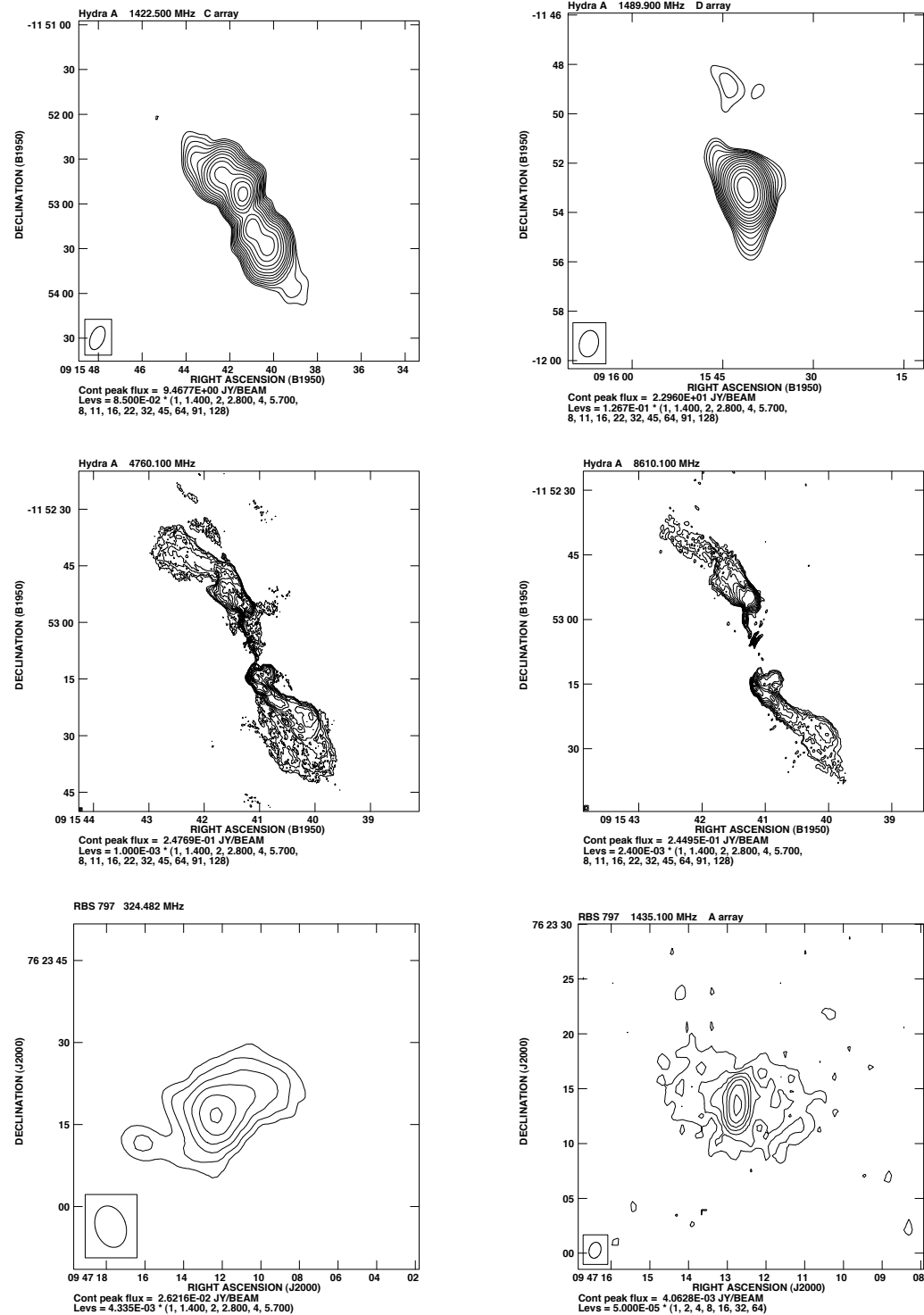


Figure B.6: Radio contours – continued

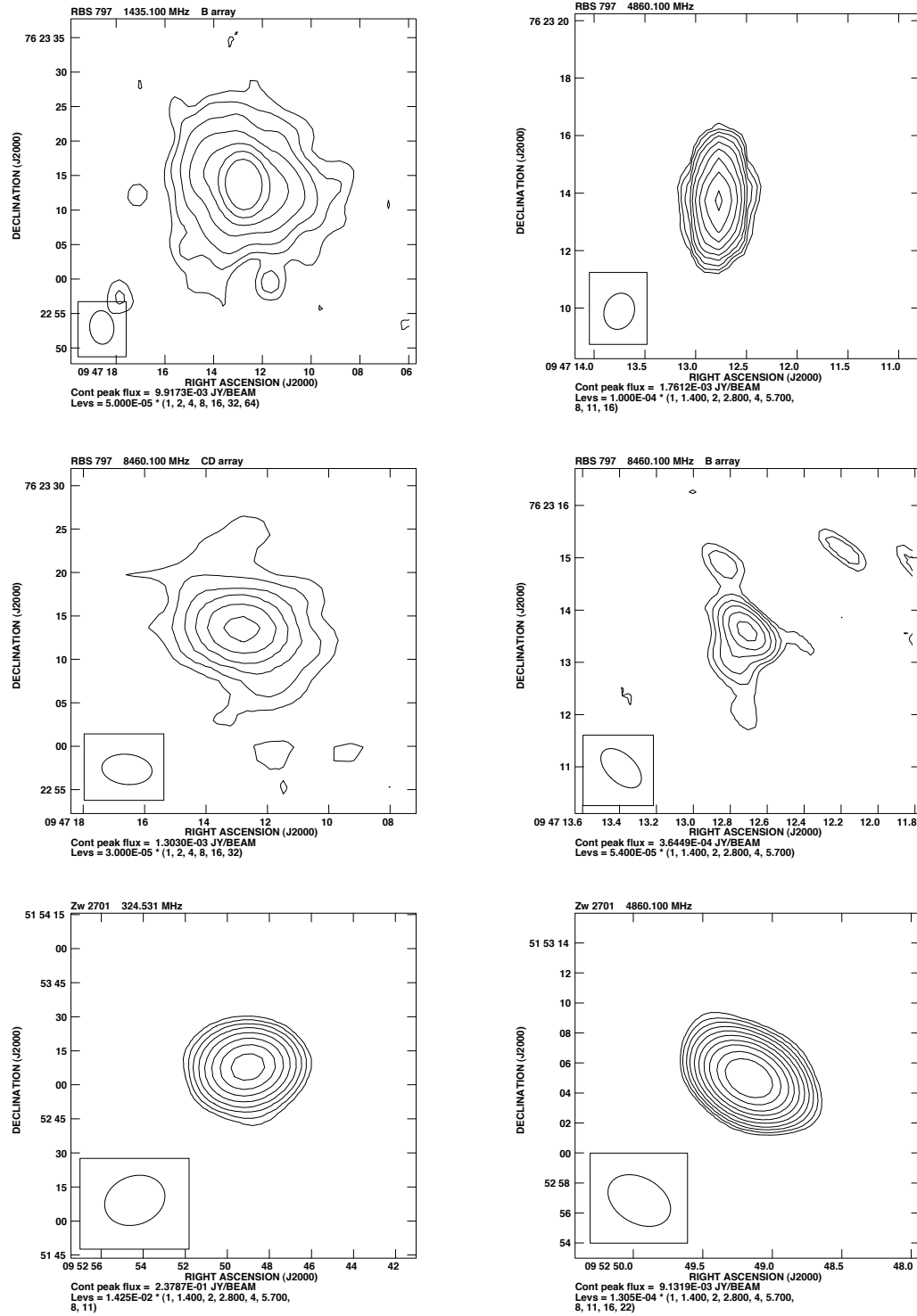


Figure B.7: Radio contours – continued

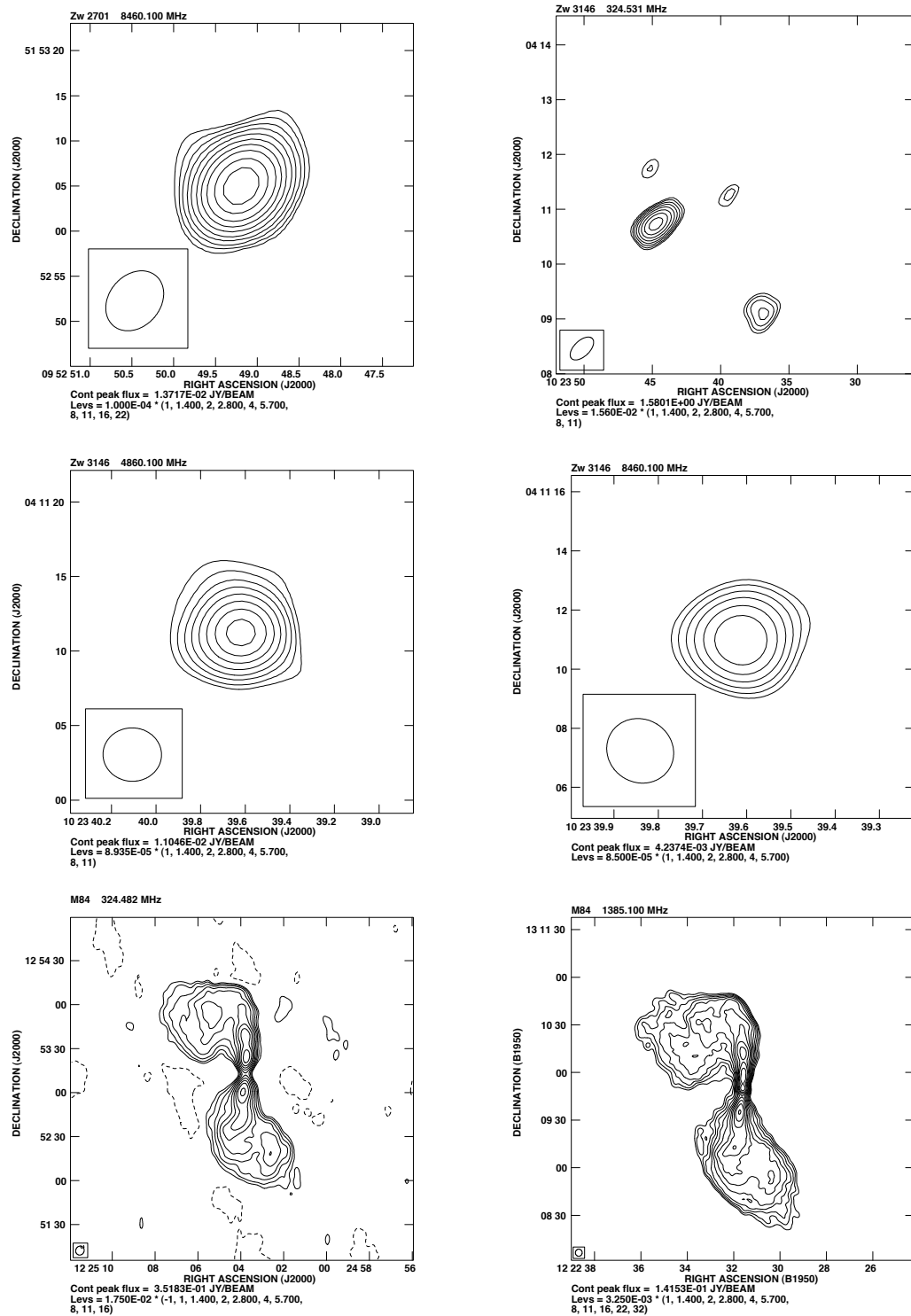


Figure B.8: Radio contours – continued

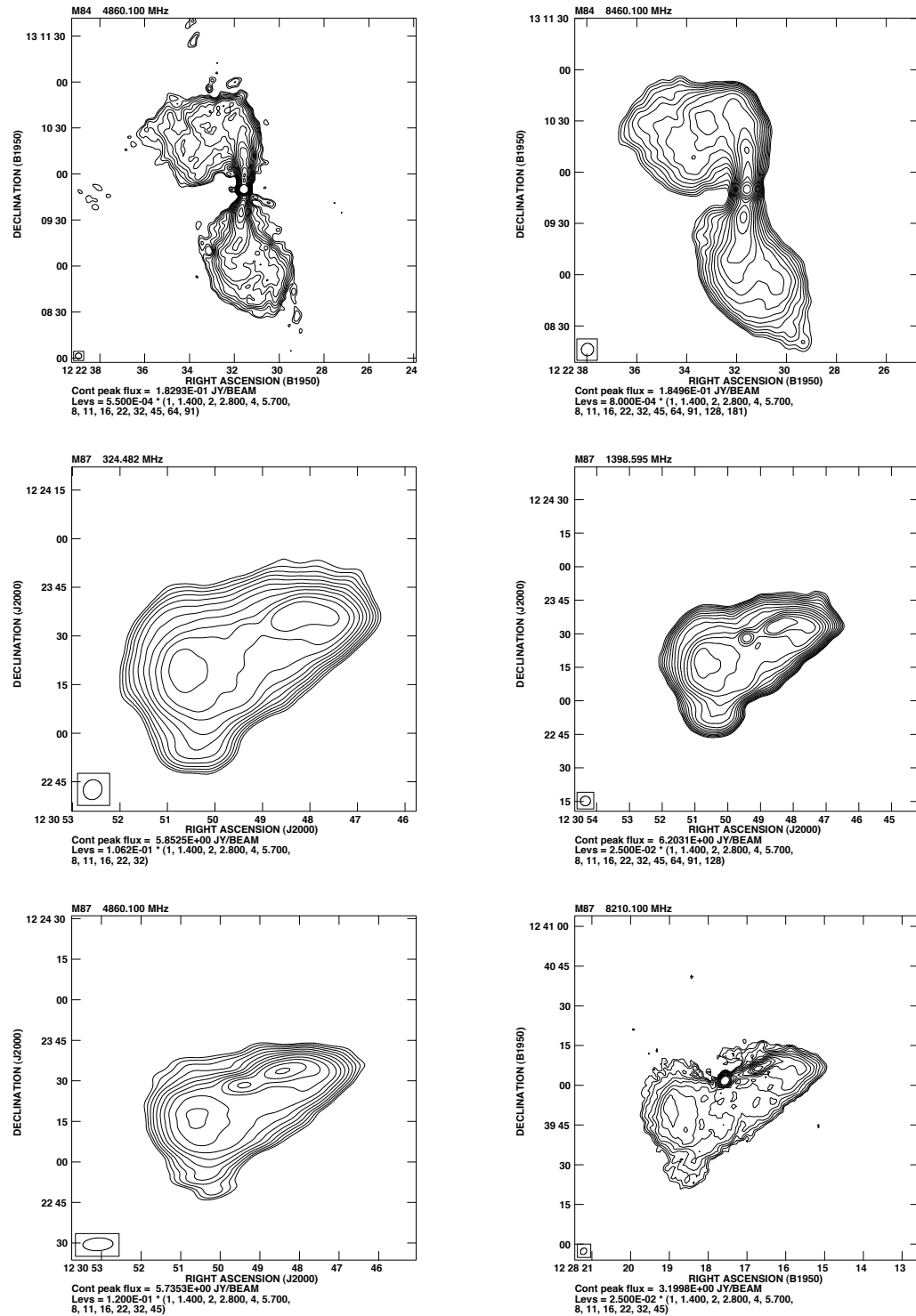


Figure B.9: Radio contours – continued

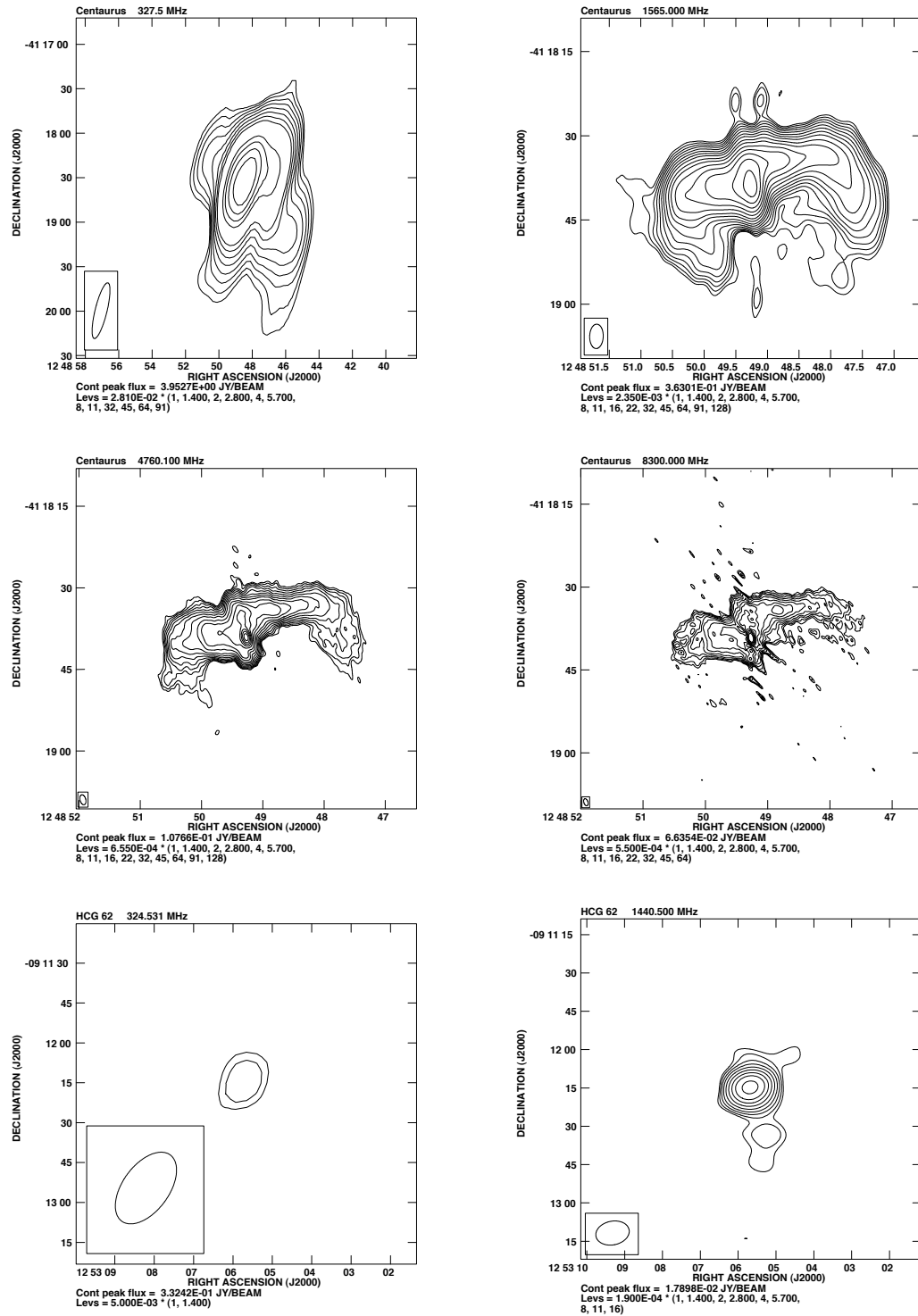


Figure B.10: Radio contours – continued

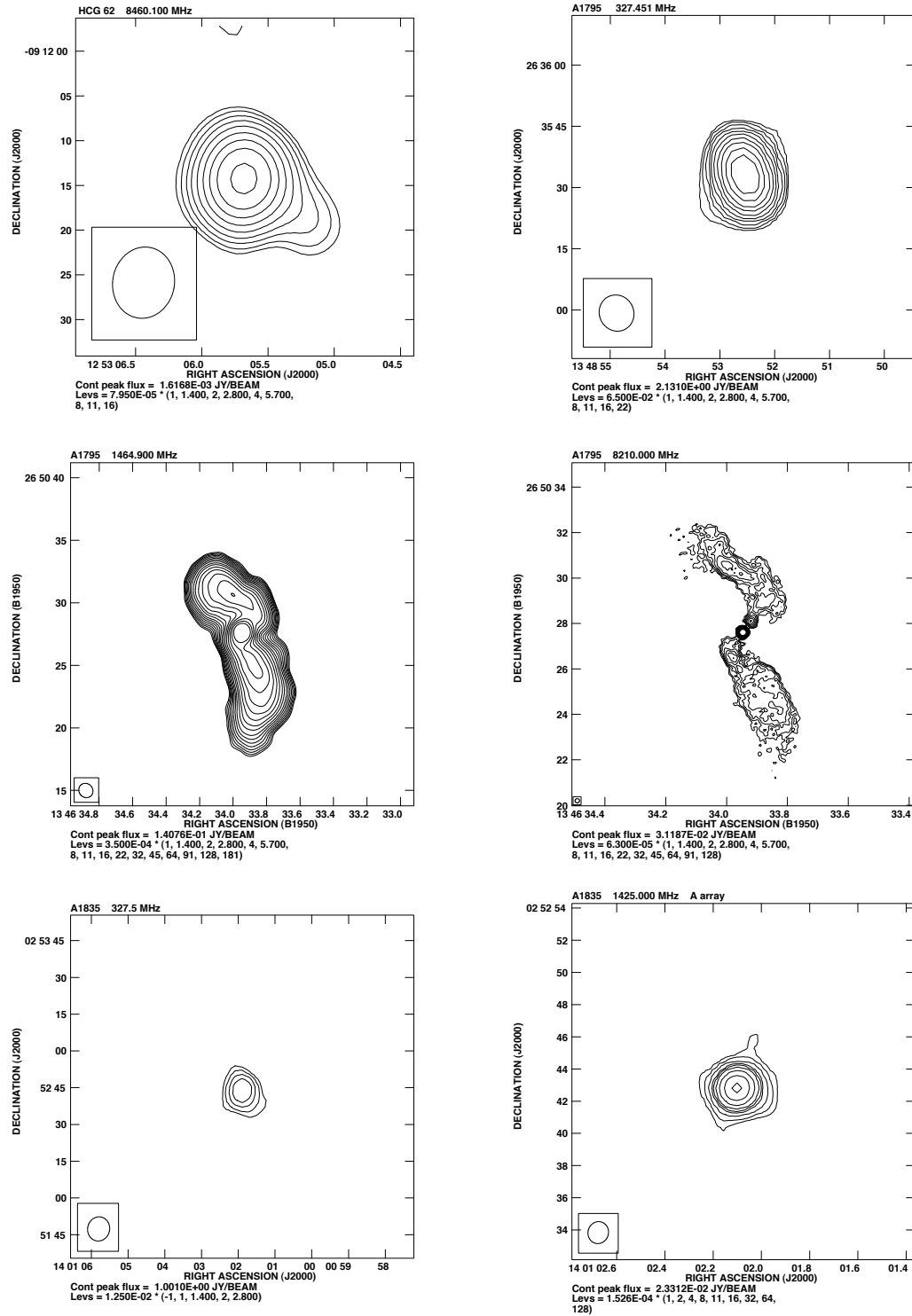


Figure B.11: Radio contours – continued

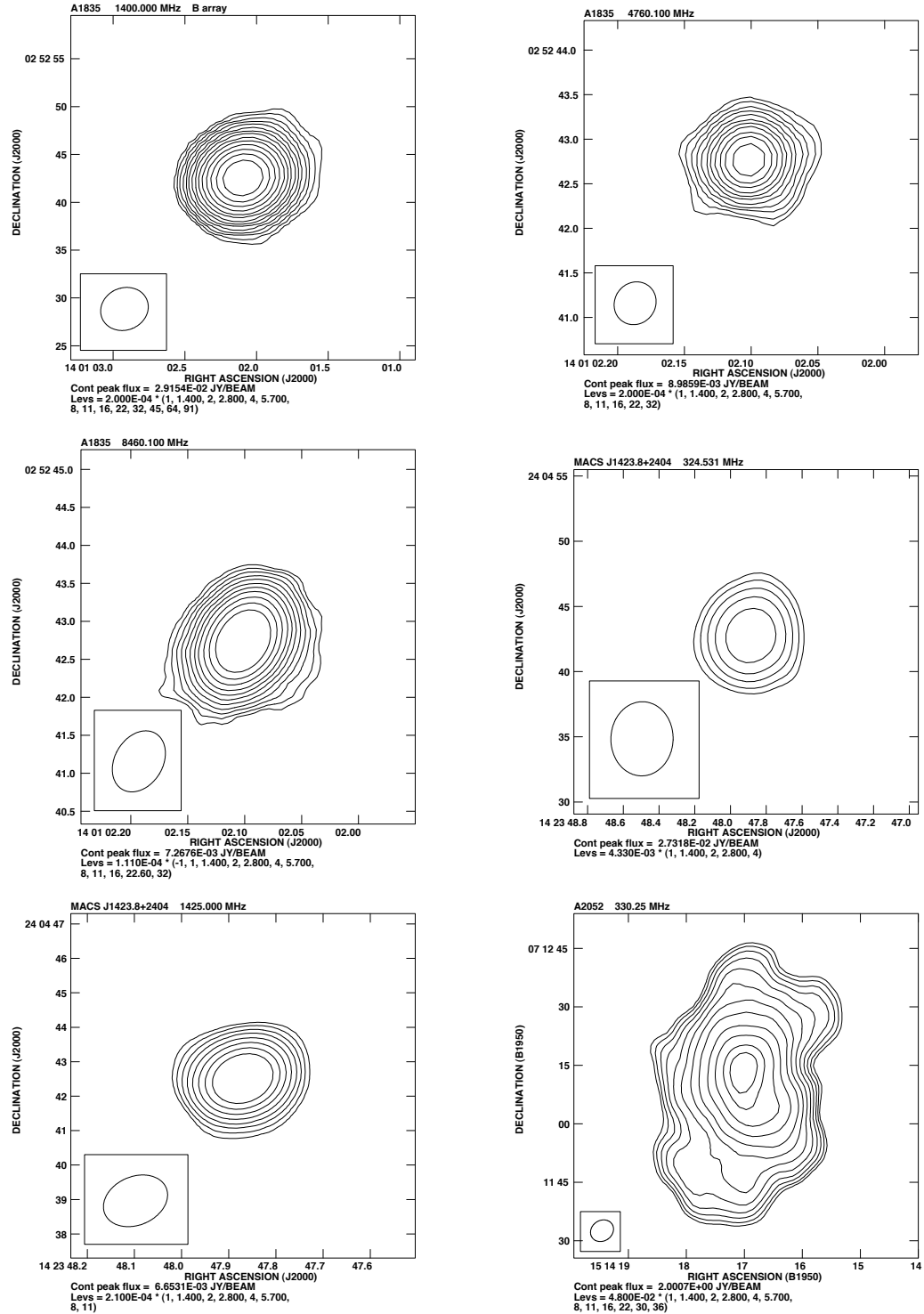


Figure B.12: Radio contours – continued

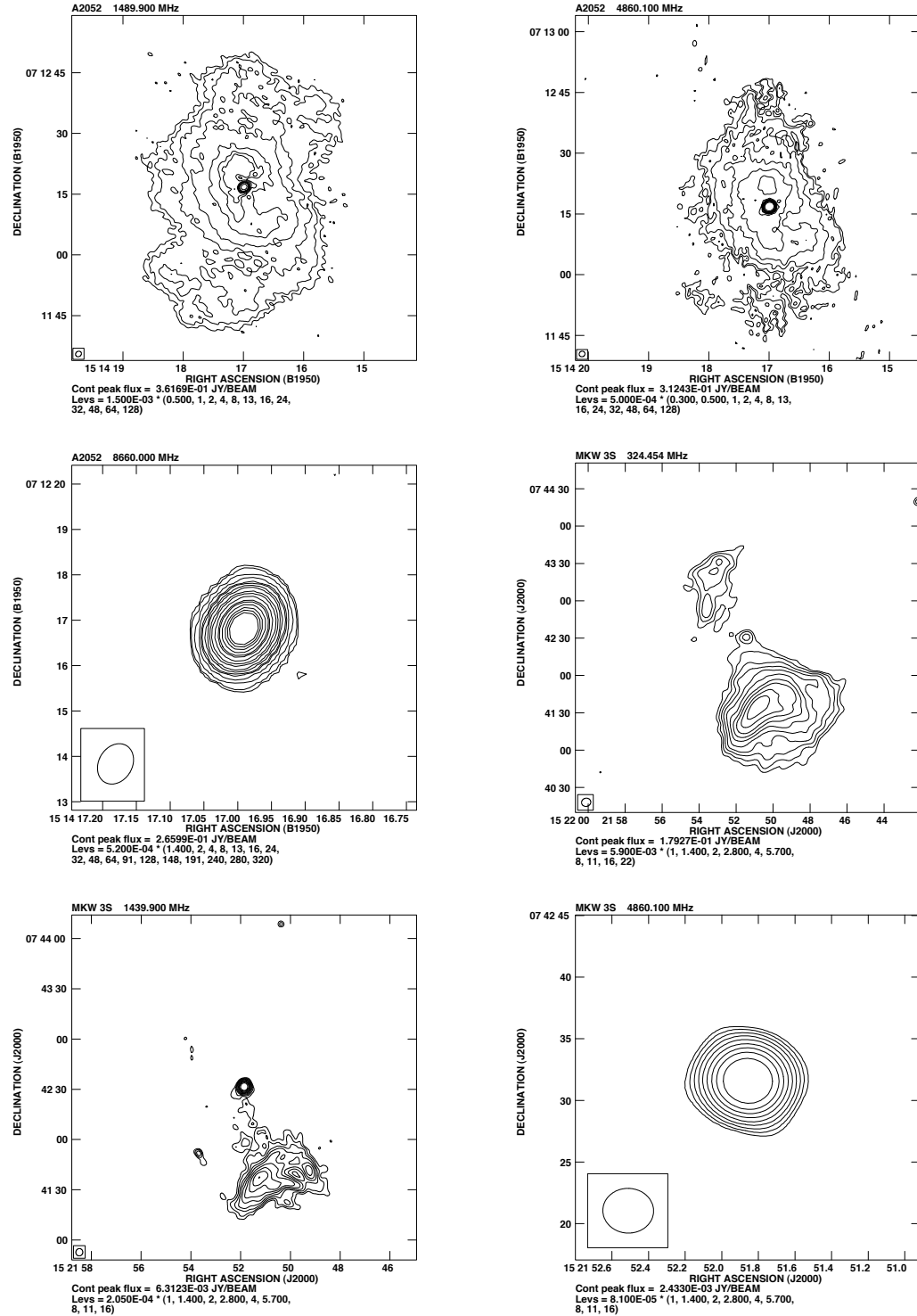


Figure B.13: Radio contours – continued

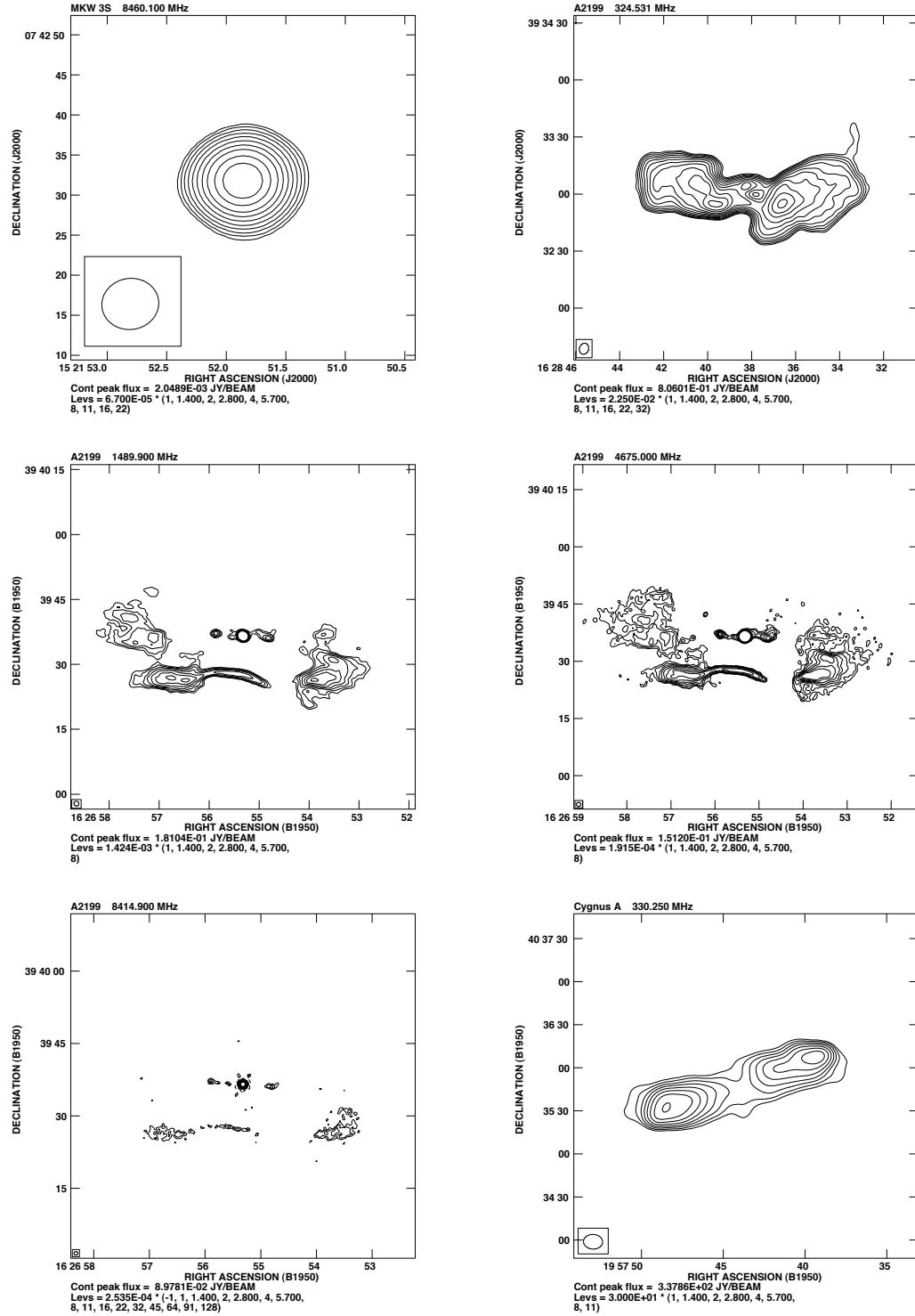


Figure B.14: Radio contours – continued

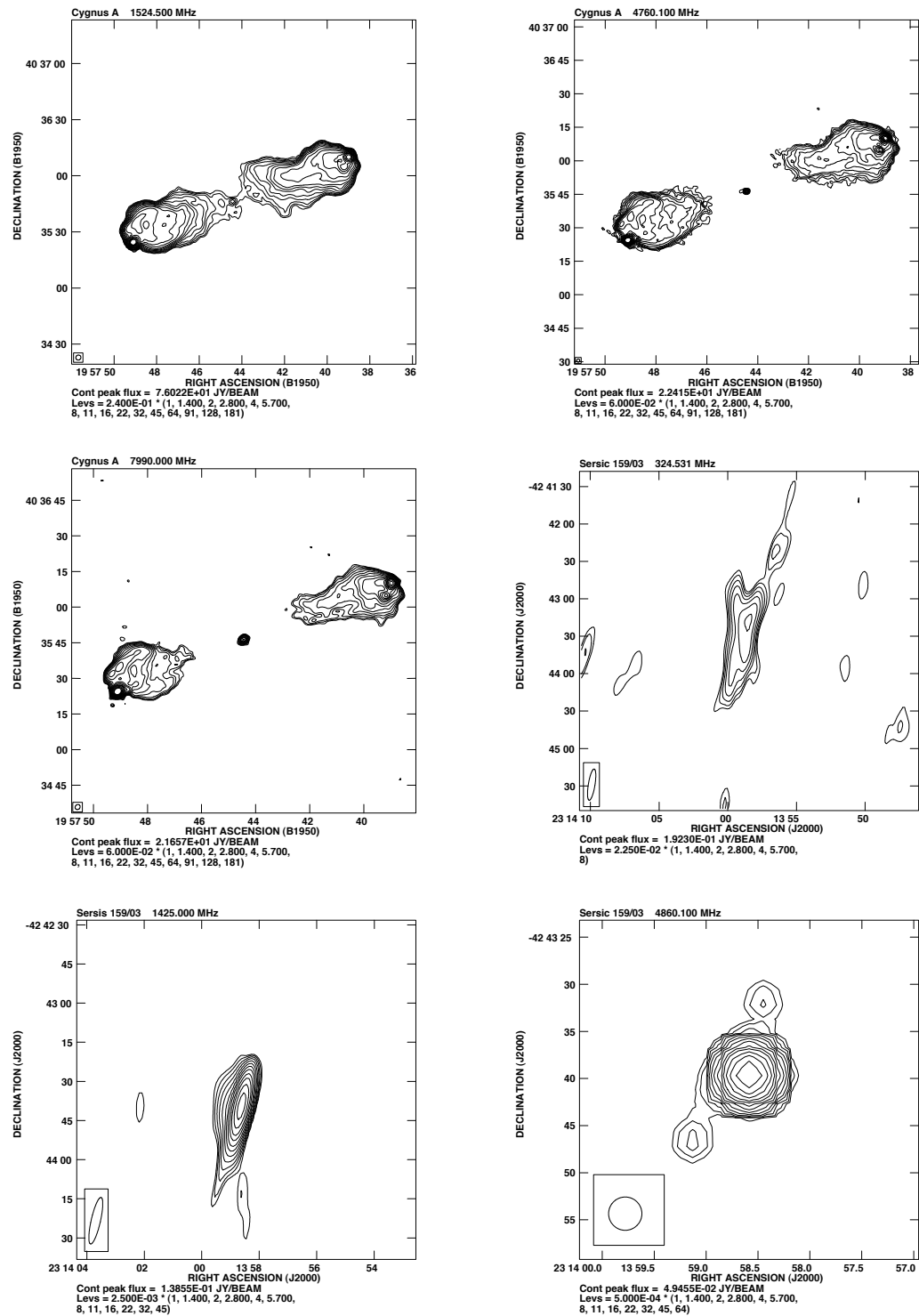


Figure B.15: Radio contours – continued

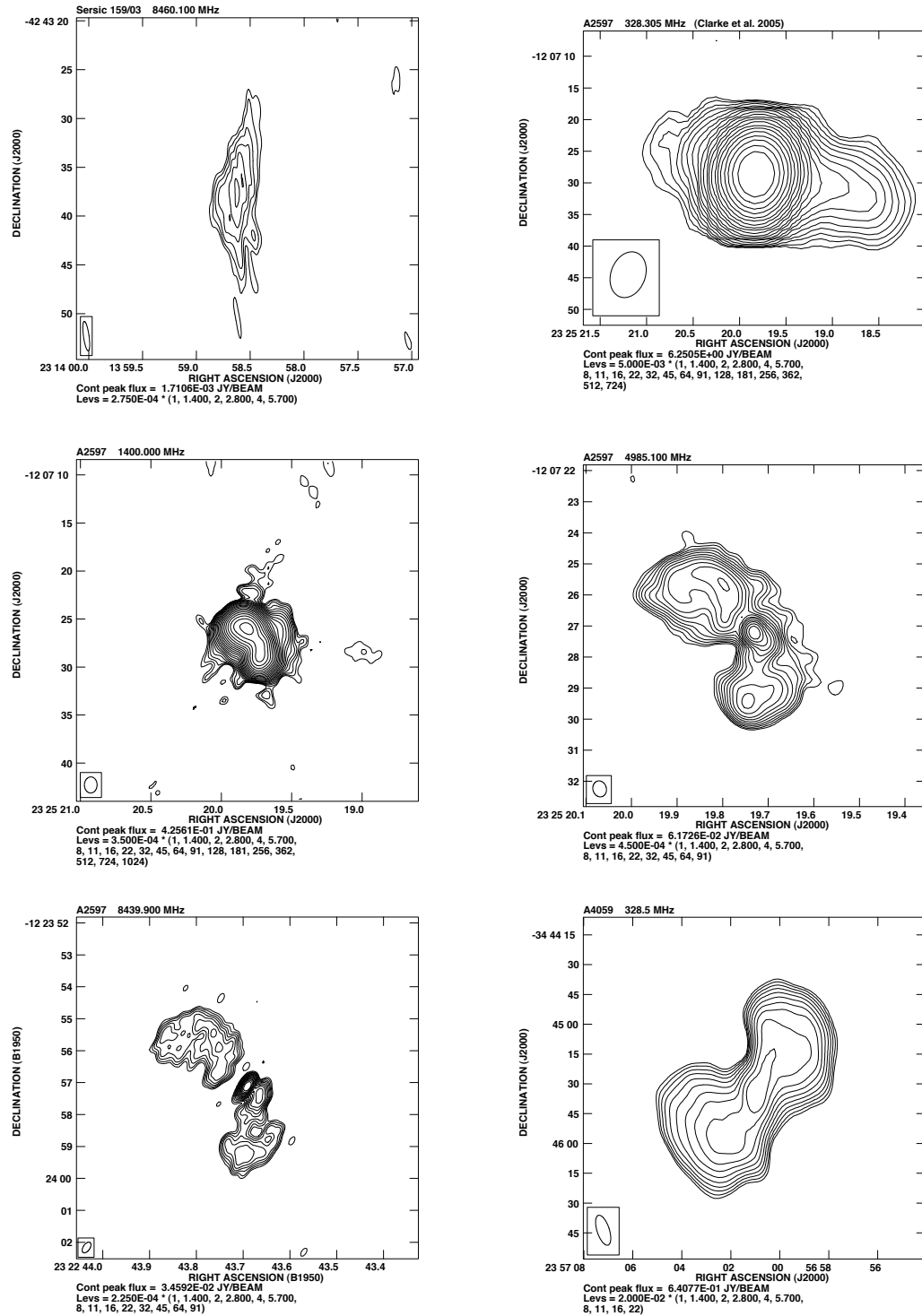


Figure B.16: Radio contours – continued

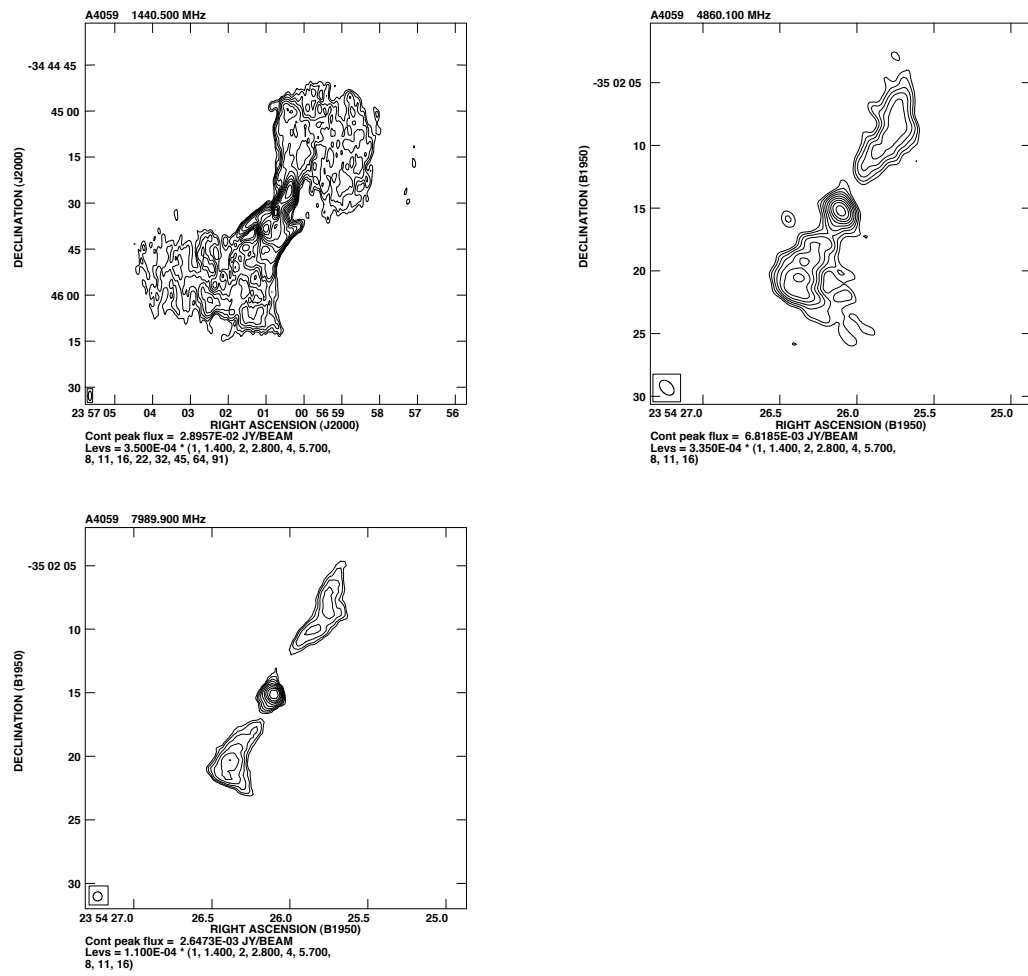


Figure B.17: Radio overlays (green) on the smoothed *Chandra* X-ray images

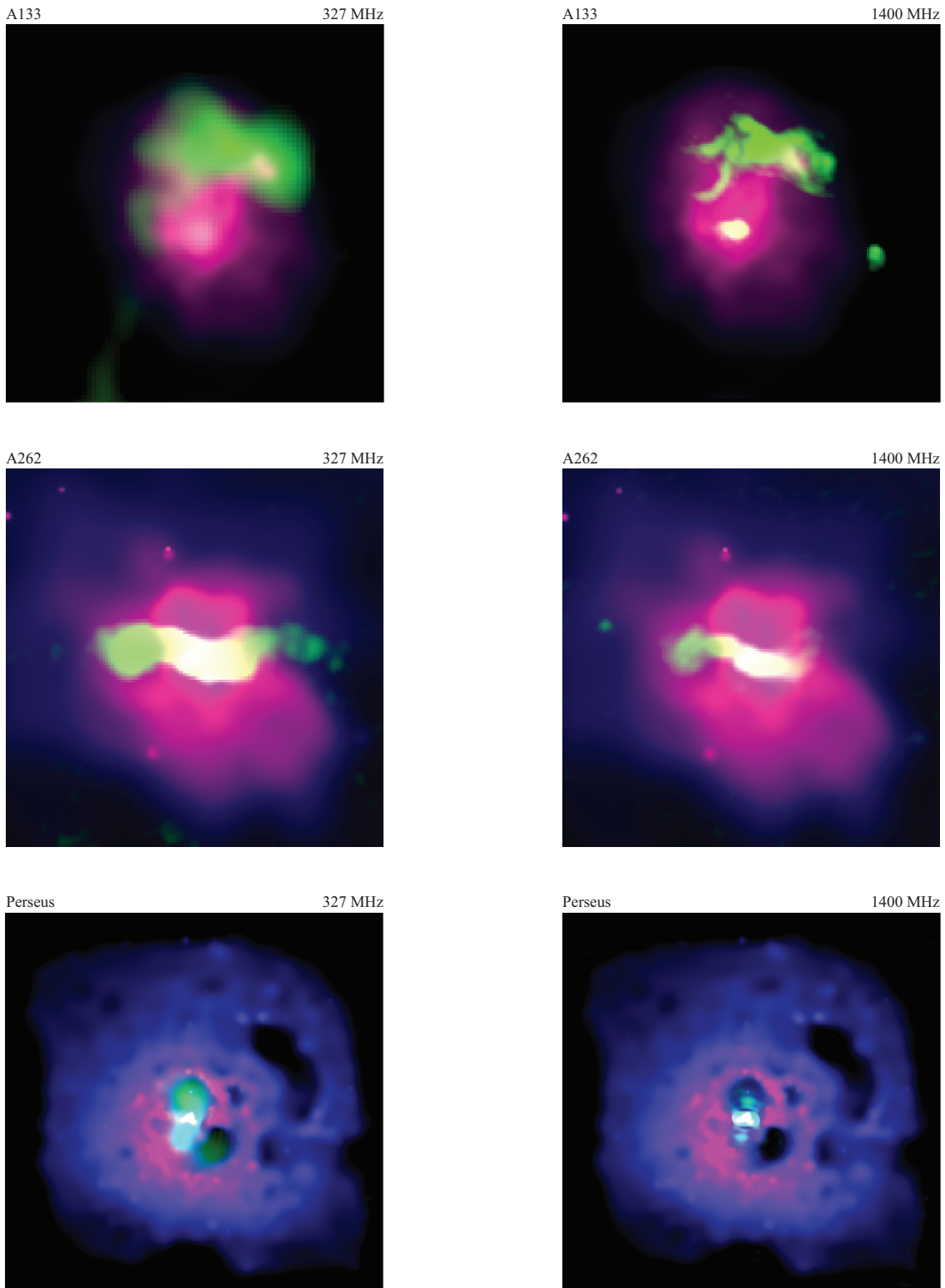


Figure B.18: Radio overlays – continued

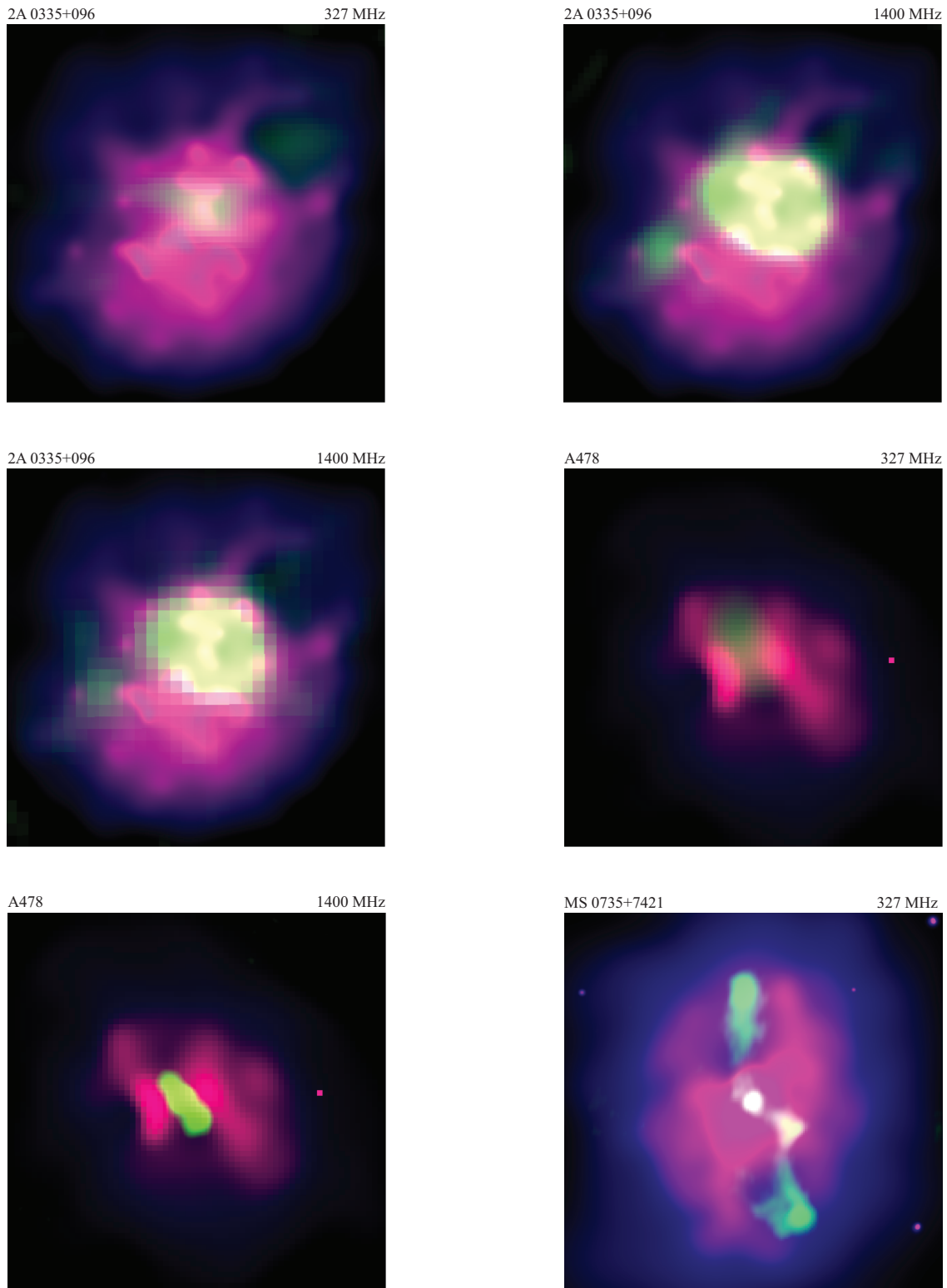


Figure B.19: Radio overlays – continued

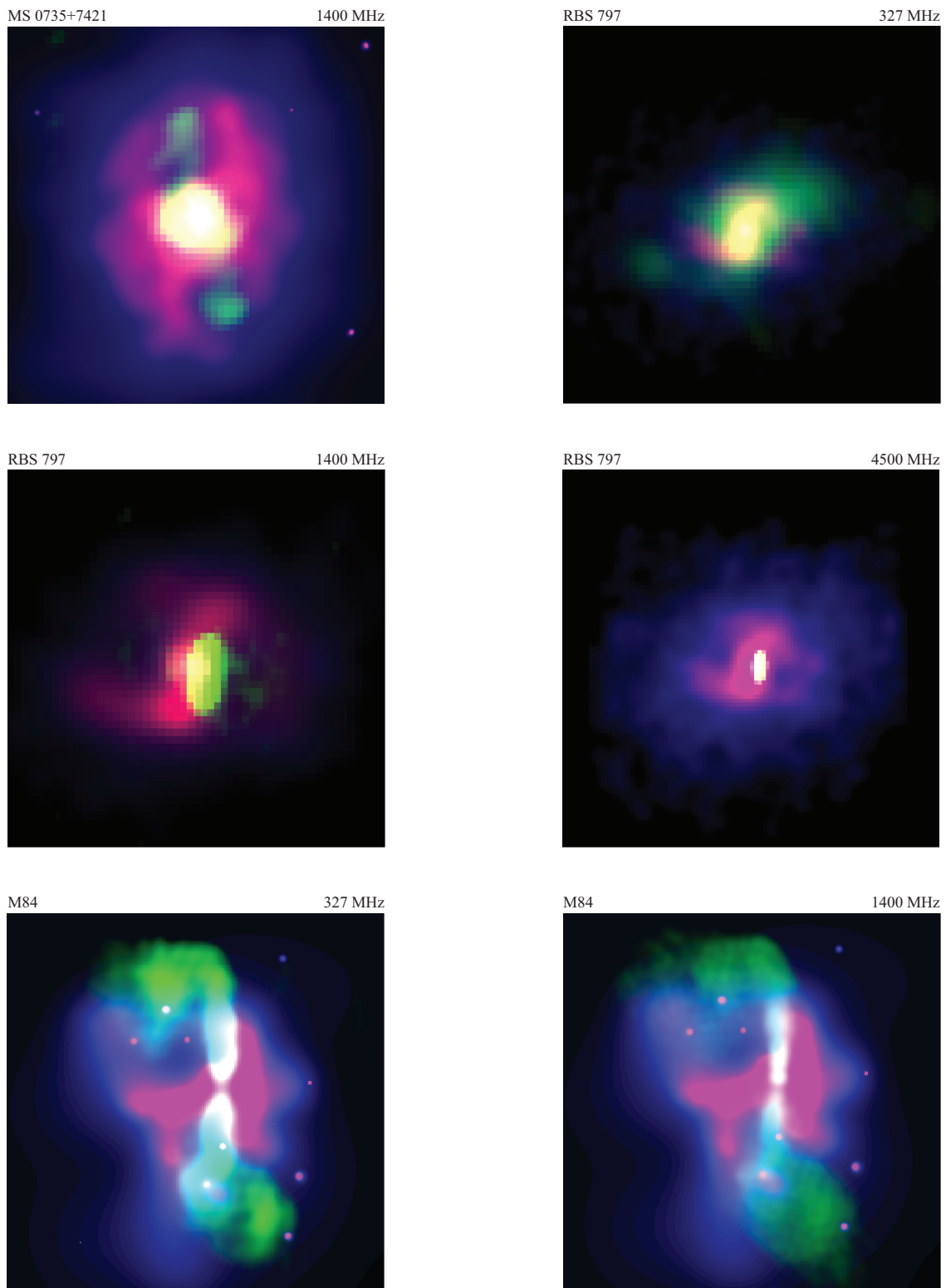


Figure B.20: Radio overlays – continued

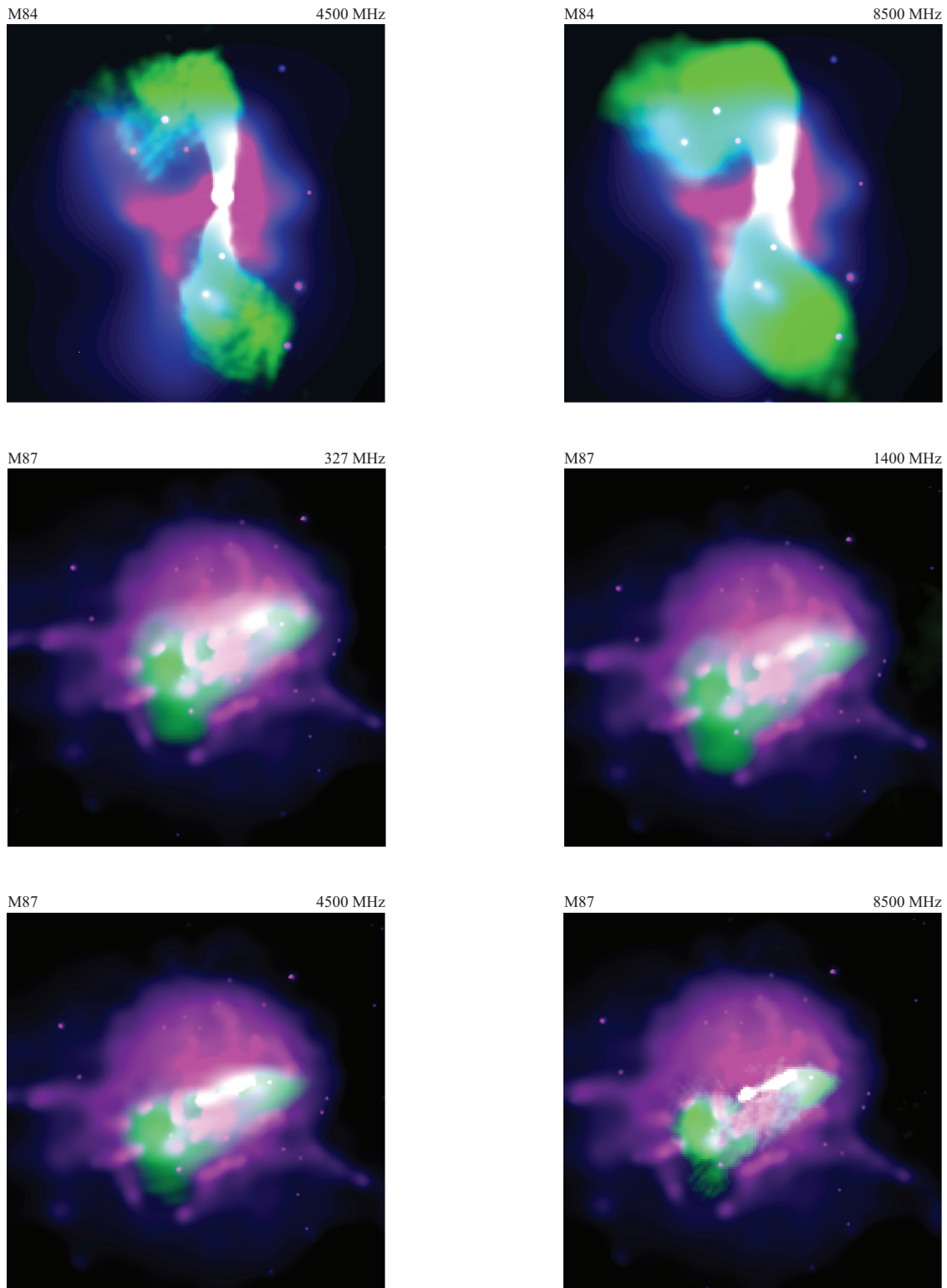


Figure B.21: Radio overlays – continued

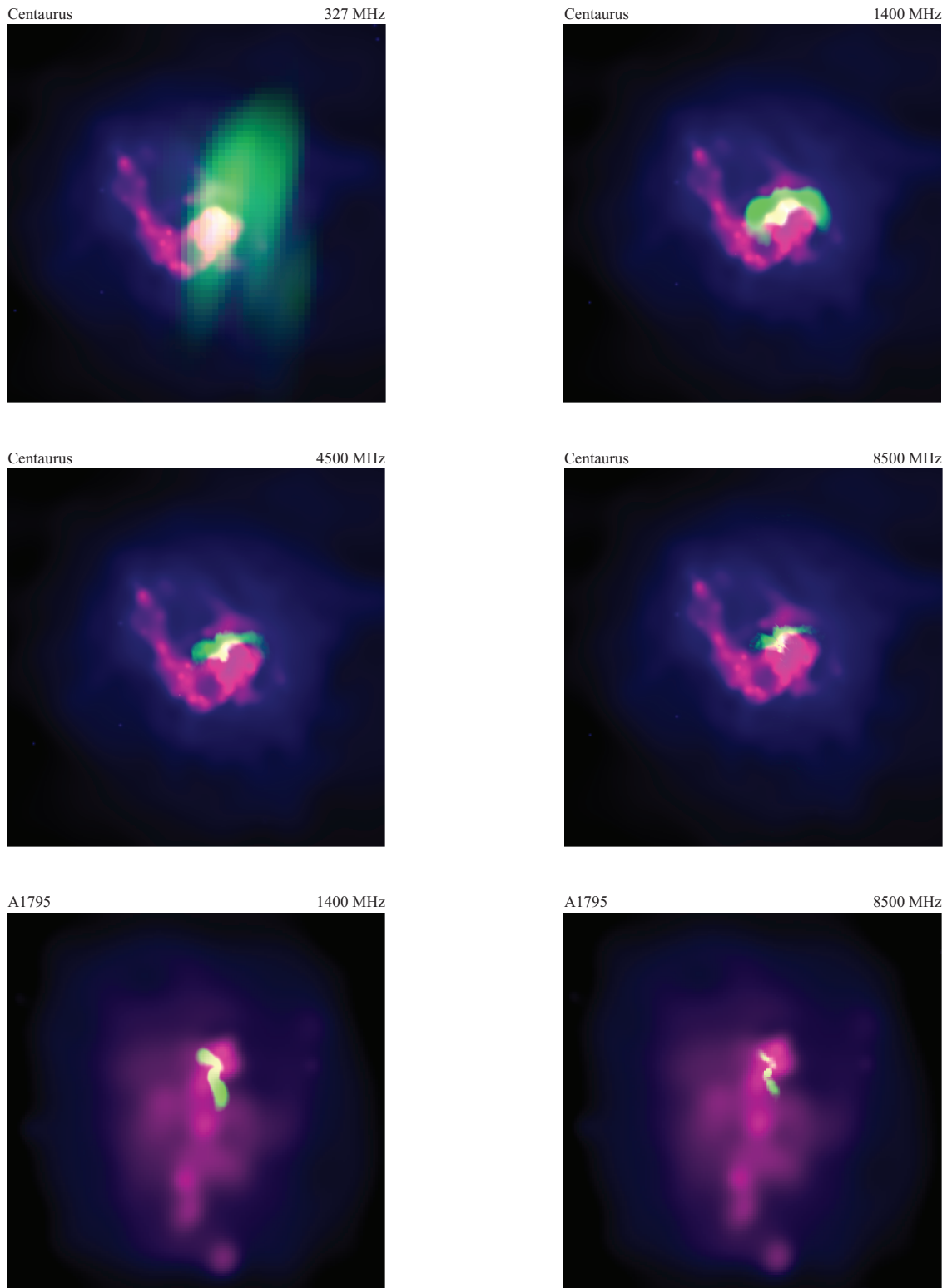


Figure B.22: Radio overlays – continued

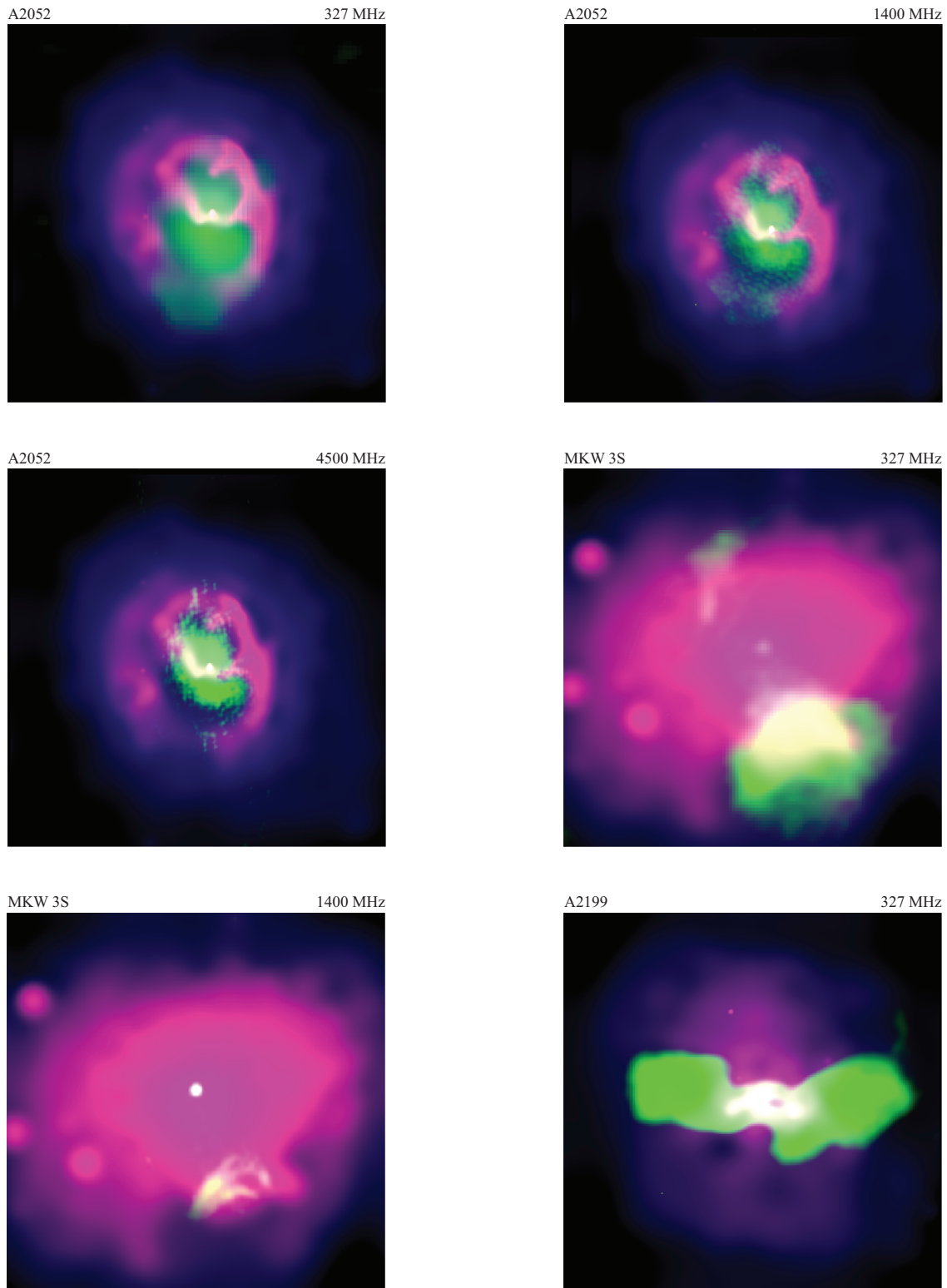


Figure B.23: Radio overlays – continued

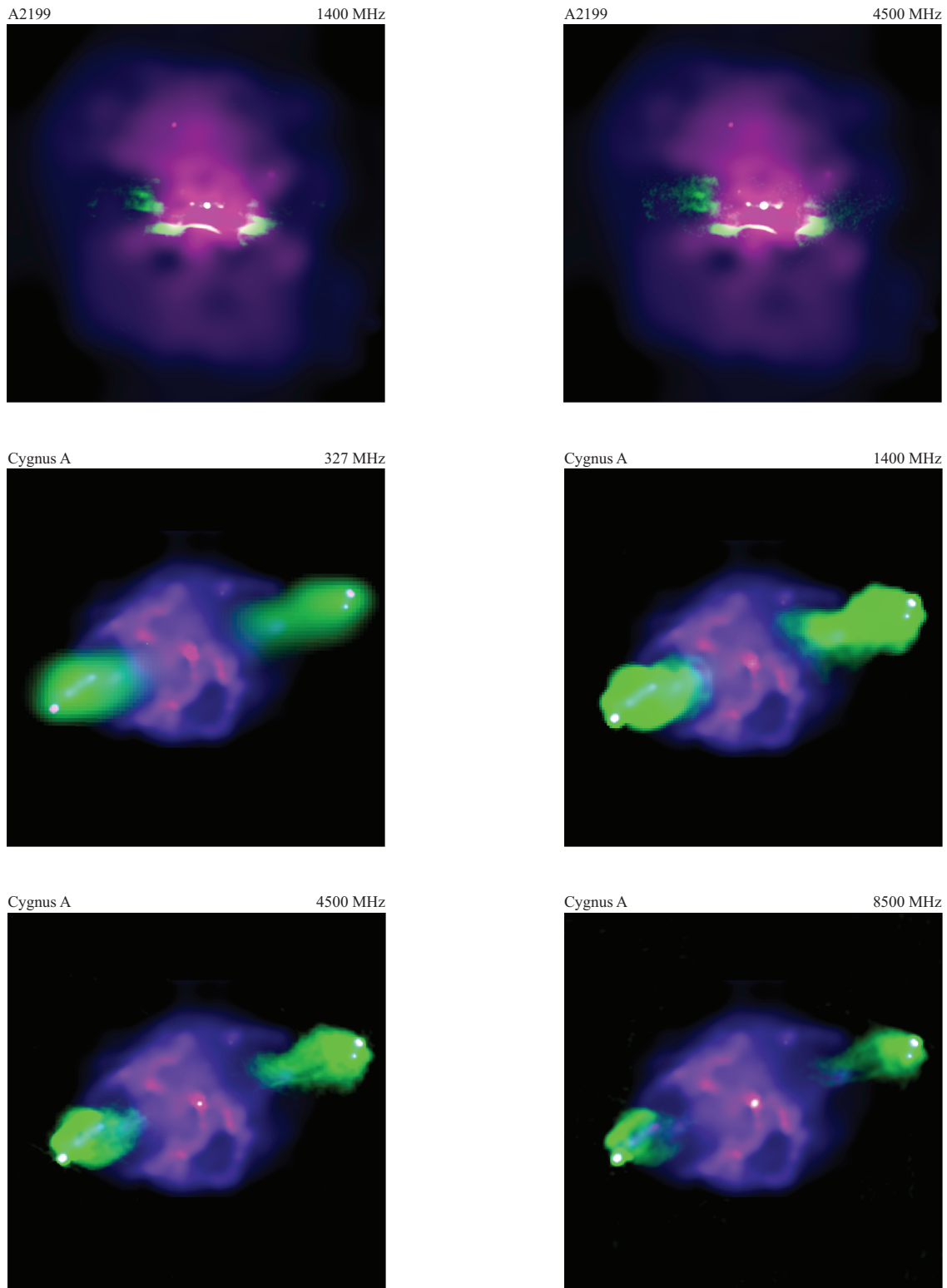


Figure B.24: Radio overlays – continued

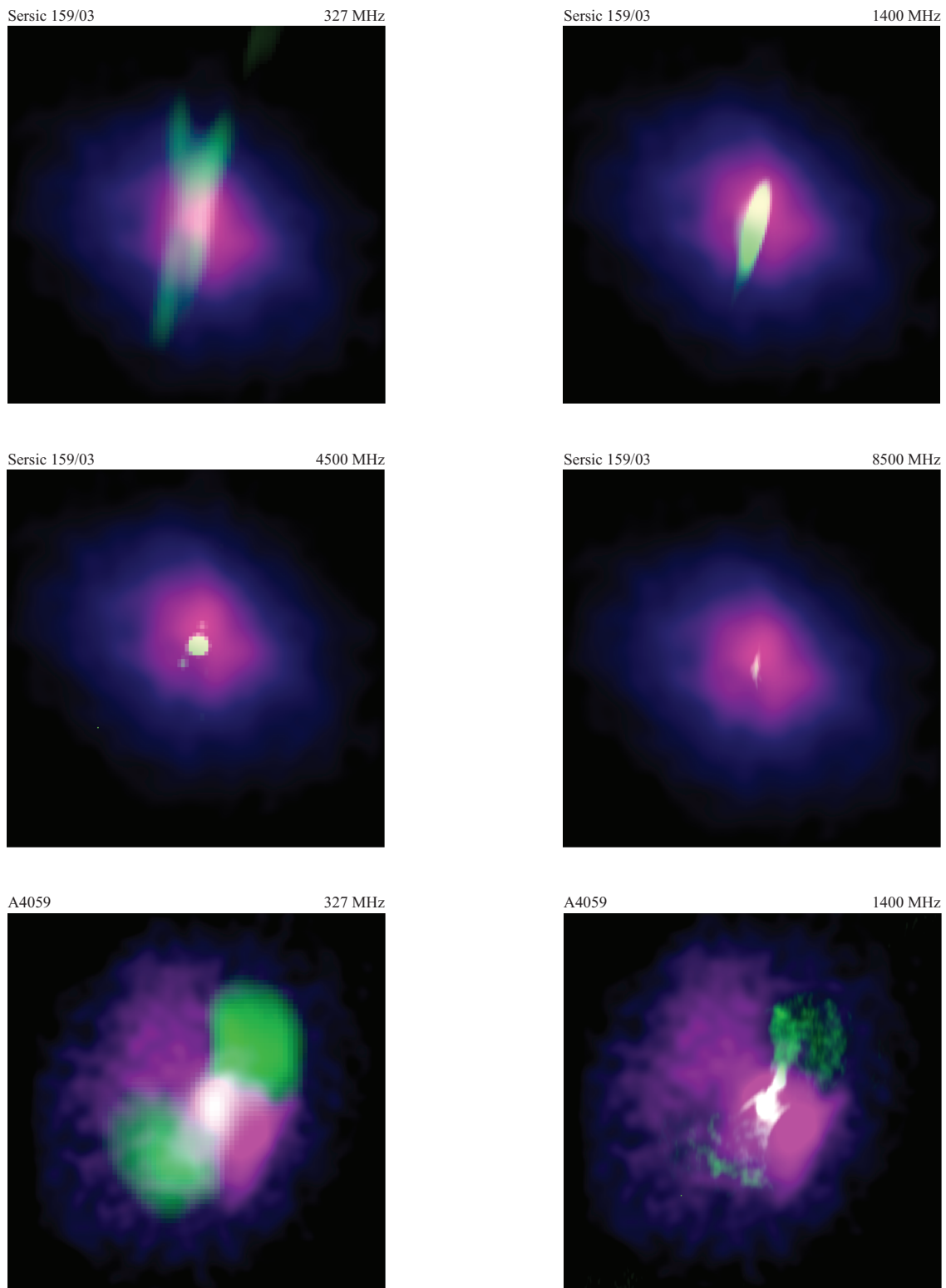
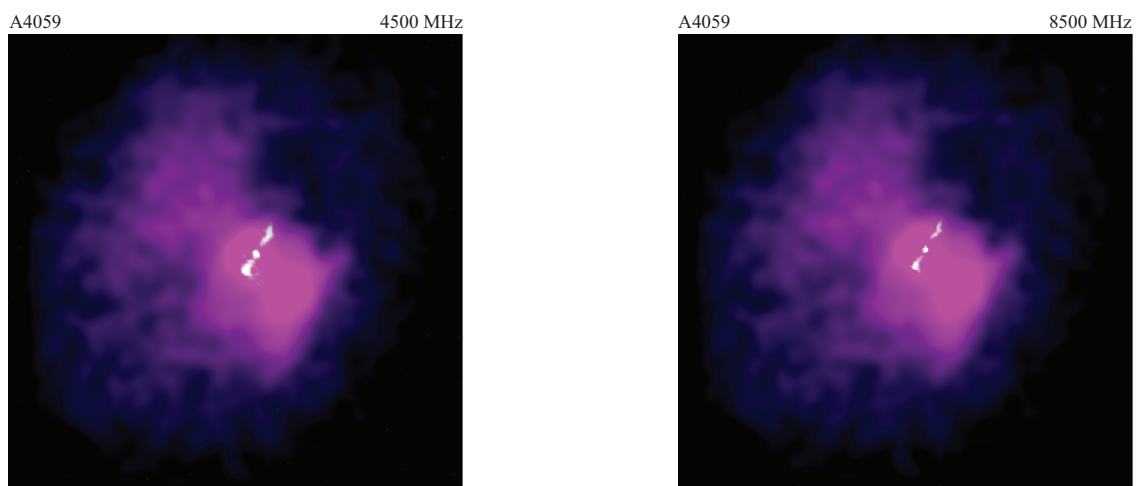


Figure B.25: Radio overlays – continued



## APPENDIX C

### Co-authored Publications

In this chapter are listed the co-authored publications which are not part of this dissertation. Below are my contributions to these articles:

[Nulsen et al. \(2005a\)](#): An initial X-ray analysis of Hercules A.

[McNamara et al. \(2006\)](#): The radio analysis of A1835.